ABSTRACT

Living systems are constrained by the principles of physics. This thesis investigates the physical principles underlying four different problems from living systems, spanning several lengthscales and timescales. I begin by investigating how cell surface filaments influence the virus entry process into a cell. By considering physical parameters such as filament density, stretching, and bending rigidities, the study reveals that these coreceptors can either assist or hinder viral uptake through crumpling or folding around the virus. Next, I explore the underlying mechanism of abnormal nuclear shapes, including bulge and wrinkle formations. These are found to be influenced by chromatin transcriptional activity and inter and intra-chromatin links. Specifically, bulge formations are shown to be driven by chromatin-correlated motion and are dependent on motor and chromatin interconnectedness. Moving outwards, I examine the role of the cell's internal components in confined cell motility and polarity. By focusing on the rigidity of the cytoskeleton and nucleus, I showed the difference in cell speeds and polarity behavior in confinement, as demonstrated in microchannel experiments using vimentin-null and wild-type cells. Finally, I investigated tissue behavior under compression for both solid and fluid-like tissues. By comparing cell shape, I reveal that solid-like tissues exhibit more frustration due to their limited ability to change neighbors, while fluid-like tissues show more dynamic behavior. In all cases, incorporating ideas from physics, such as mechanical forces, activity, and geometry, results in a deeper understanding of living systems' workings. In the process, new physical phenomena are also discovered, contributing to our knowledge of the intricate workings of living systems.

Physical Insights into Biological Processes: From Viral Uptake to Chromatin Organization to Cell Motility to Tissue Rigidity

By

Sarthak Gupta

B.Sc., University of Delhi, 2013

M.S., Indian Institute of Science Education and Research (IISER) Bhopal, 2017

Dissertation

Submitted in Partial Fulfillment of the Requirements

for the degree of

Doctor of Philosophy in Physics

Syracuse University

August 2023

Dedicated to papa, mammi and sakshi...

ACKNOWLEDGEMENTS

My journey as a Ph.D. candidate has been truly fantastic and fulfilling, and I owe this experience to the valuable interactions and support from the people around me. First and foremost, I extend my gratitude to my advisors, Prof. Jennifer Schwarz and Prof. Alison Patteson, for their invaluable guidance, encouragement, and unwavering support throughout my Ph.D. journey. Their mentorship has played a pivotal role in shaping my scientific thinking while nurturing my sense of wonder about the natural world. With their support, I have been able to delve deeply into my scientific interests, all the while keeping sight of the bigger picture. I cherish our free-flowing conversations and eagerly look forward to having many more.

I am also deeply thankful to my thesis committee, Prof. Jennifer Ross, Prof. Christian Santangelo, and Prof. Pranav Soman (the committee chair), for agreeing to conduct my oral exam and examine my thesis work. I am particularly grateful to Prof. Ross and Prof. Santangelo for their mentoring role in this journey. In addition, I express my gratitude to Prof. Moumita Das (Rochester Institute of Technology) for her constant support and guidance during my Ph.D.

I consider myself fortunate to have collaborated with Edward Banigan (MIT), Prof. Andrew Stephens (UMass Amherst), and Prof. Paul Janmey (UPenn), as their contributions have significantly shaped my understanding of the biological world. Moreover, I am grateful to have found mentors and friends in Prof. Tara Finegan (University of Missouri), Dr. Raj Kumar Manna, and Dr. Sadjad Arzash. Our discussions on diverse scientific and non-scientific topics have been immensely enjoyable and enriching.

I want to express my appreciation to the Physics office team, including Yudy, Patti,

Kristine, Cassandra, and Patty, for their invaluable assistance with all the paperwork during these years. Additionally, I thank Larne Pekowsky at SU Research Computing Team for his constant support and prompt email responsiveness on various technical inquiries.

I am also thankful to my master's advisor, Prof. Snigdha Thakur at IISER Bhopal, for introducing me to the field of biophysics and soft matter and motivating me to pursue it as a career. My journey would not have been possible without the constant guidance and support of my bachelor's advisor at the University of Delhi, Prof. Manish Aggarwal. His encouragement and belief in me have been instrumental in my academic pursuits.

During my time in Syracuse, I have had a wonderful experience, thanks to my friends and colleagues around me. Chaitanya, Merrill, and Nick have been close friends and partners in crime through numerous adventures. I treasure memories from the awesome group hangouts with Preeti, Deepa, Mahesh, Sumon, Asad, Anand, and Raj for many potluck dinners, movie nights, and celebrating festivals that made the journey so delightful. Thank you, Prashali, Sourav, Kevin, and Kamalendu, for so many parties and hangouts in the last few years. Late-night discussions with Manu, Varun, Kesavan, and Chaitanya have been intellectually stimulating and have exposed me to many fascinating topics.

Lastly, but most importantly, I want to express my deepest gratitude to my family. My dad, who sadly passed away during my Ph.D., continues to be a guiding light in my life. My mom and my sister have been unwavering in their belief in me and their support. Thank you for being patient, especially for the last three and half years with me, for being unable to visit home during and after the pandemic, and for bearing through all this time on video calls. And to Anshu, the most important person during this journey, thank you for your patience, love, and unwavering support. You have been my rock throughout these years, and I am grateful beyond words.

Contents

List of Tables

List of Figures

Chapter 1

Introduction

Biology is physics. Just as the atoms making up your computer keyboard are subject to the laws of physics, so are the atoms that comprise you, the reader of this thesis. Your atoms, in part, are grouped into amino acids, which, in turn, are grouped into proteins that are grouped into cells to form a multiscale system. Each change in scale requires a leap in understanding of living matter. Given the recent proliferation of experimental techniques quantifying living matter, such as yourself, the physics of living matter, or biophysics, is a rapidly growing subfield in physics. Biophysics is a subfield in which physical principles underlying various biological processes are uncovered. Understanding these principles will lead us to better understand life itself. To achieve this aim, we develop and study computational models to interpret the results of these proliferating biophysical experiments. Such collaboration ultimately leads to predictions from the modeling that can then be tested in the lab.

The application of physical principles to understand biological processes is not a new endeavor by any means. For example, in the seventeenth century, Robert Hooke's observations using a magnifying glass led to the discovery of the microbial world [1], which eventually led to the establishment of the germ theory of disease [2]. Another example could be the works of Julius Robert von Mayer, a German physician, chemist, and physicist, who first formulated the first law of thermodynamics in 1841 [3, 4] and then went on in 1842 to posit that oxidation, as it is now known, is the primary source of energy for any living creature [5, 6]. As the field of biophysics grew, in 1944, the book "What is Life?" by physicist Erwin Schrödinger inspired a generation of biophysicists in subsequent years [7]. One of the landmark achievements of the field is the discovery of the DNA's double helix structure by applying techniques from physics by Franklin, Watson, and Crick [8].

In the last few decades also, physics has significantly contributed to our understanding of living systems, be it in a healthy state or a diseased state. For instance, researchers have very recently found that quantification of both cell shape and cell nuclear shape in breast cancer tumors are predictors of a physical process known as unjamming that can lead to the breast cancer cells leaving the tumor and spreading cancer [9]. From a

practical standpoint, including the physics of unjamming enhances the prognosis accuracy of patients [9]. As for another example, active matter models based on physics principles have enhanced our understanding of bacterial fruiting body formation behavior in starving bacteria cells [10]. These are just a few examples of how physics plays a vital role in studying living systems. Overall, the physics of living systems holds great promise for unraveling the mysteries of life.

Studying living systems has not only provided insights into biology but has also led to the development of new physics. For instance, understanding how collective motion arises from self-propelling cells [11, 12] has revealed unique physics distinct from other complex materials like sand [13, 14]. Additionally, the study of biopolymer networks has led to the discovery of new physics related to rigidity transitions [15, 16]. Furthermore, with its internal energy injection, active matter [17, 18, 19] has introduced new physics that differs from traditional soft matter problems where energy is injected only at material boundaries, such as through shear [13]. Instead, in active matter, each constituent particle generates its own internal energy that motivates the self-propelledness of the particles to lead phase separation [20].

In biophysics, given the multi-scale complexity of the situation, collaboration between theorists and experimentalists is essential for scientific progress. This thesis exemplifies the significance of close collaboration with experimentalists in developing physics-based models relevant to biology. Each chapter of this work demonstrates how modeling, in conjunction with experimental evidence, leads to the discovery of new physics across multiple scales of biology, ranging from viruses and chromatin to cell motility and tissue dynamics. *As the models will focus mainly on the role of mechanics, this thesis pertains to the biophysics subfield of mechanobiology.* Please note that the four different topics are motivated by experiments being conducted in the prolific Patteson lab.

In this thesis introduction, we will introduce a set of questions that address the significance of physics in biological processes. In section (1.1), we examine the mechanics involved in viral uptake by the cell surface. Section (1.2) focuses on the role of active chromatin dynamics on the structure of the deformable nuclear shell. Furthermore, in

section (1.3), we explore the role of cytoskeletal physical properties in the dynamics of cell motility in confinement. Finally, in section (1.4), we investigate the behavior of tissue rigidity under uniaxial compression. By studying these biophysical processes, we gain insights into how physics and biology interact, leading to a better understanding of these fundamental life processes.

1.1 Mechanics of viral uptake

The recent Covid-19 pandemic has profoundly impacted various aspects of our lives and served as a reminder to prepare for future outbreaks. Viruses, tiny biological machines on the nanometer scale, enter our cells to replicate by exploiting the cell's biological processes. They continue to multiply within a cell until all available resources are depleted. Eventually, the viruses rupture the host cell, leading to its death, and move on to infect other cells. The infection rate depends on the virus's ability to enter cells and replicate itself efficiently.

Viruses are simple structures comprising a membrane enclosing genetic material and could also have external spikes on their surface. The genetic material provides instructions for viral replication, while the spikes facilitate entry into host cells. There are multiple types of viruses, such as HIV, Influenza, Hepatitis, Bacteriophages, etc. During Covid-19, the SARS-CoV-2, or severe acute respiratory syndrome, coronavirus-2, attacked us. SARS-CoV-2 virus belongs to a family of coronaviruses that consist of HIV and the common cold, in SARS-CoV-1 [21, 22, 23]. The term "coronavirus" comes from the Latin word "corona," which means "crown" or "wreath." This Latin word was borrowed from the Greek word $\kappa o \rho \acute{\omega} \nu \eta$ "korōnē," which also means "garland" or "wreath." The name "coronavirus" was given by June Almeida and David Tyrrell, the first scientists to observe and study human coronaviruses [24, 25]. This family of viruses earned its name due to the distinctive crown-like spikes surrounding the viral shell, as depicted in Fig. 1A of cryo-electron microscopy images.

Researchers have been studying the various methods used by coronaviruses to enter the cell, such as macropinocytosis, membrane fusion, endocytosis, genetic injection, etc. [26,

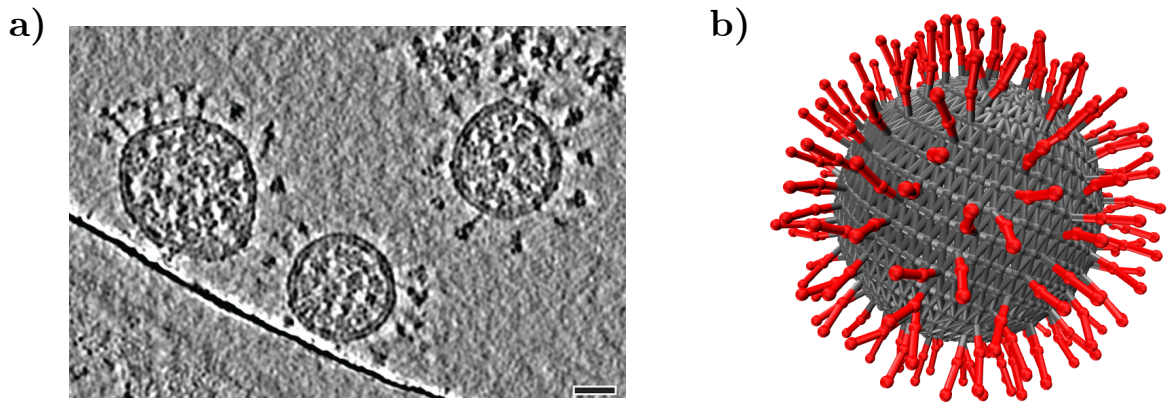

Figure 1 : *Experimental image and simulation illustration of the coronavirus:* (a) Cryo–electron tomography of SARS-CoV-2 virus. Spikes make the crown-like structure around the virus. [33], (b) Three-dimensional computational model of the coronavirus [34].

27]. Coronaviruses use an endocytosis process, among other processes, for cell entry. During endocytosis, the virus utilizes its spike protein to bind to the cell surface. This spike protein is specifically attached to the primary receptor on the cell surface, such as ACE2. Consequently, the cell membrane envelops the virus, effectively engulfing it and allowing for cellular entry. Cells permit the entry of the virus because they are unable to distinguish between the virus and regular cellular cargo. Consequently, treating the virus as cargo during endocytosis leads to its entry into the cell.

Cells have various receptors on their surface, such as membrane rafts [28], extracellular vimentin [29, 30], glycans [31] etc. These filaments act as coreceptors that also attaches to coronaviruses as suggested by recent studies [28, 32]. While the involvement of primary receptors in viral uptake has been extensively investigated, further work is necessary to gain a deeper understanding of the role played by these coreceptors.

Recently our group and other researchers have shown that a cell surface protein called "vimentin" could bind to both SARS-CoV-1 and SARS-CoV-2 [29, 30]. Vimentin is part of a cell's cytoskeleton and is usually found inside the cell. However, emerging evidence suggests that vimentin is also present on the cell surface [35]. In addition to vimentin, other cell surface components such as Heparan sulfate proteoglycans [36], neuropilin-1 [37], and TMPRSS2 [38] has also been found to bind with the spike protein of coronaviruses. These cell surface components act as coreceptors during viral entry, and blocking them

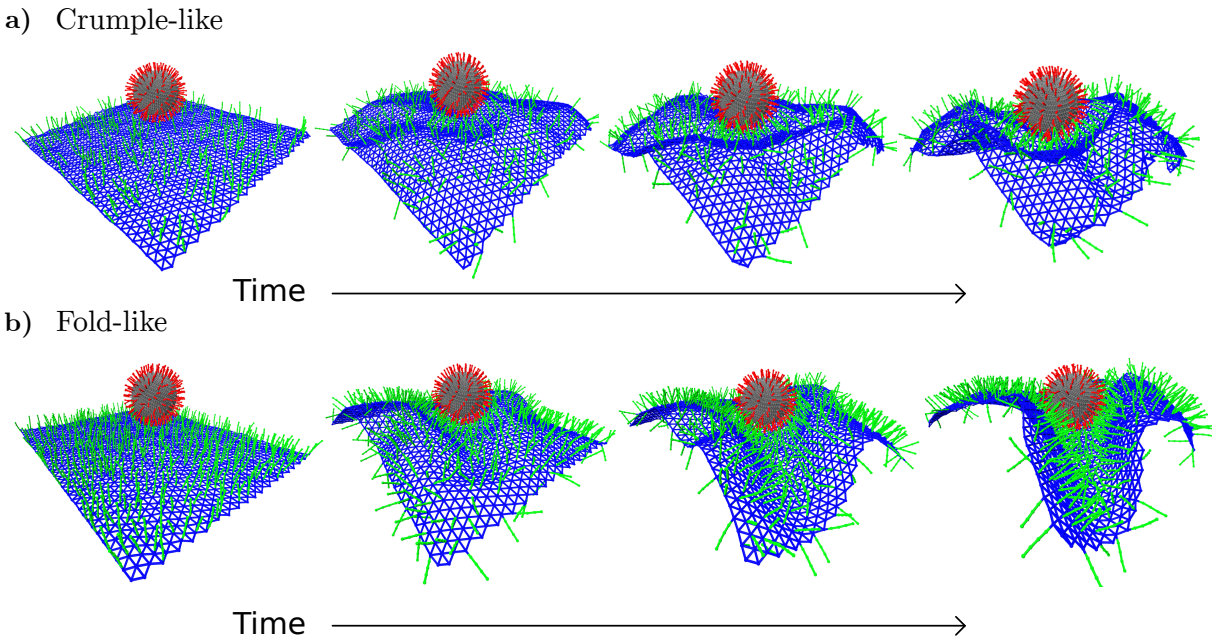

Figure 2 : *Simulation model showing cell surface with two wrapping pathways during endocytosis as a function coreceptor's physical parameters:* (a) Cell surface crumpling around the virus while wrapping (b) Cell surface creating folds while wrapping the virus.

could reduce the infection rate [29].

Since endocytosis is a mechanical process involving attachment and wrapping of the membrane around the virus, the mechanical properties of the coreceptors play a pivotal role in facilitating successful viral entry. Cell surface filaments have different physical properties, such as density, stretching, and bending rigidities, that could significantly influence endocytosis. Therefore, it is crucial to investigate how the physical properties of coreceptors affect the viral uptake process. Learning the mechanics of endocytosis could pave the path toward developing improved clinical strategies to fight against future pandemics.

We have developed a computational model to understand the role of the mechanics of coreceptors [34]. Our model contains a cell surface with tunable rigidity that could represent any cell surface. Additionally, we have filaments with diverse physical properties, such as varying density, bending rigidity, and stretching rigidity, to capture the characteristics of different cell surface components. Furthermore, our model features a spherical virus shell adorned with spikes, shown in Fig. 1B, allowing us to investigate the effects of different physical properties on various viruses.

Our computational framework has provided insights into the interplay between the mechanical properties of the cell surface and the spikes present on the virus during the endocytosis, as shown in Fig 2. By changing multiple physical parameters, we study the role of the mechanical properties of the cell surface, its surface components, and the viral spikes on the efficiency of viral uptake. We found an optimal density of cell surface components that maximizes the efficiency of viral uptake. Moreover, we find that at different density of cell surface components, two modes of uptake arises, cell surface folding or crumpling around the virus based on the mechanical property of the coreceptors and cell surface itself, as shown in Fig 2A and B, respectively. Additionally, we observed that high stretching rigidity played a more crucial role than high bending rigidity in facilitating the process. Consequently, we have demonstrated that the cells with different mechanical properties would have different viral uptake efficiency leading to different infection rates. We have detailed this part of the thesis in the next chapter.

1.2 Chromatin activity and cell nucleus morphology

In our endeavor to explore the mechanics and dynamics of biological systems, next, we investigated the cell nuclei morphological changes influenced by chromatin activity. The cell nucleus is a few micrometer-size organelle inside the cell containing genetic information. Genetic information governs various cellular processes, such as protein synthesis and cell division in a cell cycle. This genetic material is known as DNA, a long chain of nucleic acids, and could be as long as a meter. An intriguing question arises: how a meter-long material can fit within a micrometer-sized organelle? The answer lies in the intricate

multi-level wrapping of DNA. DNA is tightly wound around proteins called histones, forming nucleosomes at a few nanometer scales [39, 40]. These nucleosomes combine to create a chain-like structure known as chromatin, leading to the genetic material organizing within the cell nucleus.

Experimental evidence reveals that a healthy cell nucleus typically exhibits a spherical shape as depicted in Fig 3a (A) and b (A), whereas, in diseased cells, the nucleus displays abnormal morphologies, including bulges, wrinkles, even fragmentation [41, 42, 43, 44, 45, 46] as shown in Fig 3. These abnormal nuclear shapes not only serve as distinctive features but act as biomarkers for various diseases, such as metastatic cancer, premature aging (known as progeria or HGPS), Emery-Dreifuss muscular dystrophy, etc. [47, 48, 49]. The cell nucleus comprises an outer shell composed of intermediate filaments Lamin A and B, along with associated proteins. It encloses chromatin internally and interacts with the cytoskeleton externally. Chromatin itself is interconnected through proteins like Hp1-α [50, 51], and it is also connected to the lamin shell via proteins including LAP1, LAP2, emerin, and Man1 [52, 53]. Understanding the mechanisms behind abnormal nuclear shape formations is significant for two reasons. Firstly, it could provide insights into the development of improved therapies for treating these diseases. Second, from a material perspective, we still do not know how local blebs and wrinkles on the nucleus form.

Previous investigations have focused on understanding abnormal nuclear shapes from an external perspective. These works study changes at the nuclear lamina levels and interactions between cytoskeleton elements (microtubules, actin) and the nuclear lamina. [56, 46, 57]. Cytoskeletal elements exert forces on the nuclear shell through motor proteins or polymerization processes, leading to local deformations on the nuclear shell. However, recent experimental studies have shed light on the active environment within the nucleus itself, which arises due to transactional activity on chromatin [58]. Proteins such as condensin, cohesin, and RNA polymerases I and II interact with the chromatin and can exert pushing and pulling forces as they move along its length. Moreover, it has been demonstrated that silencing some of these proteins could result in a decrease in nuclear deformations [58]. Although considerable attention has been given to understanding the

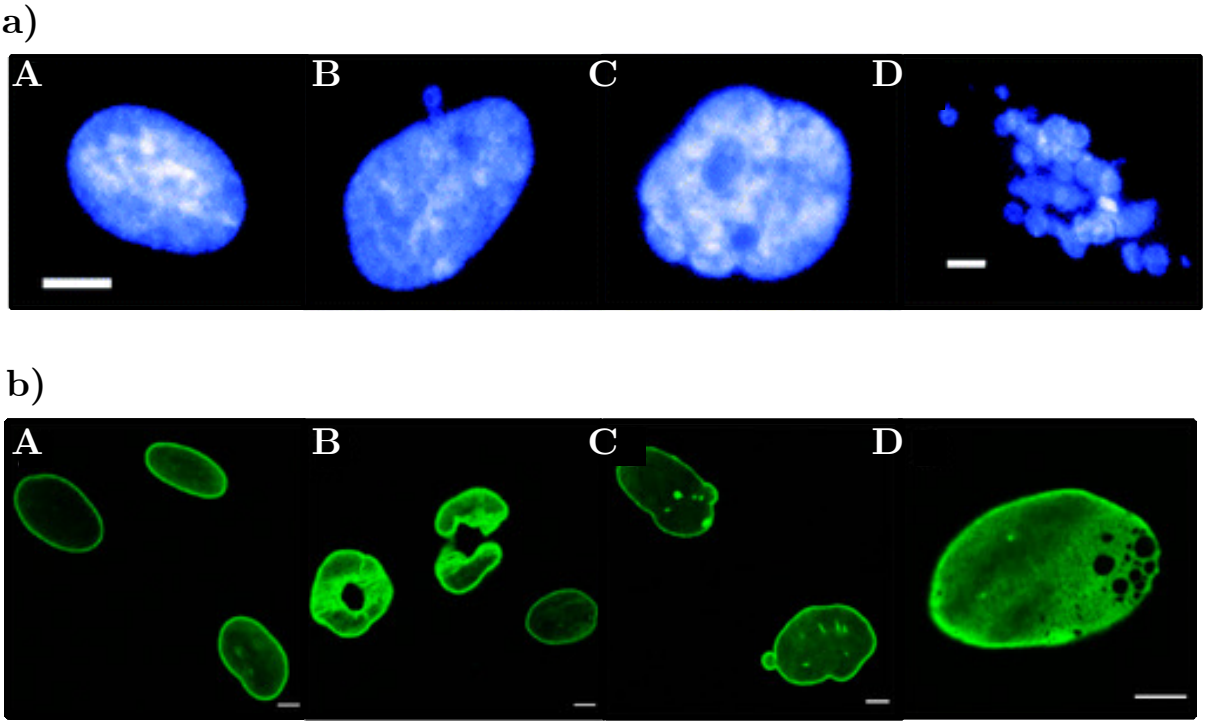

Figure 3 : *Abnormal nuclear shapes in human diseases cells* (a) Immunostained images of (A) a control nucleus and HGPS fibroblasts with (B) herniations in the nuclear periphery or nuclear blebbing or bulge formations, (C) folds and crevices, (F) fragmentation of the nucleus [54]. Scale bars = 10 μ m. (b) Nuclear abnormalities are commonly observed in human dermal fibroblasts obtained from patients with laminopathies. Green: lamin A/C staining using Jol2, (A) normal nuclei, (B) donut-like shaped nuclei, (C) nuclear blebbing, (D) honeycomb structures. Bars represent 5 µm. [55]

formation of abnormal nuclear shapes stemming from cytoskeletal activity [46, 57], the mechanisms underlying morphological changes in the nucleus resulting from chromatin activity remain poorly understood.

We approach this problem by developing a molecular dynamics-based simulation exploring the mechanisms of nucleus shape changes due to chromatin activity. Our model consists of a shell with biologically relevant connectivity representing a cell-nucleus shell. Shell contains a long polymer chain representing chromatin interconnected to itself via crosslinkers and connected to the shell via linkages, as shown in Fig. 2a schematic. We model the transcriptional factors as motors on the chromatin chain, acting forces on their neighboring beads within an influence radius. Motors are two types: contractile and extensile; the former pulls the neighboring beads towards it, and the former pushes them away. We model the motors moving on the chain by switching off a motor at a particular

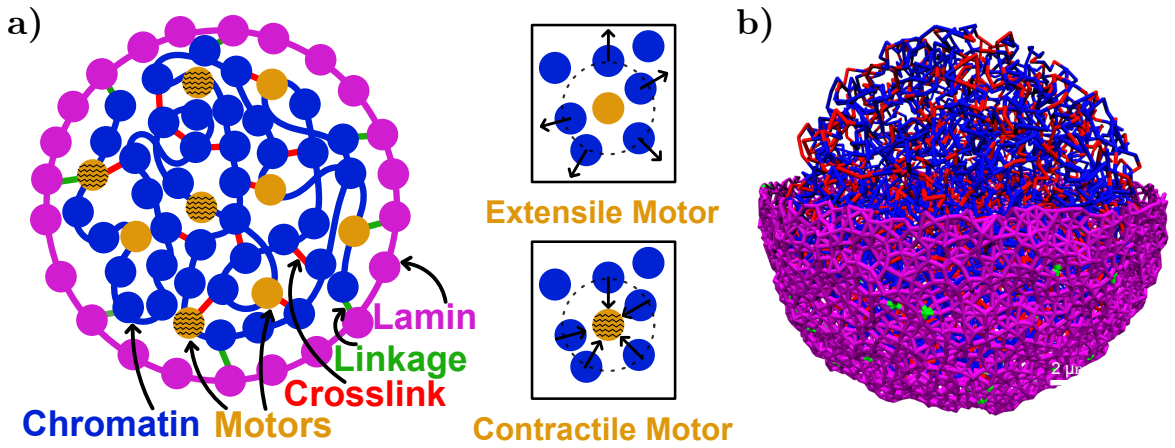

Figure 4 : *Chromatin model schematic illustrating all the components:* (a) 2D schematic of isolated nucleus model showing lamin shell contains chromatin chain interconnected via crosslinkers and connected to the shell by linkages. Two types of motors are shown, solid: extensile motors and stripe: contractile motors (b) 3D simulation shot of the model with the top half of the lamin shell removed, showing the chromatin chain inside.

chromatin bead and randomly switching on at some other bead with a Poisson process with a characteristic time, and this defines a motor's lifetime.

We have developed a molecular dynamics-based simulation to study the mechanisms behind changes in nuclear shape resulting from chromatin activity. The model consists of a shell with biologically relevant connectivity representing the cell nucleus. Within the shell, there is a long polymer chain representing chromatin, which is interconnected to itself through crosslinkers. The chromatin chain is also connected to the shell through linkages, as illustrated in the schematic in Figure 2a.

In our simulation, transcriptional factors are represented as motors positioned along the chromatin chain. These motors exert forces on neighboring beads within a specific radius of influence. We consider two types of motors: contractile motors, which pull neighboring beads towards them, and extensile motors, which push neighboring beads away. We employ a switching on and off mechanism to model the movement of motors along the chain. A motor is switched off at a particular chromatin bead and then randomly switched on at another using a Poisson process with a characteristic time, determining the motor's lifetime. Our model empowers us to investigate the dynamic interplay between chromatin mechanical properties and activity with nuclear shape changes by finding the

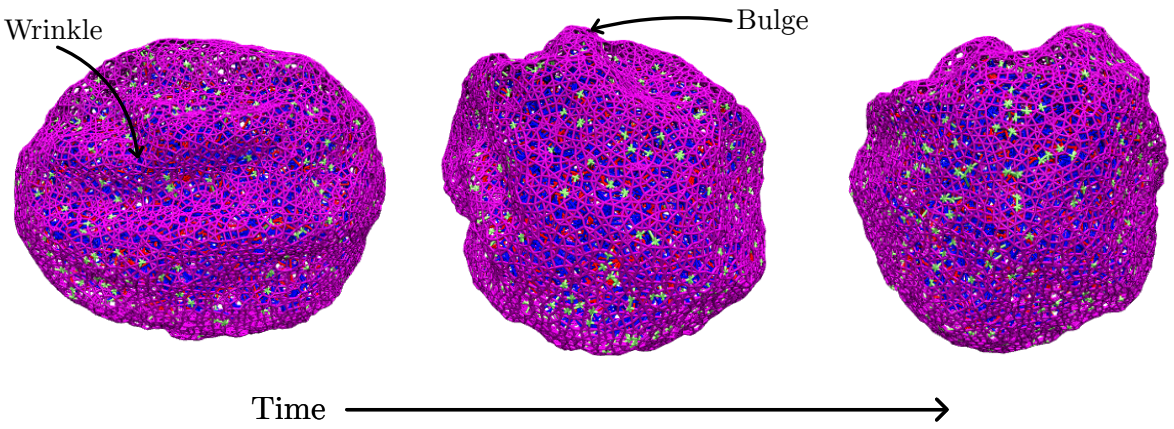

Figure 5 : *Time series snapshots of an isolated nucleus simulation model showing abnormal nuclear shapes such as bulges and wrinkles due to transcriptional activity on chromatin*

underlying mechanisms.

Our study demonstrated that our simplified cell nucleus model can reproduce abnormal nuclear shapes, including bulges and wrinkles. We observed that the number of bulges increases proportionally with the number of motors and crosslinkers. Moreover, we found that bulges become more stable when the number of crosslinkers is higher. This increased stability arises because more interconnected chromatin chains can move together over extended periods and distances, resulting in higher chromatin-chromatin correlation and more number of bulges. Additionally, we investigated the effect of motor lifetime on bulge dynamics. Surprisingly, we discovered that increasing the motor lifetime beyond a certain threshold does not extend individual bulges' lifespan but increases the overall number of bulges present.

Furthermore, we measured the chromatin-chromatin correlation length and observed that it increases as the number of motors and crosslinkers increases. This finding suggests a stronger long-range correlation between chromatin regions with higher motor and crosslinker activity. Overall, our simulation work demonstrates that active dynamics within the chromatin can contribute to the formation of abnormal nuclear shapes. Understanding these underlying mechanisms can guide the development of strategies for treating diseases associated with nuclear shape abnormalities. We have explained the details of our model and the implications of our findings in Chapter 3.

1.3 Confined cell motility

Cell migration is fundamental for many biological processes, such as embryonic development, wound healing, cancer metastasis, and tissue maintenance [59, 60, 61]. During migration, cells, which are typically around 20 μm in size, have to navigate through confined spaces, including the extracellular matrix and tissues, which can be as small as 3 to 4 μm. The cell contains multiple organelles, including the nucleus, cytoplasm, centrosome, cytoskeleton, and more. The cytoskeleton acts as an architecture of the cells, providing mechanical integrity and structure and assisting in cell migration. It comprises three major components: actin, microtubules, and intermediate filaments.

Actin filaments are primarily located at the cell's periphery in a filamentous form. They contribute to cell contractility and motility by generating forces at the cell edges due to myosin motors pulling and pushing on them. Actin also contributes to the mechanical strength of the cell by forming stress fibers that span the entire cell, as depicted in Figure 1. Microtubule filaments emanate from the centrosome and play a crucial role in keeping cell integrity and in cell migration and polarity. Additionally, microtubules act as bridges for intracellular cargo movement through motors. Intermediate filaments are a diverse family of proteins that include vimentin, Lamin A, Lamin B, Keratin, and others. Vimentin, in particular, is primarily located around the nucleus and within the cytoplasm. It also contributes to cell mechanical strength and aids in organizing the internal structures of the cell. The ability of cells to navigate through constricted spaces relies on the mechanical properties of the cellular cytoskeleton and the deformability of the nucleus.

In the context of cell motility, while microtubules and actin have received considerable attention, the role of vimentin has been relatively understudied. It is known that vimentin expression is upregulated during processes like epithelial-mesenchymal transition (EMT) or the transition from a stationary to a migratory state in cells [62, 63, 64, 65]. However, the precise reasons behind this upregulation of vimentin remain unclear. Recent experimental findings have revealed intriguing insights that in three-dimensional microchannels, cells lacking vimentin demonstrated increased cell speed, nucleus damage, and enhanced polarity. Interestingly, these observations contradict the behavior of vimentin-null cells

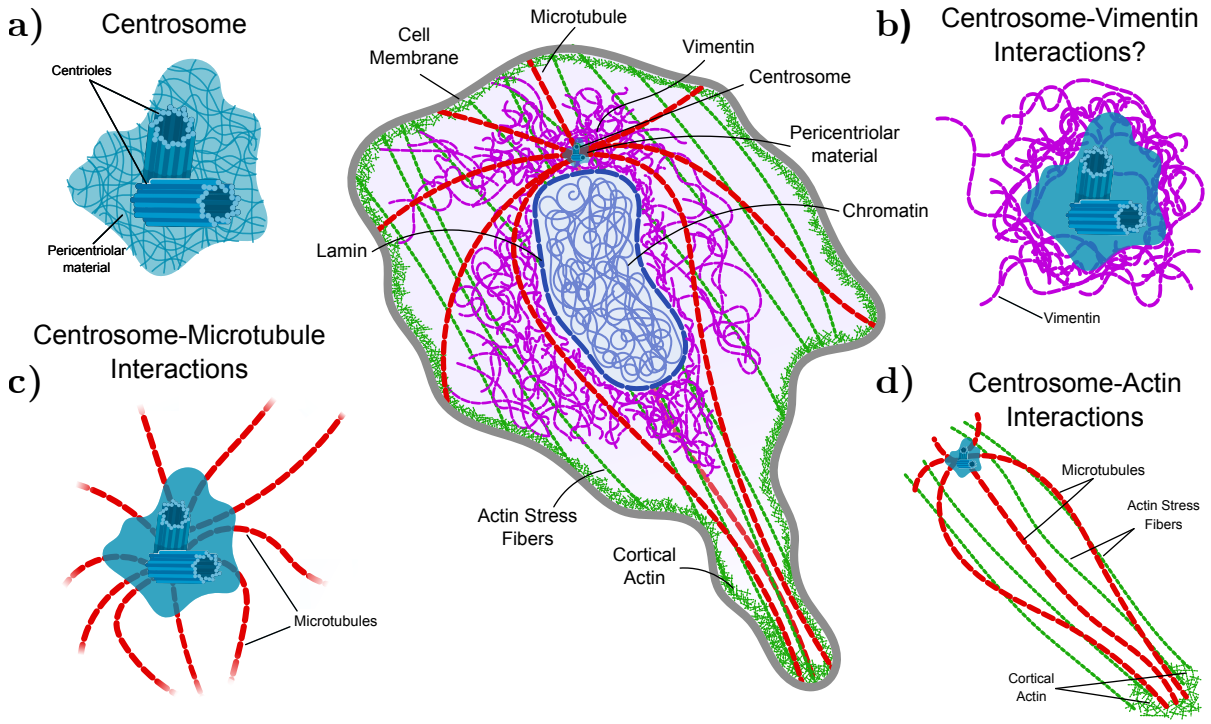

Figure 6 : *Internal structure of the cell showing nucleus, centrosome and cytoskeletal elements:* a) Structure of centrosome with centrioles and perinuclear material b) Centrosome is embedded in vimentin cage surrounding the nucleus c) Microtubules emanating out of centrosome d) actin filaments and stress fibers around the nucleus and centrosome

in two-dimensional settings. In 2D, vimentin-null cells do not show any directed motion and keep on making new lamellipodia in every direction, acting like their internal polarity mechanism is broken [66, 67]. These findings highlight the complex role of vimentin in cell motility [68].

To understand the role of vimentin in confined cell migration, we developed a computational model that incorporates all three cytoskeletal elements: actin, microtubules, and vimentin. Our model comprises an outer cortex, represented by a ring of interconnected beads and springs, and an inner ring that represents the nucleus, half the size of the cell. The cortex and nucleus are subject to area conservation constraints to simulate the nucleoplasm and cytoplasm. The cell cortex and nucleus are connected through springs to mimic the cytoskeletal structures.

As experiments, we considered in our model two types of cell lines: vimentin-null and wild-type. Vimentin-null cells lack the vimentin protein, and the wild-type cells have all the cytoskeletal components. Since vimentin-null cells lack the vimentin cytoskeletal

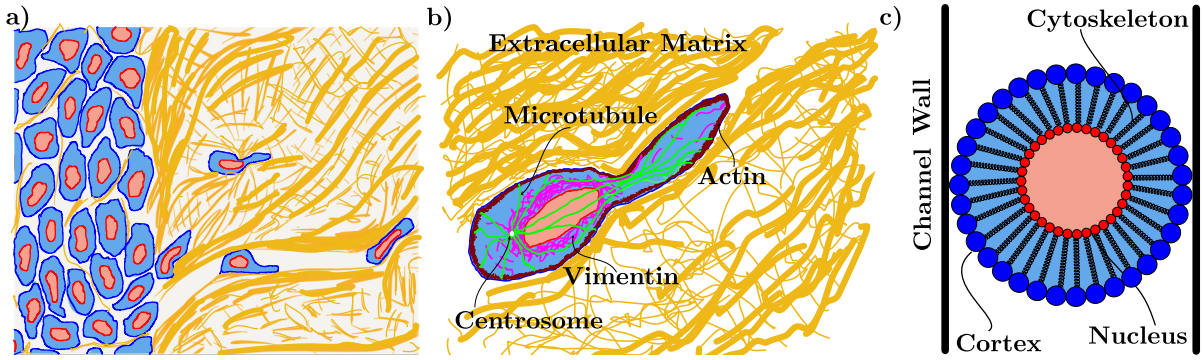

Figure 7 : *Modeling confined cell motility:* (a) Cells move through confining environments due to the extracellular matrix (in gold) and other cells. (b) Schematic of an individual cell with a cytoskeletal network containing actin, microtubules, intermediate filaments, a nucleus, and a centrosome connected to the nucleus via the protein dynein. (c) A simulation model for the cell: The cortex is made up of blue monomers connected with springs, and the nucleus is also made up of red monomers with springs connecting them. The bulk cytoskeletal network is simplified and modeled as springs connecting the nucleus and the cortex. The cell and nucleus contain cytoplasmic and nucleoplasmic material, each of which is modeled as area springs.

element around the nucleus and in the cytoplasm, we changed the strength of nucleus area conservation and cytoskeletal connections to simulate the vimentin-null cell line. Additionally, we incorporated active forces on the top half of the cell cortex to represent actin polymerization and another contact-driven force from the channel wall to simulate actin treadmilling at the outer surface of the confined channel [69].

Our computational model provides valuable insights into the contribution of vimentin to confined cell migration, its interplay with other cytoskeletal components, and the centrosome. Consistent with experimental observations, our model captures the slow speed of wild-type cells compared to vimentin-lacking cells in narrow confinement.

Furthermore, our model predicts a non-monotonic relationship between the speed of wild-type cells and the width of the confinement channel. We found that as the channel width decreases, the contact between the wild-type cell cortex and the channel wall increases, leading to a stronger driving force at the wall. However, this driving force competes with the overall deformability of the cell, which is influenced by the presence of cytoskeletal springs and the nucleus, thereby increasing effective adhesion. Consequently, we identify an optimized channel width where the wild-type cell achieves maximum speed. Similarly, we observe a similar phenomenon in vimentin-null cells, although the most

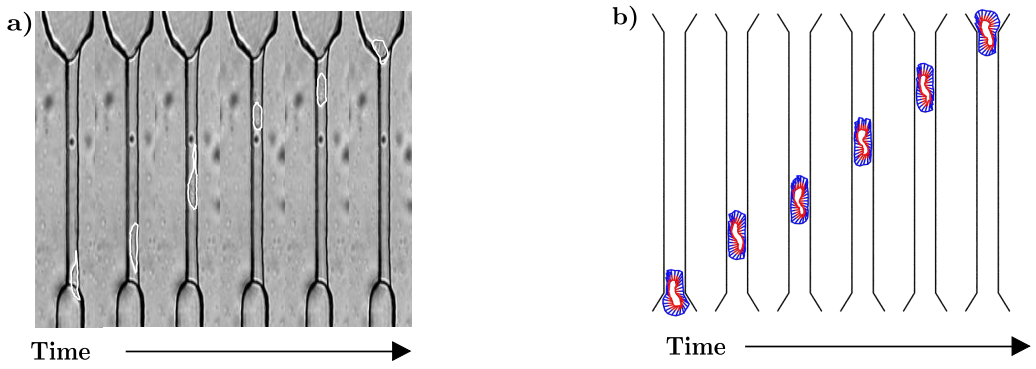

Figure 8 : *Model quantitatively agrees with cell speeds from micro-channel experiments:* (a) Time series of a wild-type mEF cell moving in a microchannel (b) Same as (a) but images are from a computational model.

optimal channel width is narrower compared to wild-type cells. Additionally, our model reveals the vimentin's protecting role for the nucleus from possible damage during confined cell motility.

To understand the high polarity of the vimentin-null cell in the channel, we introduce a polarity mechanism based on the position of the nucleus as a proxy for the position of the centrosome. In vimentin-lacking cells, the centrosome tends to be more tethered to the back of the cell, as there is no vimentin influencing its position. In contrast, cells with vimentin exhibit a stronger cytoskeleton that helps maintain the nucleus in a more centralized position, allowing the centrosome to move around the nucleus due to vimentin repolymerization. Change in the centrosome position enables the cell to change its direction more frequently within the confinement.

By combining these discoveries, our computer model helps us better understand how vimentin affects the movement of cells in tight spaces, protects the nucleus, and influences the direction of cell movement.

1.4 Tissue under compression

Next, we focused on addressing physical problems in biology at a larger scale by investigating the behavior of cells within tissues or tumors. Tissues are complex assemblies of cells that collectively form larger structures, such as organs, within our bodies. Within tissues, tumors form when specific cells divide uncontrollably, presenting a challenge for

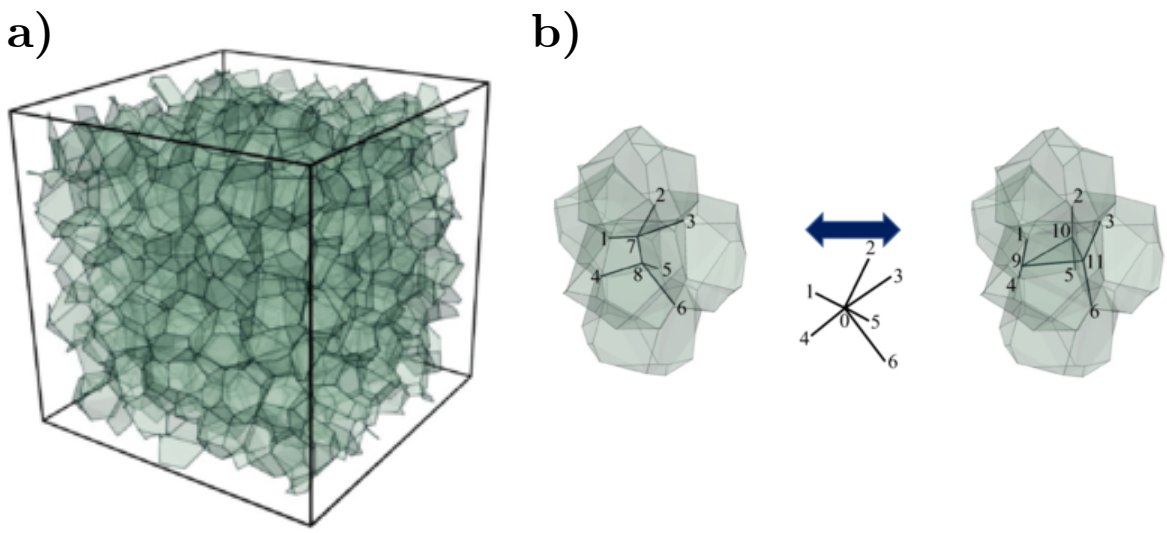

Figure 9 : *Three-dimensional vertex model:* (a) Each polygon represents a a cell which have volume and surface area conservation to maintain the integrity of a cell (b) In three dimensions, cells can change neighbors through face to line or vice-versa transisition [70].

treatment due to their invasive nature, ability to migrate to different locations in the body, and capacity to initiate new tumor growth. To address this challenge, it is essential to understand physical conditions that could trigger tumor cells to detach from the primary tumor site. By understanding the mechanical factors that affect tumor cell migration, we can develop strategies to predict and reduce their migration rates. One key aspect of tumor development and growth is the confinement experienced by these tissues. Tumors grow under external pressures due to their proximity to other biological structures, such as surrounding tissues, organs, or bones. Recent experimental studies have highlighted the influence of mechanical properties exhibited by collective cells on tumor growth. However, predicting whether an individual cell within a tumor will ultimately decide to leave remains challenging.

To address this challenge, I used the vertex model of tissues. Vertex models in two dimensions have been useful in studying different aspects of how organisms develop, particularly in understanding how the shape of tissues is formed. These models have helped us discover the importance of tensions created between cells in influencing tissue mechanics. Previous studies have applied the Vertex model to explore a range of phenomena, such as cell mixing and the transition from solid to fluid behavior, in organisms like Drosophila and Hydra [71, 72, 73, 74, 75]. In the two-dimensional version of this model, the tissue

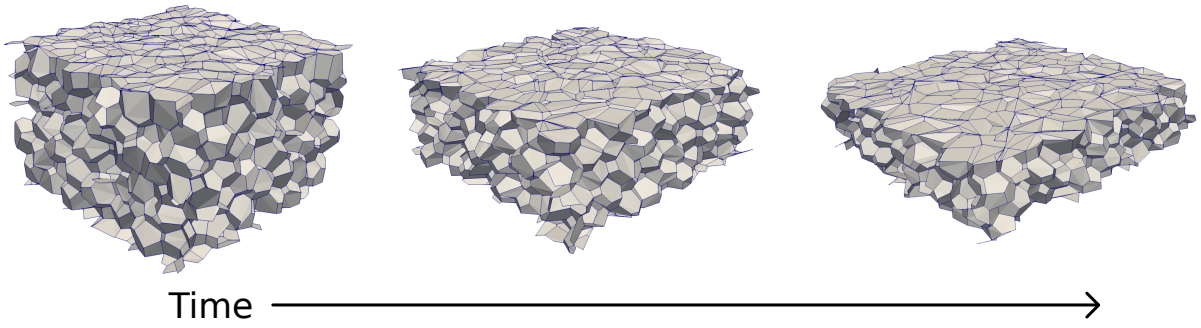

Figure 10 : *Time series snapshots of parallel plates uniaxially compression the vertex model of tissue*

is represented by a space-filling polygon tiling, with no gaps or holes between polygons to model the confluency of tissue. Each polygon corresponds to an individual cell, sharing edges with neighboring polygons. The area and perimeter of each polygon are governed by conservation potentials that regulate the compression or extension of the cells. Since tumors exist as three-dimensional structures, I have employed a three-dimensional framework of the vertex model [76, 70]. This three-dimensional vertex model resembles its two-dimensional counterpart, but instead of polygons, polyhedra are employed to fill the space, with shared faces and edges representing individual cells. These polyhedra incorporate volume and surface area conservation potentials to maintain the integrity of the cells. As seen in experimental observations, these vertex models also incorporate the ability of cells to swap positions with one another, depending on specific parameters. In the two-dimensional model, when to exchange neighbors is determined by edge length, and face-to-line transitions determine the neighbor change conditions in the three-dimensional vertex model.

We compressed the 3D vertex model between parallel plates to investigate the physical condition which could lead to cells detaching from a growing tumor. In our model, compression acts as a proxy for tissue growth. Previous studies have shown that tumors are more rigid than the surrounding healthy tissues [77], so we focused on two physical conditions. First, the tissues are composed of cells with solid-like properties, and another is composed of cells with fluid-like properties. Through our simulations, we observed that the tissue consisting of cells with fluid-like behavior could attain their desired mechanical state

under compression by swapping positions with neighboring cells. In contrast, the tissue composed of solid-like cells encountered difficulty exchanging positions with neighboring cells, thus impeding their ability to achieve the desired mechanical state. We are still exploring more avenues in this work. In particular, we aim to investigate the transition point from solid to fluid behavior in three-dimensional tissues under strain. By continuing this work, we anticipate uncovering valuable insights into the mechanics of tumor growth and the physical factors influencing tumor-like cell behavior.

1.5 Outline

In this thesis, I will address problems focusing on the importance of mechanics in biology at multiple scales, from viruses, at a nanometer length scale, through the internal structures of cells, up to the scale of tissues visible to the eye, shown in Fig. 11.

Chapter 2 focuses on developing a computational model to study the interaction between viruses and cell surface filaments. The goal is to understand how individual components' mechanical properties contribute to the viral uptake process. This model represents a pioneering approach that explores the behavior of cell and viral surface components. Specifically, we examine how the density of cell surface filaments and viral spikes influences endocytosis. Furthermore, we investigate how variations in cell surface rigidity can lead to different modes of uptake, such as folds or crumples. Considering the diverse physical properties of the proteins present on both cell and viral surfaces, we analyze the impact of stretching and bending rigidities on the efficiency of endocytosis. In sum, we concluded that the mechanical properties of coreceptors are a vital factor to consider that could help us develop clinical strategies against viral infection.

In Chapter 3, we delve into the cell nucleus by looking at chromatin dynamics and its impact on the formation of abnormal cell nuclear shapes. I developed a detailed yet simple computational model to investigate this phenomenon that focuses on an isolated nucleus. My goal was to understand the mechanisms underlying the emergence of bulges and wrinkles on the nuclear surface. In this model, I specifically examined the influence of transcriptional activity strength and the number of active motors on the formation of

nuclear bulges. I created a two-dimensional projection of the three-dimensional nucleus to quantify the number of bulges and their sizes. Additionally, I considered factors such as the lifetime of transcriptional factors, the number of crosslinkers, and their collective contribution to forming irregular nuclear shapes. In this work, we discovered that higher motor strength, increased crosslinker density, and longer motor lifetimes result in more stable bulges contributing to enhanced chromatin correlation motion. By unraveling the possible underlying mechanism for the formation of abnormal nuclear shapes, our work contributes to the broader understanding of these processes and offers promising avenues for possible therapeutic interventions.

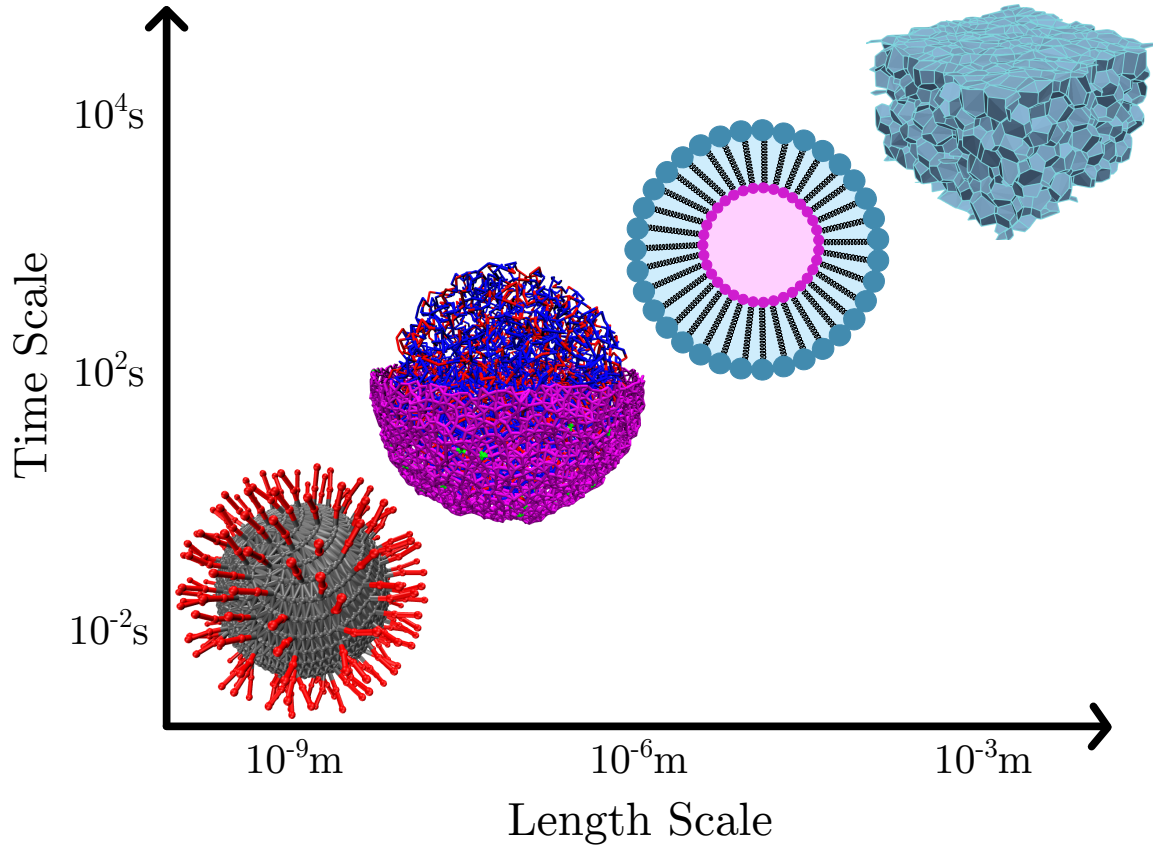

Figure 11 : *Living systems across time and length scales:* In this thesis, we worked on living systems spanning three orders of length and time. It spans from viruses at the nanometer scale and their rapid uptake within a few milliseconds, detailed in Chapter 2, to chromatin structures within cell nuclei spanning a few micrometers that exhibit bulge formations occurring over minutes, detailed in Chapter 3. Moving up in scale, we encounter cells at tens of micrometers, with motility in confinement taking place over a few hours, detailed in Chapter 4. Further up, tissues, at the millimeter scale, experience compression processes that unfold over the course of a few days, detailed in Chapter 5.

Chapter 4 of the thesis focuses on the problem of confined cell motility and polarity.

To address this issue, we developed a computational model that incorporates multiple biological entities interacting with each other to provide insights into cell motility and polarity behaviors within confined environments. Our computational model comprises a cell cortex that connects to the nucleus through cytoskeletal springs. To simulate motility within the confinement, we included actin polymerization forces at both the cell's leading edge and the channel wall. By employing this model, we investigated the observed phenomenon of vimentin-null cells exhibiting faster movement in narrow confinement compared to wild-type cells. We also tracked the nucleus's shape to explore vimentin's potential protective role during cell motility. Furthermore, we developed a polarity model to examine the influence of the centrosome and nucleus in both wild-type and vimentin-null cell lines. Our findings demonstrate that our computational model captures experimental observations and provides predictions for the persistence of both cell types in confined environments. This work sheds light on the crucial role of vimentin, which has been relatively understudied, in cell motility, nucleus protection, and the guidance of migrating cells toward new directions. Our work could contribute to advancements in various fields, including cell biology and disease research.

In Chapter 5, we explore the behavior of cells within a three-dimensional tissue under uniaxial strain. To tackle this problem, we utilize a three-dimensional vertex model, which offers a framework for studying cellular dynamics in tissues. This model consists of space-filling polyhedrons representing individual cells, with faces and edges shared between neighboring cells, with volume conservation and surface area conservation for each face to maintain the mechanical integrity of a cell. Cells can also exchange neighbors through face-to-line or vice versa transitions governed by specific threshold parameters. To understand under what conditions cells could leave a growing tissue or tumor, we compress two distinct tissue types: solid-like cells and fluid-like cells. By examining how cells behave under compression, we aim to unravel the mechanical conditions that facilitate cell migration away from the tumor. Our findings reveal that cells with fluid-like properties exhibit a greater chance to change neighbors, even under compression that relaxes the stress due to compression. In contrast, solid cells struggle to achieve such

neighbor change in response to compression. This work contributes to our understanding of the mechanical factors that influence cell behavior within tumors and provides valuable insights for experimental studies focused on finding the conditions that could prompt cells to leave tumor masses.

In concluding Chapter 6, I will summarize the thesis work presented here. Furthermore, I will discuss potential future research directions that build upon the foundation laid in this thesis. By exploring the multiscale interactions and feedback mechanisms between different levels of biological organization, from the chromatin level through intracellular to cell-cell interactions to the tissue level, we could gain deeper insights into the fundamental physics that governs biological processes [78].

Chapter 2

How cells wrap around virus-like particles using extracellular filamentous protein structures?

Viruses are relatively simple in structure as they consist of a container and genetic material. The container material ranges from solid-like proteins to fluid-like lipids [79, 80]. For the latter type of container, evolutionary pressures have led to the emergence of filamentous spike proteins that protrude out from the container. Such viruses are otherwise known as coronaviruses, examples of which include the common cold, HIV, and, of course, SARS-CoV-1 and SARS-CoV-2 [21, 22, 23]. The number of spike proteins may indeed vary from virus to virus (for a given type of coronavirus) [21, 22, 23]. Moreover, the average spike protein density may change from one type of coronavirus to the next. For instance, the average spike protein density is typically two orders of magnitude in HIV as compared to other coronaviruses [81]. Of course, spike protein density is merely one aspect of their characterization. Much work has been done to characterize their binding affinities, and some work has been done to characterize their mechanics [82, 83, 84, 85, 86]. In other words, the spike proteins have their own mechanical/conformational degrees of freedom to serve as additional knobs for viruses to optimize their function, which is presumably to replicate.

Since the contents of a virus are minimal, in order to replicate, viruses must enter cells to hijack their biological machinery. Viruses enter cells via multiple pathways. Two of the dominant pathways for coronaviruses are membrane fusion, and endocytosis [87, 88]. In the former, there exists an appropriate receptor on the cell surface, and an additional player arrives just below/at the cell surface to assist the virus in opening its genetic contents. In the latter, the cell surface deforms to wrap around the virus and ultimately pinches it off to enter the cell as a virus-containing vesicle. Clathrin and dynamin are major players in one endocytotic pathway. Other pathways include cytoskeletal filaments, such as actin [27, 89]. Of course, a cell surface contains complex structures with multiple coreceptors interacting with spikes of the virus [28, 32]. An identified receptor of the Sars-CoV-2 virus is ACE2; however, other coreceptors such as membrane rafts [28], extracellular vimentin [29, 30], glycans [31] also play a role in endocytosis in particular. A subset of such coreceptors, such as extracellular vimentin, can be filamentous with their own degrees of freedom [35] and can, therefore, take on a life of their own, if you will,

affect viral uptake by the host cell.

Following our initial mostly experimental study of how extracellular vimentin impacts viral uptake [29], here, we present a computational model in which *both* the cell-like construct and the virus-like construct contain their own filamentous structures protruding from their surfaces and study the impact of these additional degrees of freedom on viral wrapping. Indeed, much research has focused on how the size and shape of the virus impact viral wrapping [90, 91, 92] with spherocylindrical objects wrapping (and pinching off) more efficiently than spheres [93]. In addition, a recent genetic algorithm approach demonstrated that spheres with patchy sites that are arranged in the lines along the sphere, as opposed to randomly, endocytose more efficiently [94]. Filamentous structures on viral surfaces have been found to lower energy barriers for binding to the cell [95, 96]. However, given the presence of filamentous proteins emanating from, or bound to, cell surfaces, how do filamentous objects on the *outside* of a cell assist in viral wrapping?

To begin to answer the above question, we have organized the chapter as follows. We first present the computational model with several simplifying assumptions. The first is that the cell surface is modeled as a deformable sheet with bending and stretching energy costs, representing the underlying cell cortex supporting the lipid bilayer. Second, as extracellular vimentin is our main filamentous protein candidate, vimentin self-assembles into filamentous, hierarchical structures whose tetramers are six times longer than the thickness of a cell membrane [97]. There is some evidence for extracellular vimentin adhering to the cell surface via glycans [98]; however, vimentin may stick directly to the lipid bilayer or to the cell cortex via plectins. Since many of the details regarding how extracellular vimentin interacts with the surfaces of cells have yet to be discovered, we assume that the extracellular filamentous protein structures, or extracellular components, tether directly to the cell surface. Finally, the third simplifying assumption is that while the viral container will contain filamentous spikes emanating from it, the container will be a deformable shell with elastic interactions. Even with such simplifying assumptions, the model is still very rich in its viral wrapping phase space. We then present the results of the modeling after varying the density of the filamentous, extracellular components,

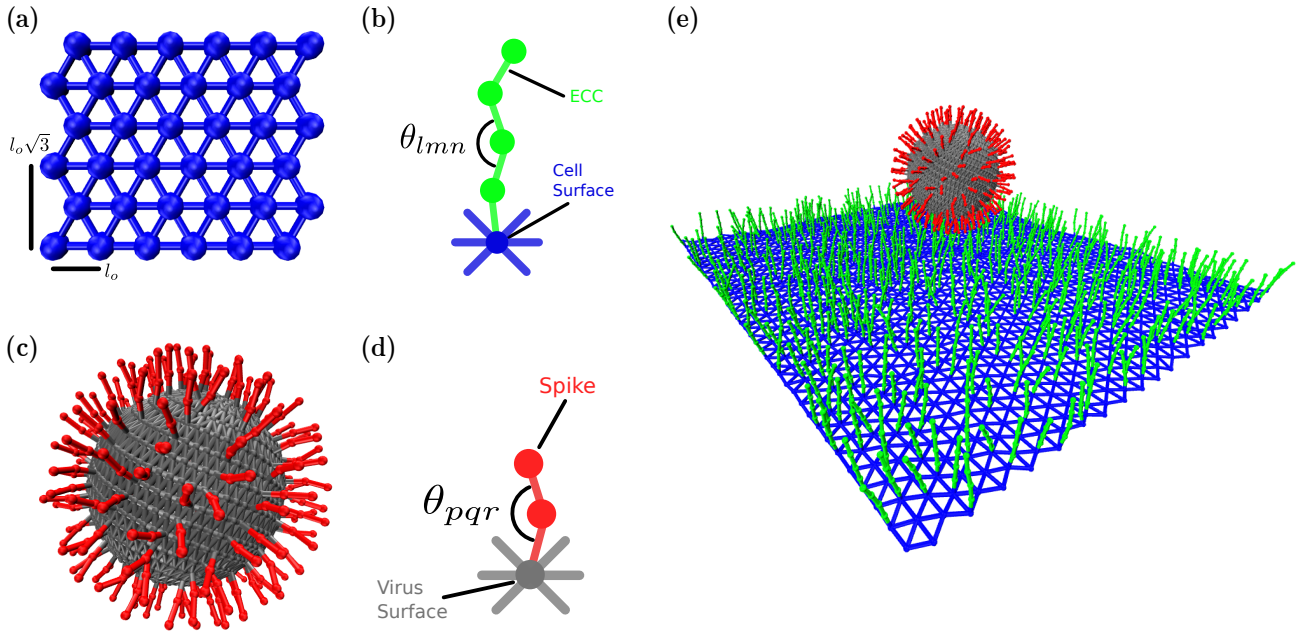

Figure 12 : *Schematic illustration of the components of the coarse-grained computational model* (a) The cell surface is constructed as network of equilateral triangles (blue particles and edges) (b) Extracellular components are modeled as a single polymer with bending and streching rigidity (c) The virus surface (gray) is composed of particles on a sphere connected each other via springs and containing spikes (red) emanating from the surface (d) Spike proteins are quantified as single polymers with bending and stretching rigidity (e) Combining all the components of the computational model yields a virus with spikes interacting with a cell surface with extracellular components.

and the filamentous extra viral components, as well as the mechanics of each component and of the deformable sheet, to explore their implications for viral wrapping. We then conclude with a discussion of the evolutionary pressures of viral structure and mechanics, given our results.

2.1 Computational model and methods

To understand the role of the filamentous structures on the outside of both a cell and a virus on viral uptake, we model viral wrapping via coarse-grained Brownian dynamics simulations. Here are the relevant players and how they are incorporated into the model and their respective interactions with the other players.

Cell surface: We model the cell surface as a deformable sheet, as shown in Fig 12 (a). The sheet is made up of particles, shown in blue, that are connected via springs.

Nearest-neighbor particles in the sheet interact via harmonic spring potential $V_{Spring} = \frac{K_{NN}^{CellSurface}}{2}(r_{ij} - l_o)^2$, where $K_{NN}^{CellSurface}$ is the strength of spring interaction, r_{ij} is the distance between nearest neighbors and l_o is the edge length of the equilateral triangle. Bending rigidity is introduced in the surface with a spring interaction between second nearest neighbors $V_{Spring} = \frac{K_{SNN}^{CellSurface}}{2}\left(r_{ik} - l_o\sqrt{3}\right)^2$, where $K_{SNN}^{CellSurface}$ is the strength of second spring interaction, r_{ik} is the distance between second nearest-neighbors and $l_o\sqrt{3}$ is the second nearest-neighbor distance. This second nearest-neighbor interaction acts as a brace to constrain the distance between the two more distant particles such that there is an effective hinge between the two triangles spanning the brace, and given the additional braces, we can explore the bending cost of the deformable sheet. This interpretation is further supported by an additional soft-core repulsion between particles (detailed below) with the particle size relative to the smallest equilateral triangle size set such that the particles cannot pass through this triangle to decrease twisting. Moreover, the presence of the filamentous structures on one side of the sheet also helps to minimize twisting.

Parameters	Value	Reference
$K_{NN}^{CellSurface}$	$1\ pN/nm$	
$K_{SNN}^{CellSurface}$	$0/3.5/7/10.5/14\ k_BT$	
K_{Spring}^{Virus}	$0.05/0.5/1/5/10/50\ pN/nm$	[83] [99][100]
K_{Spring}^{Spike}	$10^{-2}/10^{-1}/10^{0}/10^{1}/10^{2}\ pN/nm$	[84]
K_{Spring}^{ECC}	$10^{-2}/10^{-1}/10^{0}/10^{1}/10^{2}\ pN/nm$	[101]
$K_{Spring}^{Receptor}$	$50\ pN/nm$	[102]
$K_{Spring}^{ECC-Receptor}$	$5\ pN/nm$	[103]
$K_{Bending}^{Receptor}$	$120\ k_BT$	-
$K_{Bending}^{ECC}$	$24\ k_BT \times 10^{-2}/10^{-1}/10^{0}/10^{1}/10^{2}$	-
$K_{Bending}^{Spike}$	$24\ k_BT \times 10^{-2}/10^{-1}/10^{0}/10^{1}/10^{2}$	-
$\epsilon_{Attractive}^{ECC-Spike}$	$25\ k_BT$	-
$K_{Soft-Repulsion}$	$1\ pN/nm$	-
D	$1\ \mu m^2/s$	-

Table 1 : Table of parameters used unless otherwise specified.

Again, we are modeling the cell surface as a deformable sheet. With this assumption, we can also explore local, nontrivial shapes of the underlying cortex, which, in turn, drives the plasma membrane shape. On the other hand, since earlier work demonstrates that the head domain of vimentin can also associate with a plasma membrane [104], we will address the potential changes if the sheet were to be fluid-like in the discussion.

Extra-Cellular Components (ECC): The filamentous ECCs are semiflexible polymers also modeled as particles connected with springs, as shown in Fig 12(b). Each ECC

consists of four particles, with the first one connected to a cell surface particle, as shown in Fig. 12(e). Since the cell surface microenvironment may be random, as opposed to a pattern, we place the ECC randomly on the deformable sheet. While a major candidate ECC we consider is extracellular vimentin, given its increasingly pronounced role in viral infection [35], one can also consider heparan sulfate [105], proteoglycans, glycolipids [26], or sialic acids [106]. Each of the candidates may have different mechanical properties based on the protein's physical properties and cell type. To model such properties, each of these co-receptors has bending rigidity given by $V_{Bending} = \frac{K_{Bending}^{ECC}}{2}\left(cos(\theta_{lmn}) - 1\right)^2$ where θ_{lmn} is the angle between three consecutive particles in co-receptors and $K_{Bending}^{ECC}$ is the strength of the bending force. We maintain the equilibration angle to be zero or a straight polymer, such that there is an energy cost for bending. The stretching energetic cost is governed by $V_{Spring} = \frac{K_{Spring}^{ECC}}{2}\left(r_{ij} - \sigma_o\right)^2$, where K_{Spring}^{ECC} is the strength of spring interaction, r_{ij} is the distance between nearest neighbor and σ_o is the diameter of a ECC particle. Finally, we assume that these filamentous extracellular components are bound to the cell cortex just beneath the lipid bilayer [107, 36, 105].

Receptor: A short receptor is placed in the middle of the cell surface and is the same as the ECC receptor with different values for $K_{Spring}^{Receptor}$ and $K_{Bending}^{Receptor}$ as specified in Table 1. The initial condition is the virus-like particle bound to the short receptor.

Virus Surface: The deformable virus surface is initialized by generating particles on a sphere. The particles are arranged in a Fibonacci sequence. We then implement a Delaunay triangulation to identify the edges between these particles. All particles on the sphere are connected with a harmonic spring potential $V_{Spring} = \frac{K_{Spring}^{Virus}}{2}\left(r_{ij} - r_o\right)^2$, where K_{Spring}^{Virus} is the strength of the spring and r_o is the equilibrium distance found by the triangulation. This construction of a deformable, elastic virus surface, with ultimately filamentous structures emanating from it, is a simplifying assumption as viruses with spike proteins typically consist of fluid-like containers but, nonetheless, provides a starting point for the modeling.

Spikes on Virus: Spikes are two particles joined by harmonic springs, as shown in

Fig. 12(d), which are also joined to the virus surface by another harmonic interaction, as shown in Fig 12(c). Since spikes can take on multiple configurations [33, 108], they also have bending potential with $V_{Bending} = \frac{K_{Bending}^{Spike}}{2}(cos(\theta_{pqr}) - 1)^2$. The connecting spring potential is given by $V_{Spring} = \frac{K_{Spring}^{Spike}}{2}(r_{ij} - r_o)^2$, where K_{Spring}^{Spike} is the strength of the spring and σ_o is the particle's diameter. We place the spikes on the virus's surface such that the typical distance between two neighboring spikes is between 3-15 nm, the range found in experiments [83, 109].

Spike-receptor interaction: The virus is connected to the primary receptor via a harmonic spring interaction, $V_{Spring} = \frac{K_{spring}^{Spike-Receptor}}{2}(r_{ij} - \sigma_o)^2$, where $K_{spring}^{Spike-Receptor}$ is the strength of the spring and r_o is the equilibrium distance. The receptor is made up of four particles connected via harmonic spring and has some bending rigidity.

Spike-ECC interaction: Virus spikes and extracellular components may interact via specific binding domains and charge interactions [96, 110, 105]. We model all the possible interactions with a simple, attractive potential, given by Eq. 1, which attracts in some range with the strength of $\epsilon_{Attractive}^{ECC-Spike}$. Although the virus spikes may have multiple receptor binding domains [111, 32], we took a conservative approach and only allowed one ECC to bind to one spike protein for modeling lock and key interactions [112]. Thus, our sticky potential only attracts the top ECC particle and top spike particles to each other. Therefore, r_{ij} is the distance between ith top spike particle and the jth top ECC particle, and σ_o is the diameter of the particle, or

$$V_{LJ} = \begin{cases} 4\epsilon_{Attractive}^{ECC-Spike}\left[\left(\frac{\sigma_o}{r_{ij}}\right)^{12} - \left(\frac{\sigma_o}{r_{ij}}\right)^{6}\right] & r \leqslant 2\sigma_o \\ 0 & r > 2\sigma_o. \end{cases} \tag{2.1}$$

*S*oft-core repulsion: All components of the model have volume exclusion due to soft-core repulsion given by Eq. 2, where $K_{Soft-Repulsion}$ is the strength of the soft repulsion, r_{ij} is the distance between the centers of two particles, and σ_o is the diameter of a particle. The repulsion force acts only when the distance between particles is lower than the

diameter of the particle, or

$$V_{Soft-Repulsion} = \begin{cases} \frac{K_{Soft-Repulsion}}{2}\left(r_{ij} - \sigma_o\right)^2 & r_{ij} \leqslant \sigma_o \\ 0 & r_{ij} > \sigma_o. \end{cases} \tag{2.2}$$

Method: We implement Brownian dynamics to quantify the dynamics of the model. The equation of motion is given by Eq. 3 below, where r_i is the position of an ith particle, F_i^c is the sum of conservative forces acting on the ith particle, and $\xi(t)$ is the Gaussian white noise to simulate thermal fluctuations and follows $< \xi(t) >= 0$ and $< \xi_i(t)\xi_j(t') >= 0$. The sum of conservative forces on the ith particle is $F_i^c = F_i^{Spring} + F_i^{Bending} + F_i^{LJ} + F_i^{Soft-Repulsion}$. We obtain these forces by taking derivatives of the above potentials with respect to the ith particle coordinate ($F_i = -\frac{\partial V}{\partial r_i}$). We integrate the equation of motion by the Euler-Murayama method, or

$$\dot{r_i} = \mu F_i^c + \sqrt{2D\xi(t)}. \tag{2.3}$$

Scales: Our Brownian dynamics simulation is a coarse-grained simulation. All simulation quantities are normalized via length, time, and force scales. We can convert simulation quantities to biologically relevant quantities by the following definitions: one unit simulation length is defined as 10 nm, one unit simulation time is 1μs, and one force unit is 10^{-1}pN. All simulation quantities are expressed in terms of these basic units. We run the total simulation with dt 10^{-4} for 10^8 simulation steps or 50 ms and recording positions at each 25 μs. Total run time is comparable to the typical viral endocytosis time [113, 114]. To find the optimal conditions for endocytosis in our system, we vary the density of ECC and virus spike, spring strength and bending rigidity of ECC and virus spike, and spring strength of virus. Finally, the bending rigidity of the cell surface can be written in terms of k_BT. Since bending rigidity is encoded in the second nearest-neighbor springs, multiplying that spring constant with the area of the triangle made up of those springs, with side $l_o\sqrt{3}$, gives the bending rigidity. Converting to a dimensionless bending rigidity, $\tilde{K}_{SNN}^{CellSurface}$, using our normalized length and force scales,

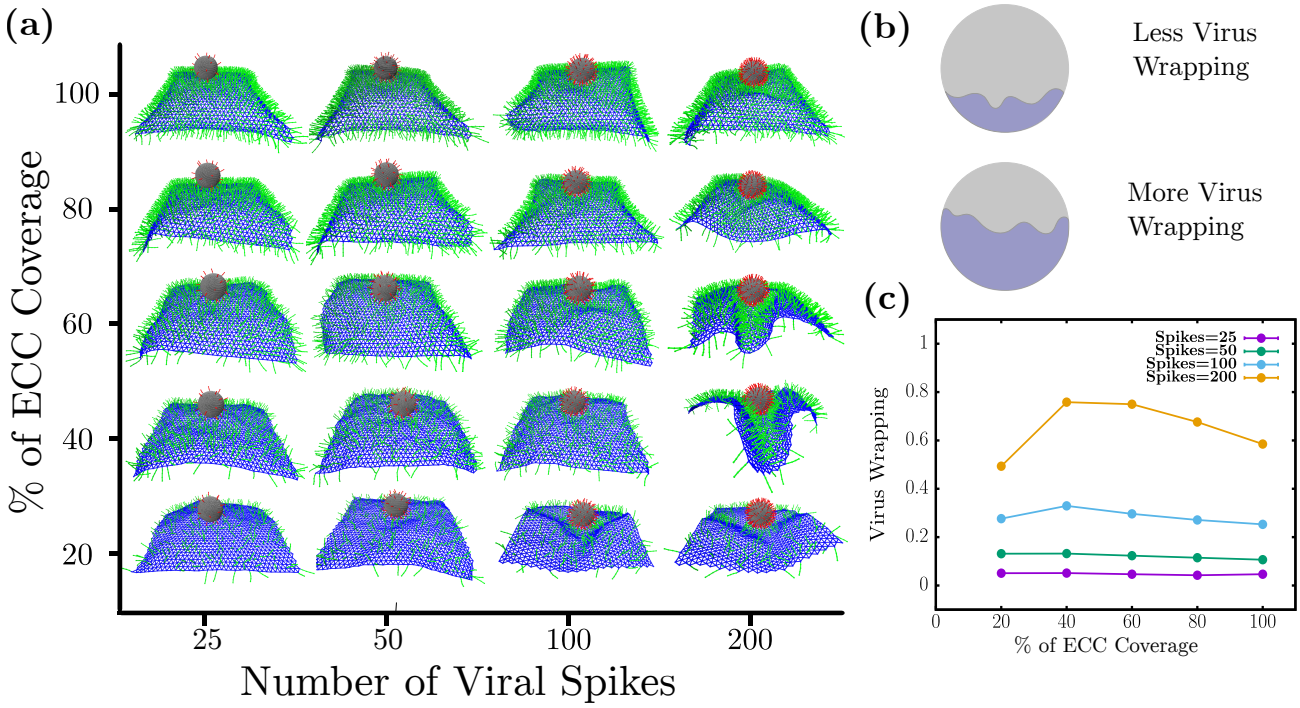

Figure 13 : *Optimal coverage of extra-cellular components (co-receptors) is required for maximal wrapping* (a) Simulation snapshots the virus wrapping as a function of number of virus spikes and ECC coreceptor percent of area coverage. (b) Virus wrapping is defined as the ratio of virus surface area covered by cell surface and the entire virus surface area (c) Virus wrapping as a function of percent of ECC coverage: For lower spike numbers, there is no appreciable wrapping, but for 200 spikes, non-monotonic viral wrapping behaviour emerges. Note that 200 spikes correspond to a spike area density of 6.3 $\times 10^{-3}$ nm^{-2} and 100 % ECC coverage corresponds to the area density of 5.4 $\times 10^{-3}$ nm^{-2}.

we get that $K_{bending}^{CellSurface} = \tilde{K}_{SNN}^{CellSurface} \times 0.7 k_B T$ gives the values shown in Table 1 to give a comparison with measured bending rigidities of the cell membrane that includes the underlying cortical cortex.

The simulation box contains up to 8624 particles. Each particle has a diameter of 10 nm. Since the typical size of the virus is 10s-100s of nanometers and the cell size is usually at the scales of 10 s of micrometers, thus virus interacts only a small part of the cell surface. So, we simulated only a small patch of the cell surface of size 550 nm$\times$480.6 nm, which is made up of 1444 particles. The cell surface boundary is free in our simulations. Each ECC has a length of 40 nm, which is in the range of many cell surface proteins [115]. Since ECC density, or percentage of coverage, is a parameter, total ECC particles vary from 1156 to 5776. The primary receptor has four particles as well. The virus surface has

a typical diameter of 100 nm [116, 117] and is made up of 1000 particles. The virus spikes consist of two particles or 20 nm long, which correspond to many virus types [83, 86]. The total number of spike particles varies from 50 to 400. The virus spikes and ECCs attract each other only if the distance between their top particles is less than 8.7 nm which is the range of interaction found in experiments [118]. We computed ten realizations for each parameter set and averaged them for plotting purposes. Error bars are the standard deviation of the mean.

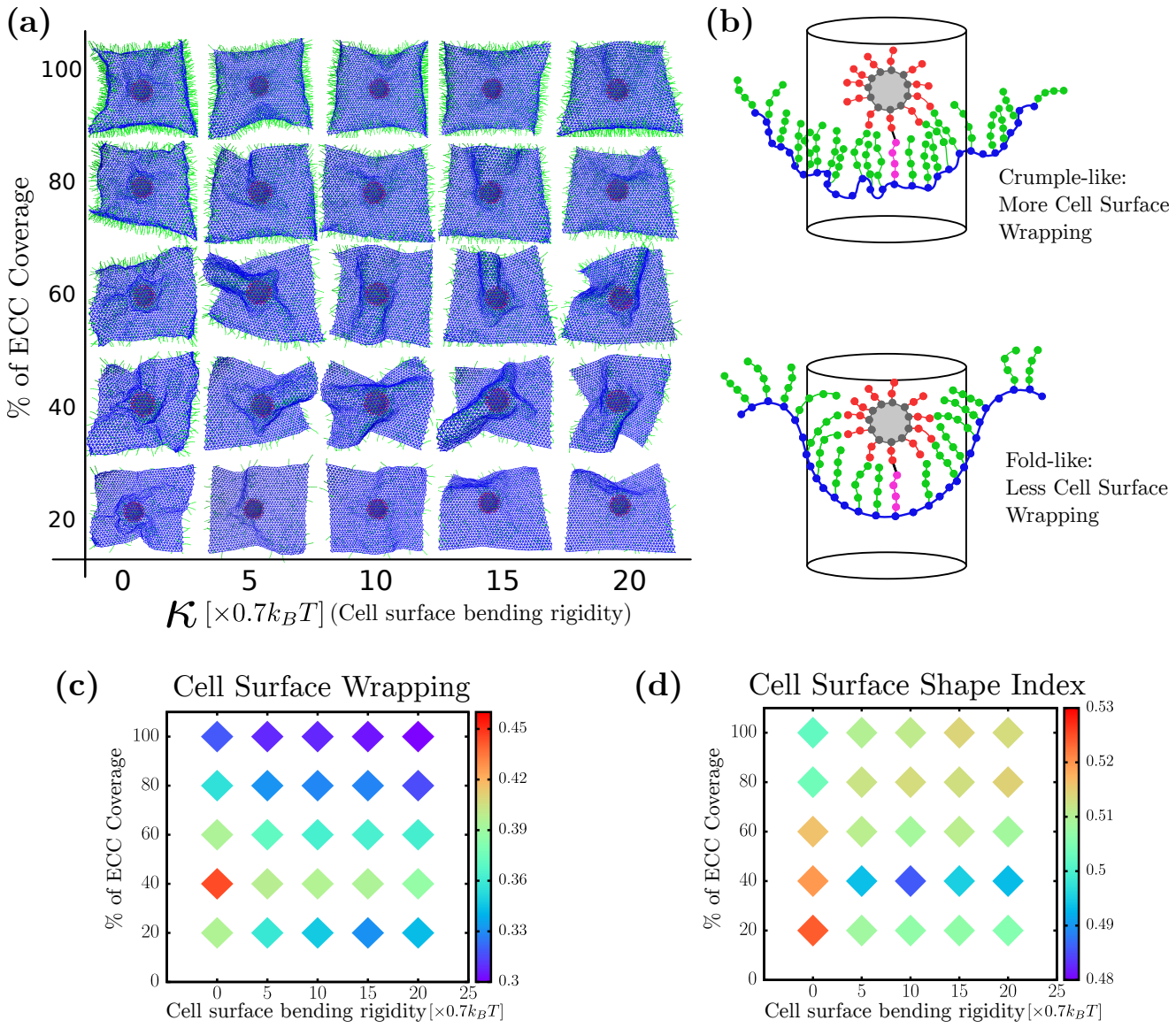

Figure 14 : *Cell surface rigidity helps generate folds* (a) Bottom view of virus wrapping by the cell surface (b) Cell surface wrapping is defined by determining the ratio of the cell surface area inside the cylinder to the total cell surface area. Crumple-like wrapping typically leads to more cell surface area inside the cylinder than fold-like wrapping shape. (c) Cell surface wrapping is minimum for an optimal coreceptor coverage, or area density, which corresponds to folds. Folds use relatively less cell surface area and maximize viral wrapping. (d) Shape index of the cell surface shows folds have a higher value than crumples. Folds form at optimal cell surface coreceptor percent coverage with non-zero cell surface rigidity.

2.2 Results

2.2.1 Optimal co-receptor percentage of coverage yields maximum wrapping

We first investigate the effects of varying extracellular components (ECC) and the virus spike density on wrapping. We altered the cell surface coverage by the ECCs from 20

percent to cover it fully and varied the spike numbers from 25 to 200 spikes. In Fig13 a, we show a typical side view of the final wrapping configurations of the system as the number of virus spikes (horizontal axis) and the percentage of coverage of extracellular components (vertical axis). We observe that the cell surface wraps poorly for lower spike numbers. In other words, there is little interaction between the virus and the cell. However, for 200 spikes, there is substantial wrapping, so we will focus, for the most part, on this part of the parameter space for the number of spikes. Note that 200 spikes uniformly distributed on the surface of the virus-like particle of radius 50 nm leads to an approximate area density of 6.3 $\times 10^{-3}$ nm^{-2}. ECC coverage of 100 % corresponds to the area density of 5.4 $\times 10^{-3}$ nm^{-2}.

To quantify the wrapping behavior, we define virus wrapping as the ratio of the surface area covered via a cell surface divided by the whole surface area of the virus, as shown in Fig 13 b. To find the surface area covered by the cell surface, we compute all virus spikes adhering to ECC and then add their patch area on the virus surface to obtain the area covered. The fractional area of the virus is what is plotted with unity, denoting the entire viral surface is bound to the cell surface. From Fig 13 c, we observe that viral wrapping does not show appreciable changes for viruses with a lower spike number than 200. Given that only one-to-one interaction is allowed between spikes and ECCs, this indicates that only having enough ECC does not necessarily ensure wrapping by the cell surface. However, viruses should also have enough spikes to attach to the cell surface.

We find non-monotonic behavior for the wrapping as a function of the percentage of coverage of extracellular components for 200 spikes, as shown in Fig. 13 c. Specifically, there is less virus wrapping at low ECC percent coverage, $>$ 20 %. Viral wrapping increases at medium percent coverage, 40 and 60 %, only to again decrease for the high ECC percent coverage of 80 and 100 %. Since we have the constraint that a spike can only adhere to one ECC at a time, getting low virus wrapping with low ECC coverage is somewhat expected. As there are few coreceptors to stick to, such viruses cannot interact with many coreceptors. On the other hand, for higher percent coverages of coreceptors, there is a shielding effect that reduces the viral wrapping. Once the coreceptors near the

virus attach to the spikes, far away coreceptors cannot interact with virus spikes due to volume exclusion. Thus, having many coreceptors does *not* lead to higher virus wrapping. Virus wrapping is maximum at the medium coreceptors density, where virus spikes have enough coreceptors to interact with those around them and have enough space between spikes not to invoke shielding effects. Thus, we found an optimal percent coverage of cell surface coreceptors for maximal wrapping. The notion of an optimal percent coverage for maximal wrapping is a rather reasonable one if one considers effective cell surface bending rigidity that depends on such a quantity. More specifically, as the ECC percent coverage increases, the sheet stiffens such that the sheet eventually can no longer wrap around the viral. At lower ECC percent coverage, some stiffening of the sheet gives rise to a more coordinated wrapping, which we explore in more detail in the next subsection.

2.2.2 Cell surface rigidity can drive folds

Next, we investigate the cell surface bending rigidity's role in viral wrapping. Since there exists heterogeneity in the structure and mechanics of the cell cortex, as viruses invade cells, they may encounter different cellular surface rigidities, which may affect the rate of its uptake. In Fig. 14a, we plot the percent coverage of ECCs on the vertical axis and cell surface bending rigidity on the horizontal axis, showing the typical morphology the cell surface takes during viral uptake. These simulation snapshots are taken from the inside of the cell surface with the virus on the outside of the cell. At lower and mid-ECC percent coverage, we observe that the cell surface exhibits crumples, with more cell surface undulations, for zero bending rigidity. However, we observe fold-like structures of the cell surface for non-zero bending rigidity. Furthermore, we do not observe a significant change in cell surface morphology at high ECC percent coverage, irrespective of cell surface bending rigidity, as the ECC percent coverage presumably dominates the effective bending rigidity.

Given that we have two general types of wrapping configurations that the cell surface takes on, crumple-like wrapping and fold-like wrapping, how do we distinguish between the two types? We say "crumple-like" because the crumpling is very localized near the

virus, unlike the crumpling of a sheet of paper, for example [119]. Quantifying folds versus crumples for a triangulated mesh is typically an exercise in discrete geometry. Generically, folds have fewer changes in sign of the local Gaussian curvature than crumples, as the latter consists of shorter, randomly oriented creases. Edge effects combined with noise in the local Gaussian curvature in our system make it difficult to quantitatively distinguish between the two types [120]. So we, instead, measure a dimensionless area of the sheet, much like a gyrification index (GI) as well as a cell surface shape index. As for the former, for a given cylindrical area just beneath the virus, a smoother surface has a smaller area indicating folds, rather than a rougher surface, or larger area, indicating crumples, assuming similar heights. We calculate the cell surface wrapping by taking a circle of radius R, centered at the center of mass of the virus. Starting with the highest spike on the virus that is adhered to an ECC, we construct a cylinder around the virus and identify all the cell surface particles in this cylinder for a given radius. As these particles are a part of a triangulated lattice, we see the total surface area of the cell surface inside the cylinder by adding up all the triangle areas inside the cylinder. Here, the radius of cylinder R sets how close or far from the virus we find the surface area. To arrive at a dimensionless area, we divide the obtained surface area by the total area of the sheet. We cannot have a large value of R compared to the virus radius as there is a finite amount of cell surface; by taking too small R, on the other hand, we may miss some of the data. Therefore, R is 1.5 times of radius of the virus or 150 nm. For other radii, we studied the quantification, and it is robust for a range of R. Please see SI Fig. 17. For calculating the cell surface shape index, we trace the boundary of the cell surface inside the cylinder and determine the perimeter P as well as the cell surface area A inside the cylinder. We then define a dimensionless quantity called shape index as $\sqrt{A}/P$. With this definition of shape index, a hemispherical surface has a shape index of approximately 0.399, which would be a lower bound. Larger shape indices denote less spherically symmetric wrapping and, so, less efficient wrapping in terms of the use of cell surface area.

In Fig 14 b, we have plotted the cell surface wrapping as a heat map, where the color bar represents the ratio of cell surface near the virus divided by the total cell surface area.

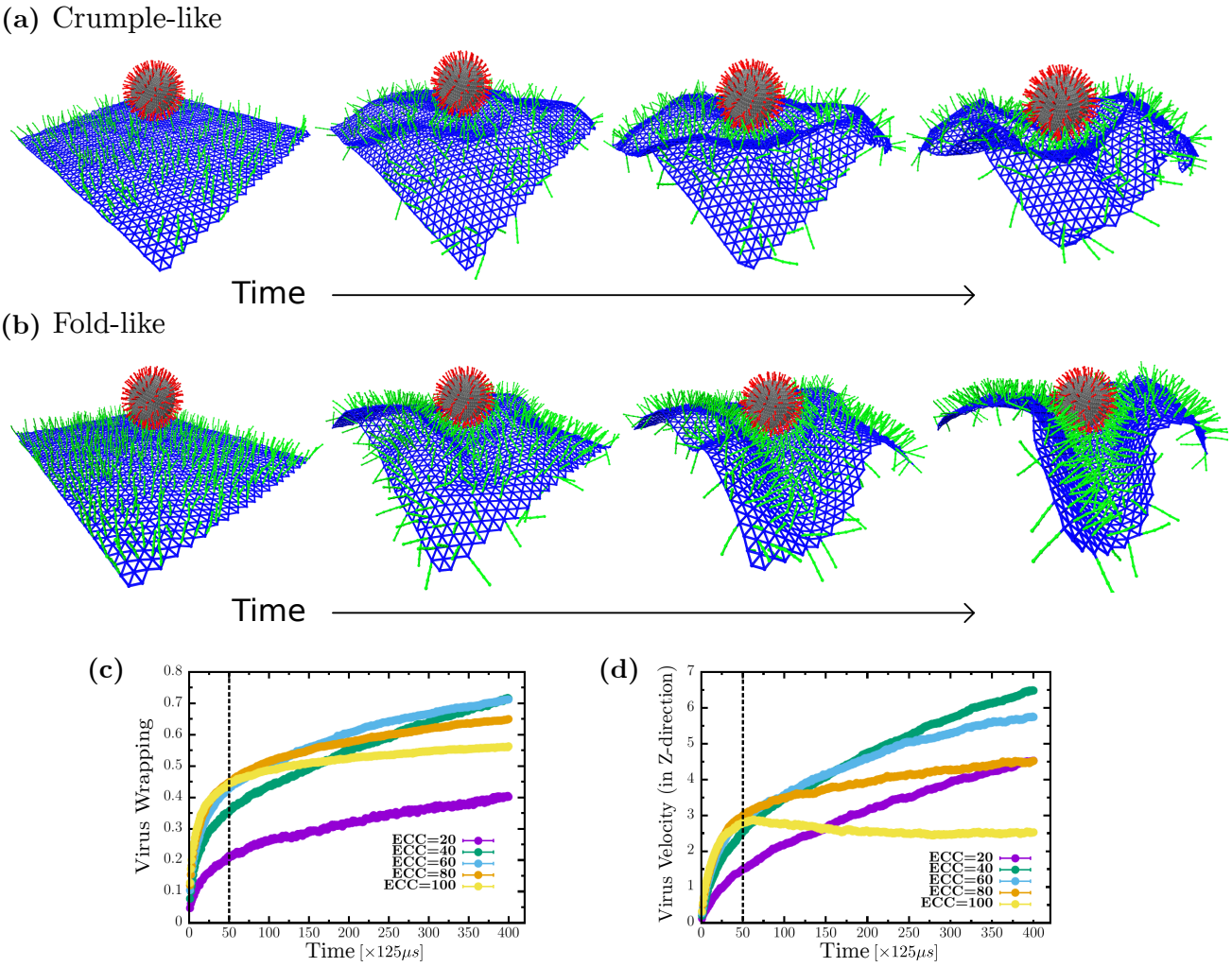

Figure 15 : *Cell surface folds wrap the virus faster than cell surface crumples* (a) Cell surface crumpling around the virus while wrapping at low ECC percent coverage (b) Cell surface creates folds while wrapping the virus at optimal ECC percent coverage. (c) Virus wrapping is fast initially but slows down as fewer ECC are available to attach, eventually has the highest wrapping at optimal ECC percent coverage. (d) Virus velocity in the z-direction shows the highest acceleration with cell surface folds around the virus at optimal ECC percent coverage. The simulation velocity can be converted to a biologically relevant velocity by 200μm/s. Biologically relevant time units can be obtained by multiplying 125μs that follow from the time units defined previously.

At high ECC percent coverage, the cell surface near the virus does not change significantly with cell surface bending rigidity and has less cell surface area near the virus. This is due to effective cell bending rigidity which arises because of volume exclusion among all ECC particles that keep the cell surface shape constant. This effect is more pronounced at high density as more particles lead to higher effective bending rigidity and keeps the surface near-flat. If the cell surface is perfectly flat, the ratio of area under the circle and total surface area is 0.27, which is very near to the value we found for the ratio at

a higher percent coverage of ECC. We also observe that for low and mid-ECC densities at zero-bending rigidity, it takes more cell surface area to wrap viruses compared to the non-zero bending rigidity. From Fig. 14 a, we see crumples forming at low-mid ECC with zero-bending and folds forming with non-zero-bending rigidity. Therefore, crumples take more cell surface area than folds to wrap the virus. This is more pronounced at the optimal ECC percent coverage of 40 percent, where the difference between cell surface area taken crumple and folds are about 10 percent. While a 10 percent difference is not a substantial difference for the uptake of one virus, it may become more substantive for multiple viruses in addition to the usual material that is endocytosed.

Furthermore, we plotted the cell surface shape index as a function of ECC percent coverage and cell surface bending rigidity in Fig. 14 c. Just as with the dimensionless GI, at low or mid-ECC percent coverage and zero bending rigidities, the larger shape index indicates crumples in red. However, for non-zero bending rigidity, the shape index decreases, as indicated in blue, thereby indicating more efficient wrapping. This is more pronounced at the optimal ECC percent coverage of 40 percent. Note that for the higher ECC percent coverage, the shape index decreases from the crumple value; however, the overall curvature of the cell surface begins to change near the virus to head towards anti-wrapping, if you will.

2.2.3 Folds wrap faster than crumples

We now explore the dynamics of viral wrapping. From Fig. 15 a and b, we can see crumple and fold formation, respectively, as the cell surface wraps around the virus. In Fig. 15 a, the cell surface is covered with a lower ECC percent coverage, 20 percent leading to crumpling around the virus, and in Fig. 15 b, the cell surface has the optimal ECC coverage of 40 percent, where the cell surface is folding towards the virus. We analyzed these configurations by plotting the virus wrapping as a function of simulation time for multiple ECC densities.

From Fig. 15 c, at lower ECC percent coverage, the virus is wrapped slowly, but for higher percent coverage of coreceptors, the cell surface wraps fast initially. To be specific,

we observe two regimes of virus wrapping with time, an initial faster wrapping before the dashed line in Fig. 15 c, where spikes are attaching to many coreceptors, and a slower regime at later times, after the dashed line, with the virus attached to a lower number of coreceptors leading to slower viral wrapping. In terms of coreceptor percent coverage, virus spikes do not bind many coreceptors to wrap initially for lower coreceptor density. However, as the cell surface crumples, spikes find more coreceptors to bind, increasing virus wrapping with time but eventually achieving low viral wrapping. For higher percent coverage, spikes initially find many coreceptors to bind, but since there is only one-to-one interaction allowed, spikes located at the higher side of the virus struggle to find more later as the shielding effect sets in due to crowding imposed by volume exclusion. Finally, at optimal percent coverage, we see that even though wrapping starts relatively slowly initially, it catches up as more and more coreceptors come into the range of virus spike interaction due to the folding of the cell surface, leading to the highest virus wrapping such that crowding effects are minimized.

We also investigate the virus's engulfing velocity to further understand the role of folds and crumples in viral uptake. We plotted the virus velocity in the z-direction, or perpendicular with respect to the cell surface, see Fig. 15 d. Here, we also observe two regimes, an initial fast regime before the dashed line, where virus velocity is similar for all densities except the lowest, as in this region viral spikes are attaching to many coreceptors. We also have a second regime later, after the dashed line, where the virus engulfing velocity is distinct depending on coreceptor percent coverage. For lower percent coverage, the virus engulfing velocity is slower because of the low availabilities of coreceptors, but with higher percent coverage, virus velocity slowly increases with time even though coreceptors are available; due to crowding, additional virus spikes cannot attach to the coreceptors. For the optimal coreceptor percent coverage, we see an increasing velocity over time as spikes keep finding more coreceptors to attach. Thus, the cell surface that folds is faster in catching the virus than cell surfaces that crumple around the virus.

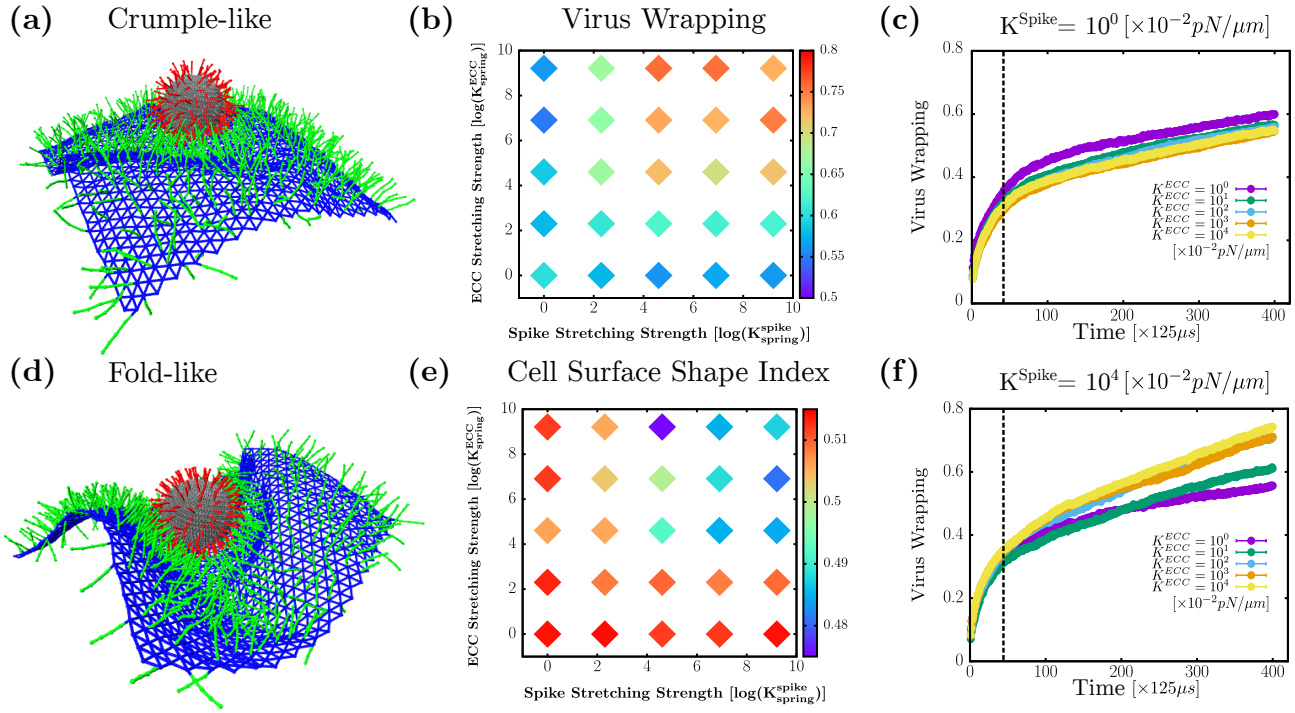

Figure 16 : *Changes in ECC and spike stretching strength can lead to crumples (at optimal ECC density).* (a) Simulation snapshot for $K_{spring}^{spike} = 10^0$ and $K_{spring}^{ECC} = 10^0$ show crumpled cell surface (b) log-log plot: Heat map of virus wrapping showing at low spike and ECC spring strength gives low wrapping compared to high spike and ECC spring strength values (c) and (f) viral wrapping as a function of time for $K_{spring}^{Spike} = 10^0$ and $K_{spring}^{Spike} = 10^4$ for various values of K_{spring}^{ECC} (d) Simulation snapshot for $K_{spring}^{spike} = 10^4$ and $K_{spring}^{ECC} = 10^4$ showing folded cell surface (e) log-log plot: Heat map of cell surface shape index have a higher value at low streching strength of ECC and spikes indicating crumple formation, but at high ECC and spike strength has lower shape index points to fold formation. Biologically relevant time units can be obtained by multiplying 125μs that follow from the time units defined previously. For spring constants, the conversion factor is 10^{-2} pN/nm.

2.2.4 ECC and spike stretching drives the system from folds to crumples

In this subsection, we investigate the effects of the mechanical properties of spike and ECC on viral wrapping. Indeed, filaments on the cell surface have varied mechanical properties depending on the type of filament. Therefore, we vary the stretching strength of coreceptors and virus spikes on viral uptake. Given this additional mechanical variation, we ask the question, is the optimal percent coverage of coreceptors always guaranteed a fold? To answer this question, we maintain the percent coverage of coreceptors at 40%, which yielded maximal virus wrapping, as shown in Fig. 123 c, for 200 spikes (for the given set of mechanical parameters stated previously). From Fig. 16 a and 16 d, we observe that changing the stretching strength drives the cell surface morphology to crumples, even at the optimal percent coverage of coreceptors. In Fig 16 a, coreceptors and spikes

have low stretching strength of $10^{-2}pN/nm$. The attraction between spikes and ECC with low stretching cost energy makes them more accessible to each other, leading to many attachments between them. Even though we have a significant number of spikes connected to coreceptors, the cell surface does not form a fold but a crumple. This is because these low- stretching strength coreceptors cannot transfer enough force to the cell surface to make a more coordinated fold. On the other hand, in Fig. 16 d, the spike and ECC have the stretching strength of $10^{2}pN/nm$, which is enough to generate forces to fold the cell surface around the virus. Thus, we found that an optimal ECC percent coverage determined for one set of mechanical parameters does not ensure efficiency that virus wrapping can always be achieved. The stretching rigidity of spikes and filaments on the cell surface also constrains the formation of folds.

We vary the stretching strength of spike and coreceptors up to four orders of magnitude given in Table 1. In Fig. 16 b, we plot the heat map (on log-log scale) of virus wrapping with respect to the ECC and spike stretching strength. We observe two regions, first a low wrapping region at low spike stretching strength which persists irrespective of coreceptors stretching strength. For low coreceptors stretching strength also, we find low wrapping, irrespective of spike stretching strength, as depicted in blue on the heat map. The second region has high virus wrapping for the high spike and coreceptors stretching strength, as shown in red. Our findings imply that the coreceptor and spike must have high stretching strength to get a high virus wrapping. To identify the folds and crumples qualitatively, we plotted the cell surface shape index in Fig. 16 e. We find that for low spike and ECC stretching strength, we measure a higher shape index which is consistent with cell surface crumpling around the virus. At higher spike and ECC stretching strength, we measure a lower value of the cell surface shape index, indicating fold formation. These results are consistent with the previously observed shape index behavior in Fig 15 c.

We also examine the time series analysis to understand how the fold and crumple formation mechanism changes due to the stretching strength of spike and coreceptors. In Fig 16c, we set the stretching strength of spikes constant at the lowest explored value of 10^{-2}pN/nm and vary the coreceptors stretching strength from 10^{-2}pN/nm to 10^{2} pN/nm.

We observe that changing coreceptors stretching strength does not contribute much to the virus wrapping behavior as it just increases with time having similar trends for all coreceptor's stretching strength values. On the other hand, from Fig. 16 f with a high spike stretching strength of 10^2pN/nm, we see that low coreceptor stretching values are associated with wrapping slowly and get less virus wrapping than for high coreceptor stretching strength. This is because, with the higher stretching strength of the spike and coreceptor, the cell surface folds, leading to the faster wrapping of the virus.

We demonstrate that having optimal coreceptors percent coverage is not enough for efficient wrapping via folds. Coreceptors and spikes also require a threshold stretching strength above which the cell surface folds to achieve more wrapping. We also investigate the effects of the bending rigidity of filamentous ECCs and virus spikes. Bending rigidity does not impact the cell surface morphologies as stretching. See Fig. 18 in SI. Finally, as for varying viral rigidity, we obtain results consistent with previous work [90] that softer viruses are harder to wrap than more rigid viruses. See Fig. 19 in SI.

Discussion

Our study suggests that cells whose surfaces are optimally populated with filamentous protein structures acting as coreceptors are more likely to be infected as they uptake the virus faster and use relatively less cell surface area per individual virus so that more virus-like particles can be uptaken. At the optimal percent coverage, the cell surface makes folds around the virus, and folds are faster and more efficient at wrapping the virus than crumple-like wrapping. Our study also finds that cell surface bending rigidity helps generate folds, as bending rigidity enhances force transmission across the surface. We also conclude that such an optimal percent coverage does not always ensure a fold formation, as changing mechanical parameters, such as the stretching stiffness of the ECC or the virus spikes, can drive the crumple-like formation of the cell surface.

There has been much work exploring the role of viruses or nanoparticle spikes and how their mechanical properties affect endocytosis. However, these studies treat receptors as sticky particles on the cell surface without any degree of freedom [82, 121, 122, 90, 123,

124, 125]. On the other hand, there have also been many studies of sticky sites embedded in a cell membrane affect endocytosis, though, again, they do not have their own degrees of freedom [126, 127]. To our knowledge, this work is the first to consider the physical properties of receptors, including density, stretching, and bending energetic costs on both the cell and viral surface in viral wrapping. In doing so, we find a key quantity to focus on in terms of an effective stiffness of the cell surface that depends on the density of filaments attached and their own intrinsic mechanics. Work will be needed to quantify this property in larger sheets without the virus-like particles. Moreover, it is interesting to determine how material on the outside of a cell, both the virus and the extracellular filaments, can reshape the cell cortex in nontrivial ways in terms of folds versus crumples, which then drives shape changes in the connected plasma cell membrane. Interestingly, earlier work on endocytosis has focused on how the underlying cell cortex can modify the shape of the plasma cell membrane from spherical wrapping to more cylindrical wrapping in yeast [128]. In this work, we unlock a much broader range of shapes for further study.

The earlier experimental finding that extracellular vimentin enhances SARS-CoV-2 uptake is intriguing [29, 30]. It turns out that extracellular vimentin helps other viruses and bacteria to enter the cell [35]. As there exist vimentin-null mice (but not actin-null nor microtubule-mull mice) [129], the fact that viruses and bacteria have evolved to interact with vimentin is no surprise when hijacking the machinery of a cell. In doing so, they interact with a higher-order, optimizing construct instead of an essential, functioning construct to replicate and redeploy without dramatically altering cell function. Presumably, this is yet another evolutionary pressure on viruses to optimize their interaction with vimentin on both the outside and inside of cells. Therefore, our focus on constructs outside and/or attached to the cell emphasizes the importance of the microenvironment of a cell, even for endocytosis. The importance of the tumor microenvironment has now become a cornerstone for understanding cancer, with many modeling efforts underway to make predictions [130, 131, 132, 133]. Given the work here, we now argue that the notion of microenvironment has an impact on viral and bacterial infections and will contribute towards our understanding of the variability of health impacts of such infections. While

our inspiration here has been extracellular vimentin, glycolipids that bind the protein lectin to form a filamentous-like complex emanating from the cell surface and can play a role in clathrin-independent endocytosis [134]. Our results point to a potential mechanical role for this complex in endocytosis.

We have assumed that the virus-like particle is already attached via a small receptor to the cell surface and quantified viral wrapping. However, it would also be interesting to study how the cellular microenvironment affects the trajectory of a nanoparticle to find that initial receptor in terms of search strategy [135]. We have also assumed a one-to-one interaction between ECC and spike without any kinetics, i.e., no attaching or detaching rate is considered in this model. Finally, as our cell surface is a deformable sheet to which filamentous structures attach, we will investigate how the nanoparticle enters the cell via a pinch-off mechanism by extending our work to include a cellular fluid membrane. In the earlier work quantifying cylindrical endocytosis in yeast, the proposed pinch-off mechanism is a Pearling instability driven by BAR proteins acting on both the cortex and the plasma cell membrane [128]. As additional morphologies of the cell surface are proposed in mammalian cells [136, 137, 138], perhaps a Pearling instability or additional mechanisms will be discovered. To make such predictions, the richness of biology must be reflected in analytical or computational modeling in at least some minimal manner.

2.3 Supplementary Figures

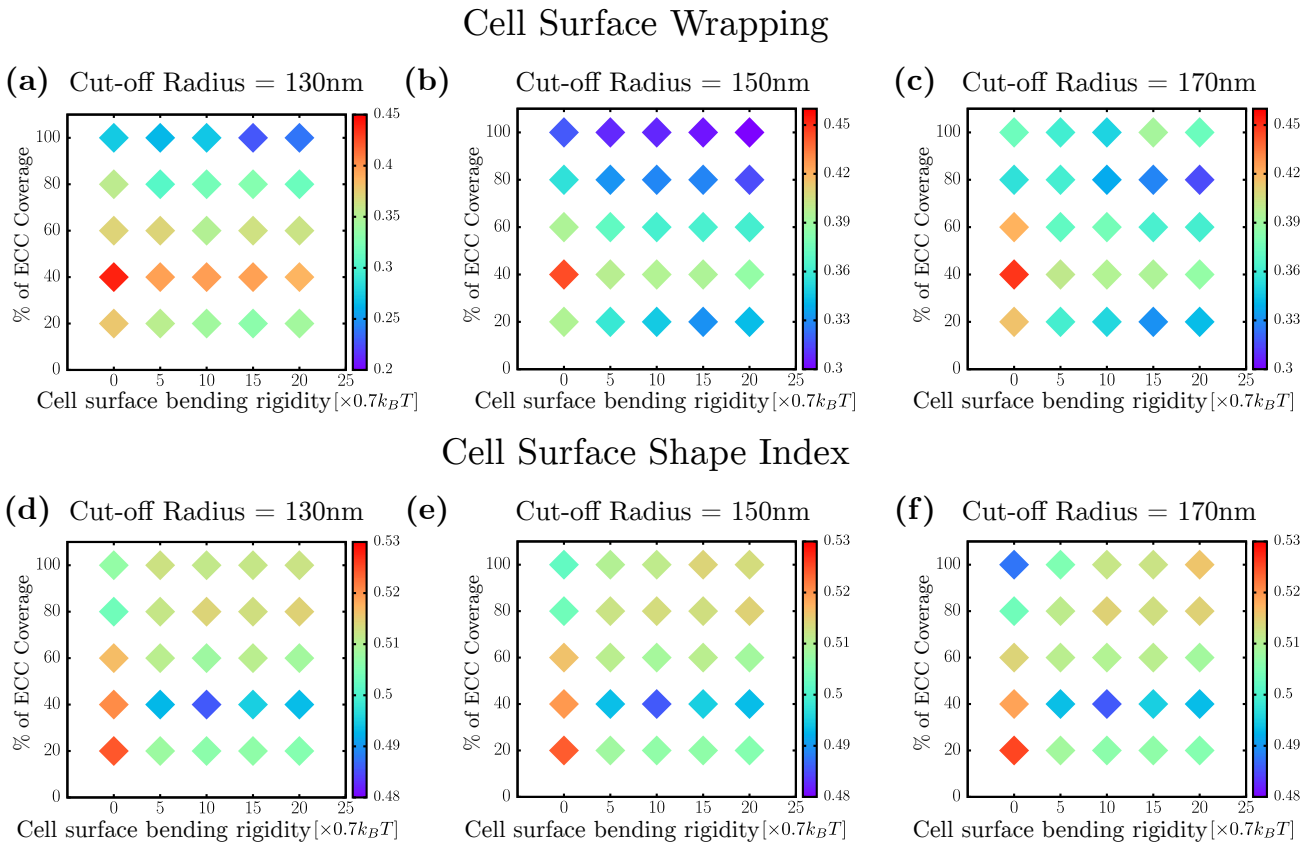

Figure 17 : Cell surface wrapping and shape index is robust with the varying cylinder's radius cut-off

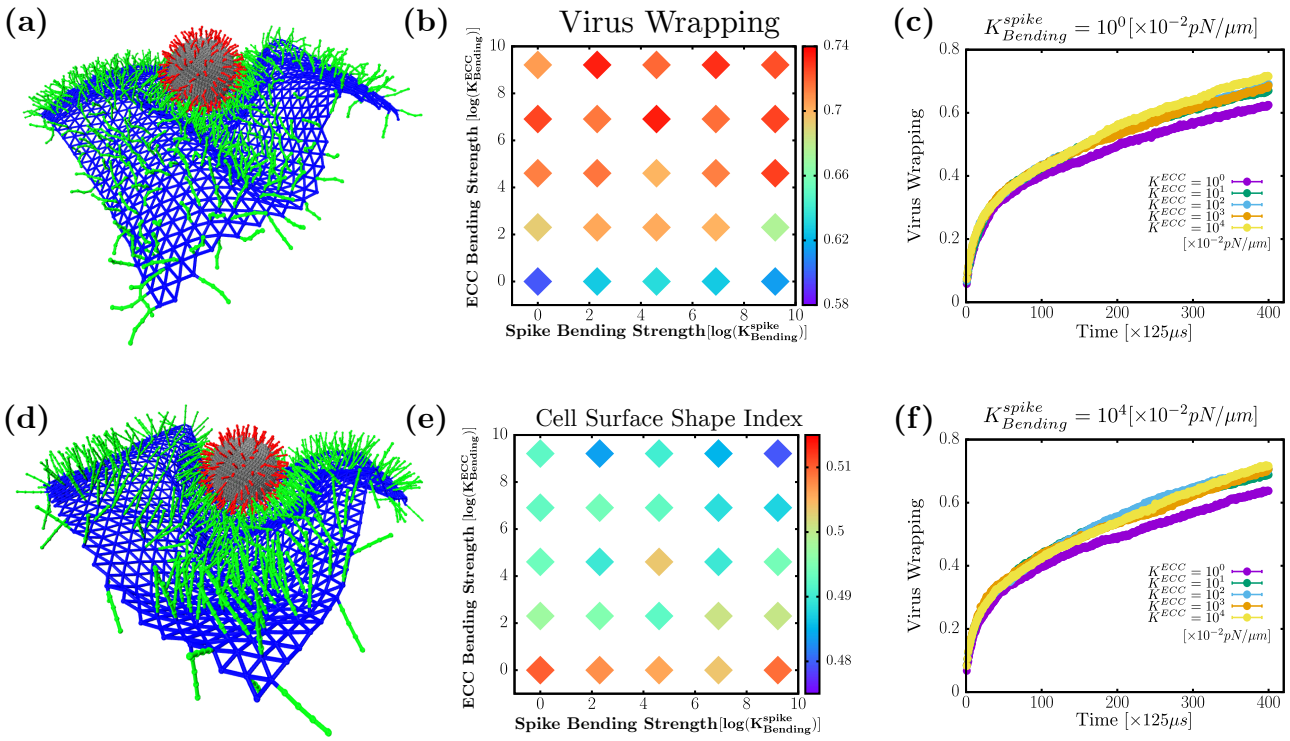

Figure 18 : *Varying ECC and spike bending rigidities does not lead to cell surface crumples* (a) Simulation snapshot for $K^{spike}_{Bending} = 10^0$ and $K^{ECC}_{Bending} = 10^0$ show folded state (b) log-log plot: Heat map of virus wrapping showing at low ECC bending strength irrespctive of spike bending strength gives low wrapping compared to high ECC bending strength (c) and (f) Virus wrapping as a function of time for $K^{spike}_{Bending} = 10^0$ and $K^{spike}_{Bending} = 10^4$ for various values of $K^{ECC}_{Bending}$ (d) Simulation snapshot for $K^{spike}_{Bending} = 10^4$ and $K^{ECC}_{Bending} = 10^4$ showing sharply folded cell surface (e) log-log plot: Heat map of cell surface shape index have a higher value at low bending strength of spike indicating soft folds formation, but at high ECC bending strength has lower shape index points to sharp fold formation. Biologically relevant time units can be obtained by multiplying 125μs that follow from the time units defined previously.

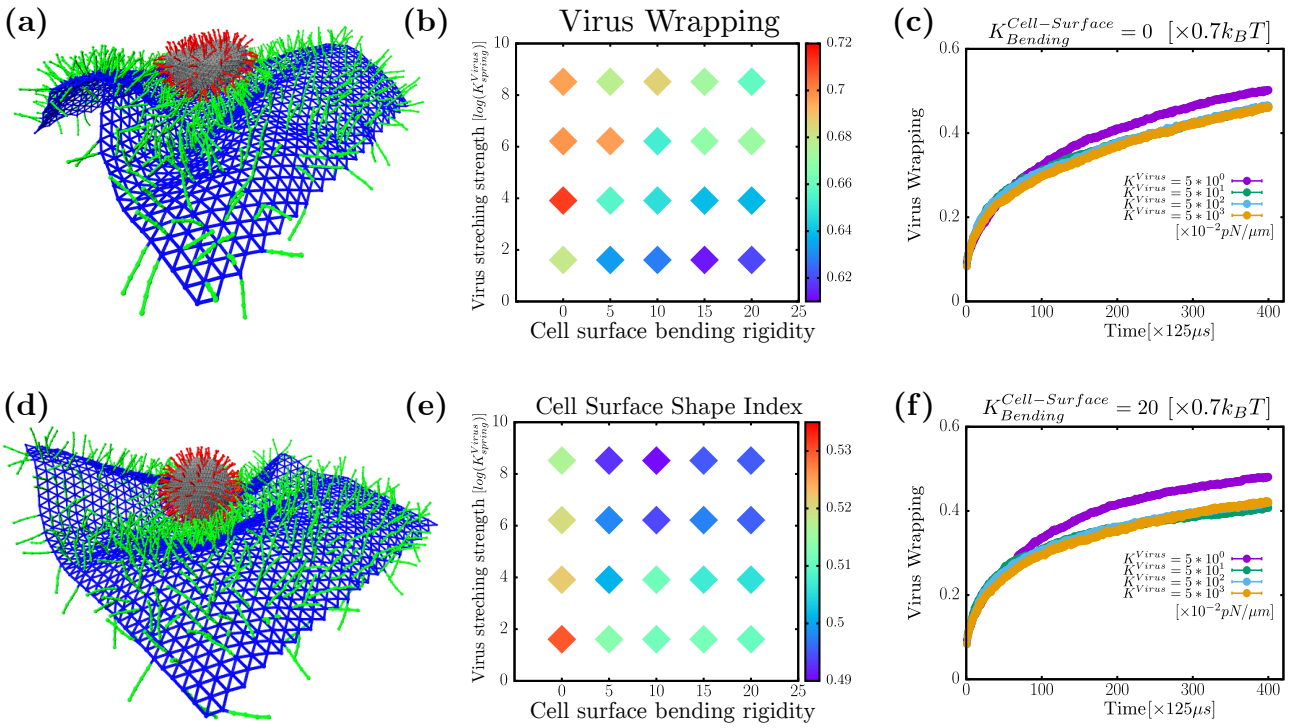

Figure 19 : *Varying virus stretching rigidity* (a) Simulation snapshot for $K^{Virus}_{Spring} = 5*10^0$ (b) log-log plot: Heat map of virus wrapping as a function of virus stretching strength and cell surface bending rigidity. Since the virus is deformable, virus wrapping here is defined as the ratio of occupied spikes divided by the total number of virus spikes. (c) and (f) Virus wrapping as a function of time for $K^{Cell-Surface}_{Bending} = 0$ and $K^{Cell-Surface}_{Bending} = 20$ for various values of K^{Virus}_{Spring} (d) Simulation snapshot for $K^{Virus}_{Spring} = 5*10^4$ (e) log-log plot: Heat map of cell surface shape index as a function of virus stretching strength and cell surface bending rigidity. Biologically relevant time units can be obtained by multiplying 125μs that follow from the time units defined previously.

Chapter 3

Active Chromatin Dynamics Drives Nuclear Bulge Formation

Abnormal nuclear shapes can serve as biomarkers for various human pathologies, including conditions like rapid aging (Progeria), metastatic cancers, and muscle atrophies, as shown in Fig 20 [41, 42, 43, 44, 45, 46]. The structure of cell nuclei consists of lamin proteins and chromatin, which is condensed DNA, among other biological materials. Externally, the nucleus is connected to cytoskeletal elements such as actin, microtubules, and intermediate filaments, like vimentin [139, 42, 140]. These cytoskeletal elements can transmit forces from outside the cell to the nucleus and also from inside the cell due to the action of motors like myosin on actin, Kinesin, and dynein on microtubules, as well as through the repolymerization of cytoskeletal filaments [139, 42]. These forces are being transmitted to various lamin-associated filaments on the nucleus, including Nesprin and SUN family proteins [141, 142, 143].

Recent experimental studies have focused on understanding the forces generated at the chromatin scale due to transcription factors like condensin, cohesin, and RNA Pol II families [58, 144, 145]. These factors not only reorganize chromatin within the nuclear lamina but also exert forces on it via other parts of chromatin [146, 147]. While previous studies have mainly examined nuclear shape aberrations from the outside or lamin surface perspective [46, 57], assuming the nucleus's interior to be a passive material, the role of chromatin activity in shaping the nucleus remains poorly understood.

To address the role of chromatin activity in generating diverse nuclear shapes, we have developed a computational model. The model focuses on the physical properties of chromatin, such as its interconnections and links to the nuclear lamin shell, as well as the active details, including the number of motors and their lifetimes. We quantitatively demonstrate the significance of the nucleus's internal dynamics by considering how the nuclear shape forms due to internal activity and chromatin chain topology. In comparison with experimental data, we provide new insights into the role of chromatin-correlated motion in shaping the nucleus, offering a more comprehensive understanding of abnormal nuclear shape, including bulges and wrinkle formation.

Recent experimental studies [148] has also focused on investigating the behavior of the nucleus under compression to understand the impact of forces from cytoskeletal elements

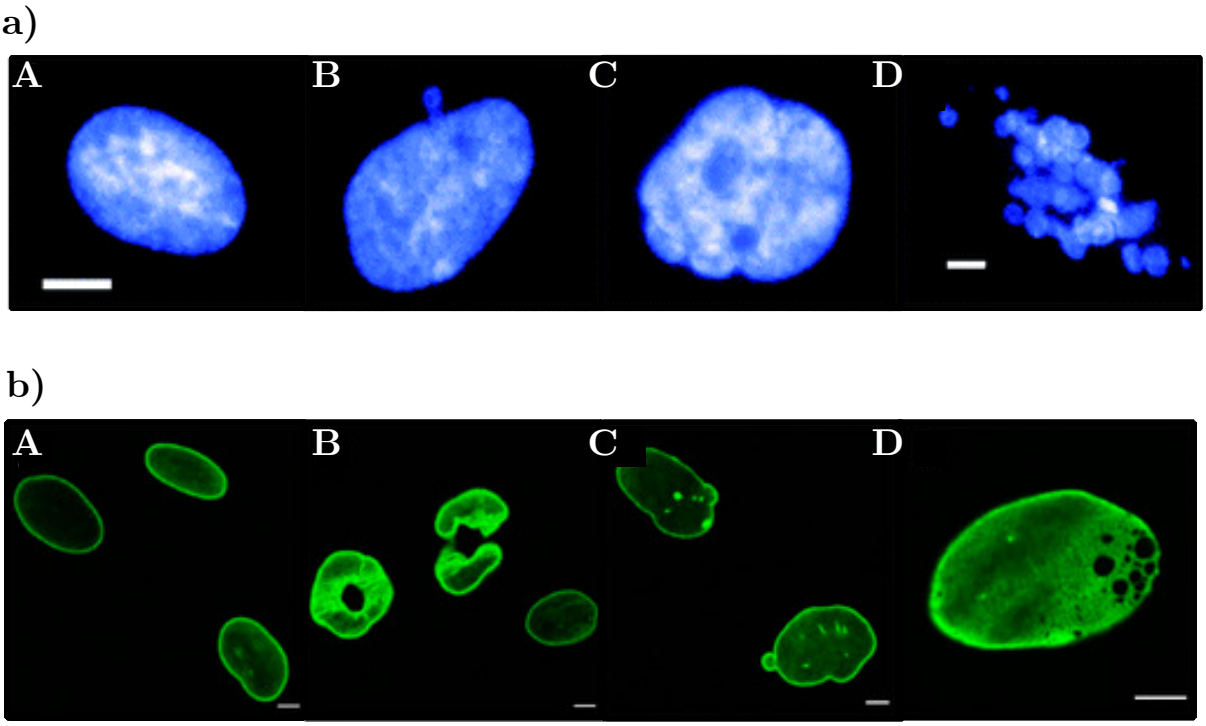

Figure 20 : *Abnormal nuclear shapes in human diseases cells* (a) Immunostained images of (A) a control nucleus and HGPS fibroblasts with (B) herniations in the nuclear periphery or nuclear blebbing or bulge formations, (C) folds and crevices, (F) fragmentation of the nucleus [54]. Scale bars = 10 μ m. (b) Nuclear abnormalities are commonly observed in human dermal fibroblasts obtained from patients with laminopathies. Green: lamin A/C staining using Jol2, (A) normal nuclei, (B) donut-like shaped nuclei, (C) nuclear blebbing, (D) honeycomb structures. Bars represent 5 µm. [55]

outside the nucleus [149, 150], as well as the nucleus itself as a material. These studies have revealed that the nucleus exhibits compression stiffening behavior at low strains [148]. While it is known that external forces act on the nucleus, the specific mechanism underlying compression stiffening remains unclear.

To gain insights into possible mechanisms, we performed simulations on our nucleus model with different strain rates. By comparing the results from different strain rates, we aimed to explore how forces are transmitted throughout the nucleus via the lamin network and chromatin chain. Additionally, our simulations shed light on the viscoelastic behavior of the nucleus under compression, providing insights into the mechanical response of the nucleus under compression.

We have organized this chapter as follows. First, we present our computational model and the dynamics method with each component's details. We begin by explaining the

construction of the lamin shell, which involves creating a sphere composed of finite-size particles with a specific coordination number. Next, we detail the modeling of a random chromatin chain and the process of confining it within the spherical confinement with a desired size. Next, we describe how we assemble the nucleus by placing the confined chromatin chain inside the lamin shell and constructing linkages and crosslinkers. Moving on, we delve into the mechanisms of motors acting on chromatin particles and how they influence the movements of the chromatin chain.

Second, we present the results obtained from our simulations and the analysis method used to quantify the number and stability of bulges as a function of motor numbers, crosslinkers, and motor lifetime. Furthermore, we investigate the behavior of the nucleus under compression with different strain rates.

Finally, we discuss the possible implications of chromatin-correlated motion on the formation of abnormal nucleus shapes and examine the viscoelastic behavior of the nucleus under compression, drawing insights from our findings.

3.1 Simulation model and dynamics

We developed a computational model to understand the role of motors on chromatin in abnormal nuclear shapes. Here we will explain each component of the model and how they interact. We will also discuss the parameters chosen for the simulation and the method to introduce dynamics in the model.

We use the simulation model in three dimensions, which can be challenging to visualize directly, as shown in Fig 21 b. To facilitate understanding, we have created a two-dimensional schematic in Fig 21 a, representing a model cross-section, which builds upon the previous models [151, 152]. In this schematic, we have depicted the main components of the model. The model consists of a nucleus shell, depicted in purple color, enclosing a long chromatin chain shown in blue color. The chromatin chain is connected to other chromatin particles through crosslinkers, represented in red, and it is linked to the shell via linkages, shown in green. The inner dynamics are influenced by motors, which are depicted in yellow. The solid and striped representations of motors indicate extensile and

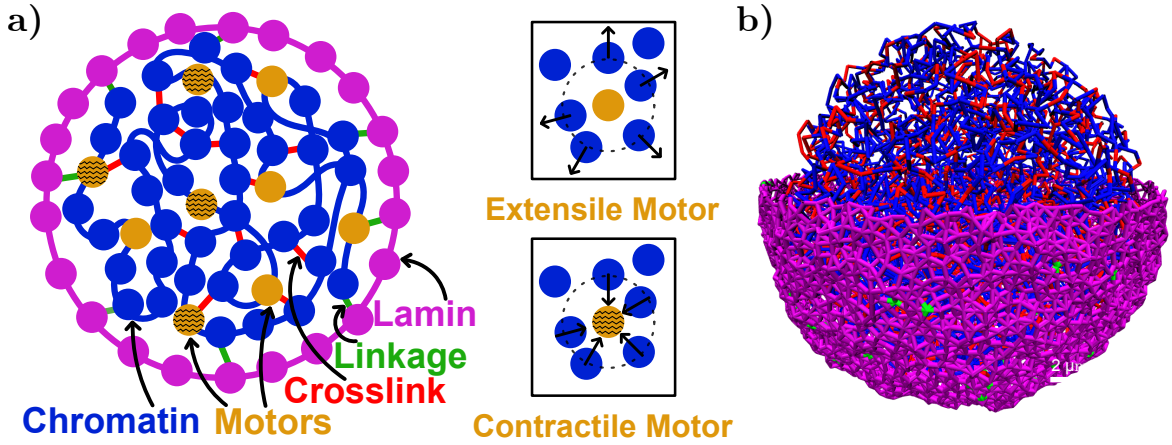

Figure 21 : *Schematic illustration of the components isolated nucleus model* (a) 2D cross-section of the model with nuclear lamin shell in purple, chromatin chain in blue, crosslinkers connecting chromatin chain to itself in red, and linkages in green linking the chain and the shell. The motors are shown in yellow, with solid yellow representing extensile motors and striped yellow indicating contractile motors. Extensile (Contractile) motors repel (attract) all other chromatin particles in the 1.5σ range, where σ is the diameter of the particle. (b) 3D computational model of the isolated nucleus. The nuclear lamin shell is shown in purple, with the green color indicating the position of linkages. The Chromatin chain is shown in blue, and the crosslinkers are red in color. We have removed the top half of the shell so that the chromatin structure can be observed clearly.

contractile types, respectively. In the following sections, we will elaborate on how each element of the model was constructed and implemented in our simulations.

Nuclear lamin shell: To model the nuclear lamin shell, we create a hollow sphere composed of particles connected by harmonic spring potential, given by the equation $V_{Spring}^{Shell} = \frac{K_{Spring}^{Shell}}{2}\left(r_{ij} - l_o^{Shell}\right)^2$, where K_{Spring}^{Shell} represents the strength of the spring interaction, r_{ij} is the distance between two neighboring particles, and l_o^{Shell} is the rest length between these particles.

We generate the initial shell in three steps. Firstly, we generate the desired number of particles on the shell surface following a Fibonacci sequence arrangement, as shown in Fig. 22 a. However, recent experimental studies show that the structure of a lamin nuclear shell is not on a lattice. Thus, we then melt this lattice structure. We did that by subjecting these point-size particles to thermal noise, allowed to move only on the sphere's surface. Also, making these particles grow slowly to a desired diameter,σ, with no overlap allowed due to the soft-core repulsion potential detailed below.

This process gives us a distribution of finite-size particles randomly scattered on the

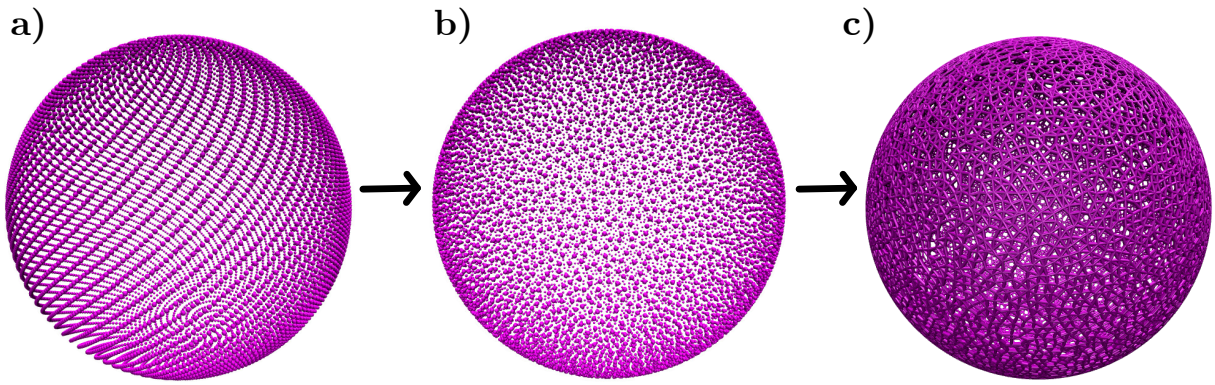

Figure 22 : *Process of generating the nuclear lamin shell :* (a) Initially, we generated N particles on a sphere using a Fibonacci sequence, shown in purple. However, real-world lamin structures do not resemble lattice-like structures. (b) To mimic the random distribution of lamin particles on a sphere, we melted the lattice through dynamics and thermal noise, resulting in a random arrangement of finite-size particles on the sphere. (c) previous research shows that the lamin structure's topology has a coordination number between 4 and 5. To achieve this, we developed an algorithm (explained in detail in the text) to connect the particles, resulting in the final structure shown in the figure.

sphere, as shown in Fig. 22 b. To define the shell's topology, from a previous study [153], we found that it forms a network with a coordination number between 4 and 5. The coordination number indicates the average of how many particles are connected to one chosen particle.

To achieve this desired coordination number, we develop an algorithm. We randomly select a particle and check if any other particle lies within a spherical region around it. If we find a neighboring particle, we count it as a neighbor; if not, we slightly increase the size of the spherical region and continue checking until we find a neighboring particle. We ensure that each chosen particle has at least four and, at most, eight connected particles to achieve the desired average coordination number between 4 and 5. Finally, we establish the lamin configuration with particles and edges connecting them, resulting in the desired lamin structure, as shown in Fig. 22 c.

Chromatin Chain: We generated a chromatin chain as a Rouse chain, where each particle has a diameter of σ. The particles are connected by harmonic spring potential given by $V_{Spring}^{Chromatin} = \frac{K_{Spring}^{Chromatin}}{2}\left(r_{ij} - l_o^{Chromatin}\right)^2$, with $K_{Spring}^{Chromatin}$ representing the chromatin spring strength, rij denoting the distance between two neighboring particles, and $l_o^{Chromatin}$ is the initial distance between two consecutive particles.

To generate this chain in three dimensions with N particles, we began with a random

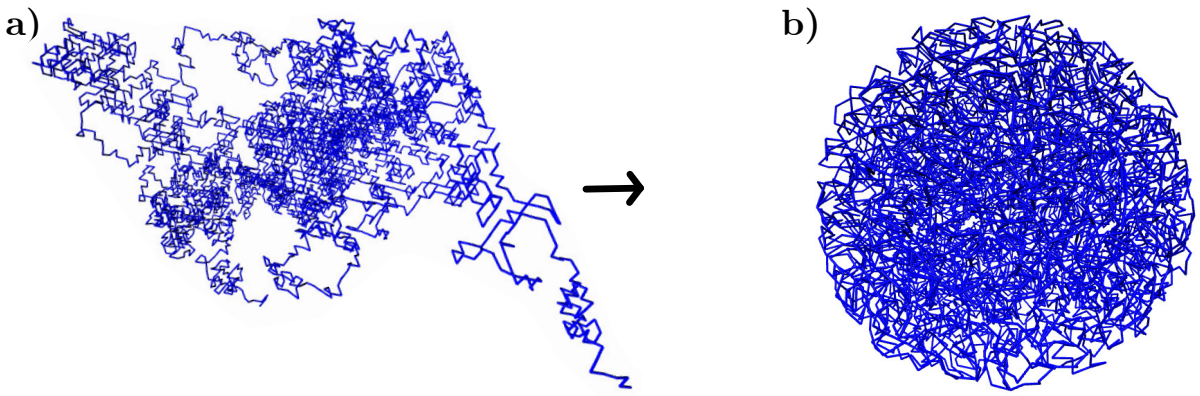

Figure 23 : *Algorithm to generate the chromatin chain and confine it within a shell:* (a) To create a random chain in 3D, we performed a random walk on a face-centered lattice with conditions that no back step is allowed and visited a point on lattice only once. This resulted in a chain without any interconnection, as shown in blue. (b) Subsequently, we confined this chain in a sphere with the method detailed in the text, resulting in a chain confined in spherical confinement representing chromatin.

walk on the face-centered lattice, with no overlap or backward steps are allowed as shown in Fig 23 a. This process results in consecutive points forming the chain in 3D.

Since chromatin exists within the nuclear lamin shell, we needed to confine this chain within a spherical boundary of the desired size. To achieve this, we followed these steps: First, we found the center of mass of the chain and identified the chain particle farthest from this center, which gave us the initial radius. The final radius was set as the radius of the shell. With the application of boundary conditions and thermal noise, we gradually shrank the sphere from the initial radius to the final radius, causing the chain to confine within it. The boundary condition decreases the initial boundary radius slowly. If any particle was found outside this boundary, we applied a spring potential to it, with one end tethered to the boundary and the other end attached to the particle with a resting length of zero. This effectively pulled the particle inside the shrinking sphere. We stopped this process once the desired sphere radius was attained, resulting in the chain being confined within the sphere shown in Fig 23 b.

Chromatin chain inside the lamin shell: Next, to generate the isolated nucleus model, we kept the spherically confined chain shown in Fig 24b inside the lamin shell shown in Fig 24a. For this, we found the center of mass of both chain and the shell and kept it at the same coordinates. We let the system run under the dynamics with thermal noise to equilibrate the configuration. We found that the chain and deformable shell expand

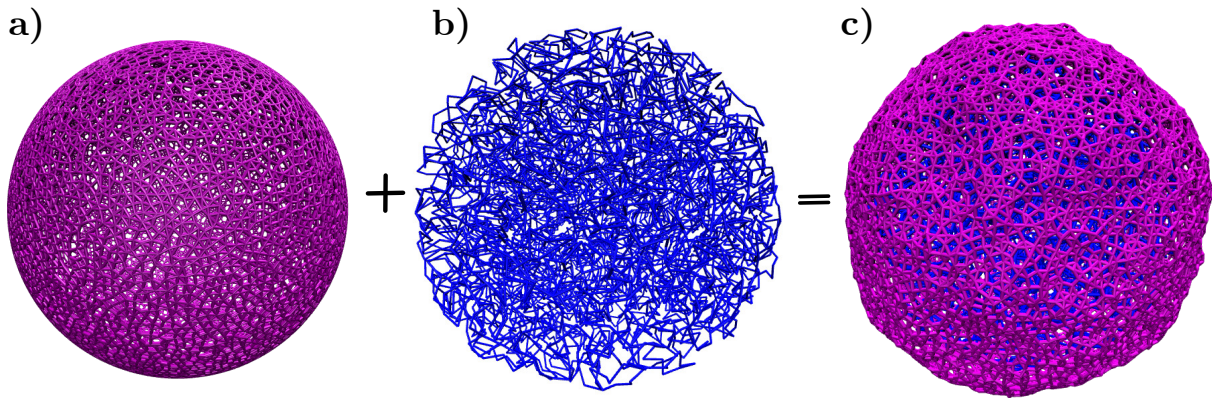

Figure 24 : *Placing chromatin chain inside the nuclear lamin shell:* (a) Nuclear lamin shell generated via particles on a sphere with average coordination number 4.5 (b) Chromatin chain generated through a random walk of face-centered cubic (FCC) lattice and then confined within a sphere. (c) To achieve the confined chromatin chain inside the shell, we align the center of mass of both the shell and chain at the same coordinates. The shell and chain expand during the equilibration process to accommodate the soft-core repulsion interaction.

slightly due to soft-core potential. Finally, we get the chromatin chain inside the shell, as shown in Fig 24c.

Crosslinkers and linkages: Crosslinkers are connections that link non-consecutive particles of the chromatin chain through a harmonic spring potential given by $V_{Spring}^{Crosslink} = \frac{K_{Spring}^{Crosslink}}{2}\left(r_{ij} - l^{Crosslink}o\right)^2$, where $KSpring^{Crosslink}$ represents the strength of the crosslinker spring, r_{ij} denotes the distance between two particles connected by the crosslinker, and $l_o^{Crosslink}$ is the rest length of the crosslinker spring. These crosslinkers represent proteins that connect the chromatin to itself, including HP1-α [50, 51]. To create a crosslink, we choose a random particle on the chromatin chain and draw a sphere of a some small radius around it to locate another non-consecutive particle. These two particles are then connected via a crosslink. We repeat this process until the desired number of crosslinkers is achieved.

On the other hand, linkages connect the chromatin chain to the lamina shell via proteins such as LAP1, LAP2, emerin, and Man1 [52, 53]. These linkages are implemented using a harmonic spring potential expressed by $V_{Spring}^{Linkage} = \frac{K_{Spring}^{Linkage}}{2}\left(r_{ij} - l_o^{Linkage}\right)^2$, with $K_{Spring}^{chromatin}$ representing the strength of the linkage spring, r_{ij} denoting the distance between two particles connected by a linkage, and $l_o^{Linkage}$ being the rest length of the linkage spring. We employ a similar strategy of crosslinks to find the particles for linkages. We

choose a random particle on the shell and find a nearby particle from the chromatin chain to establish a connection. We continue this process until the desired number of linkages is attained. It is important to note that the crosslinkers and linkages are fixed; once we identify the pair of particles, they do not change during the simulation, as no rupture is allowed.

Motors: In our model, we treated a few chromatin particles as motors to represent transcriptional factors like RNA polymerase family, condensin, and cohesin [58, 154, 155]. These motors were classified into two types: extensile and contractile. If a particle acted as a motor, it either attracted (contractile motor) or repelled (extensile motor) other nearby chromatin particles within a specific range, i.e., 1.5σ. The force exerted by the motor on the particles is expressed as $F_{Motor} = M \cdot F_a \hat{r_{ij}}$, where F_a represents the force experienced by the particles due to the motor, and $\hat{r_{ij}}$ is the unit vector pointing from the center of the motor particle to the influenced chromatin particle. The sign of the force depends on the motor type, with M taking either a positive $(+)$ value for contractile motors or a negative $(-)$ value for extensile motors. It is important to note that these motors cannot act with any force on the lamin shell except due to the soft-core repulsion.

Furthermore, these motors are not stationary on the chromatin chain, as they also keep moving in the real nucleus. Instead, we modeled their dynamic behavior by having motors switch off at one particle and switch on at another particle following a Poisson process with a characteristic time τ. The physical interpretation of τ is the average lifetime of a motor at a chromatin particle.

Soft-core Repulsion: Each component is subject to volume exclusion, which is achieved through soft-core repulsion. This repulsion force is given by Eq. 3.1, where $K_{Soft-Repulsion}$ represents the strength of the soft repulsion, r_{ij} is the distance between the centers of two particles, and σ is the diameter of a particle. The soft-core repulsion force comes into effect only when the distance between particles is less than the diameter of a particle.

$$V_{Soft-Repulsion} = \begin{cases} \frac{K_{Soft-Repulsion}}{2} \left(r_{ij} - \sigma\right)^2 & r_{ij} \leqslant \sigma \\ 0 & r_{ij} > \sigma. \end{cases} \tag{3.1}$$

Dynamics: We used Brownian dynamics to simulate the system, governed by the equation 3.2 given below, where r_i represents the position of the ith particle, μ is the mobility constant, and D is the translational diffusion constant. $\xi(t)$ is the Gaussian white noise to simulate thermal fluctuations and follows $< \xi(t) >= 0$ and $< \xi_i(t)\xi_j(t') >= 0$. F_i^c is the sum of all conservative forces acting on the ith particle, $F_i^c = F_i^{Spring} + F_i^{Soft-Repulsion}$. We calculate these forces by taking derivatives of the potentials with respect to the coordinate of the ith particle ($F_i = -\frac{\partial V}{\partial r_i}$). The motor force is denoted by F_i^m, with the sign $M = \pm$ depending on the motor type (contractile + or extensile −). We integrate the equation of motion using the Euler-Maruyama method.

$$\dot{r_i} = \mu F_i^c + \mu M F_i^m + \sqrt{2D\xi(t)}. \tag{3.2}$$

Scales: We are performing coarse-grained simulations using Brownian dynamics. To relate our simulation results to real-world numbers, we have established conversion factors: one unit length corresponds to 1 μ m, one unit of time is equivalent to 0.5 seconds, and one unit of energy is represented as k_BT with T=300K. The entire simulation is run for 10^8 steps with a time step of $\Delta t = 10^{-4}$, translating to 500 seconds of real-world time. In our simulation, we explore the impact of two motor types by varying signs. Additionally, the number of crosslinkers and linkages is varied to explore the role of the interconnectedness of the system and how it influences nucleus shape. In the active part of the system, we investigate the effects of motor force and motor lifetime (characteristic time τ_m) on nuclear shape. The turnover time $\tau_m = 40$ corresponds to a residence time of 20s. As presented in the table, we have utilized parameter values to perform these simulations.

The simulation box contains a total of 1.5×10^5 particles, of which 10^4 are part of the shell and 5×10^3 are chromatin particles. Each particle in the simulation is the same size, with a diameter $\sigma = 10nm$. The diameter of the deformable shell is not constant but has a mean value of 12 μ m. The rest length between two consecutive particles in chromatin is the diameter of a particle, but in the shell, it is the initial length found during the neighbor finding algorithm. We run 20 ensembles for each set of configurations. We only considered extensile motors for all the data and analyses present here. Data from

contractile motors and mixtures would be added in subsequent works later.

Shell spring constant	K_{Spring}^{Shell}	280
Chromatin spring constant	$K_{Spring}^{Chromatin}$	140
Crosslinker spring constant	$K_{Spring}^{Crosslinker}$	140
Linkage spring constant	$K_{Spring}^{Linkage}$	140
Soft core repulsion	$K_{Soft-Repulsion}$	140
Motor strength	F_a	5/10/15
Number of motors	N_m	100/200/400/600/800
Number of crosslinkers	N_c	1000/1500/2000/2500
Number of linkages	N_l	100/200/400
Mobility	μ	1
Diameter of monomers	σ	0.86178
Diameter of deformable shell	R_S	24
Motor turnover time	τ_m	2/20/40/80

Table 2 : Table of parameters used in the simulation. All values are in simulation units

3.2 Results

3.2.1 Abnormal nuclear shape formation and analysis

In our simulation, we observed that our model qualitatively reproduces the abnormal nuclear shape features seen in experimental figures as depicted in Fig 25 [58, 46, 41]. These abnormal shapes, such as bulges and wrinkles, were visually similar to those observed in the experimental data. To quantitatively compare our model with the experimental results, we developed a method inspired by Earth's topography, where mountains and valleys are represented on a flat sheet as a height map. Similarly, we mapped the spherical coordinates of our nuclear shape to a flat surface, creating a height map that visualizes

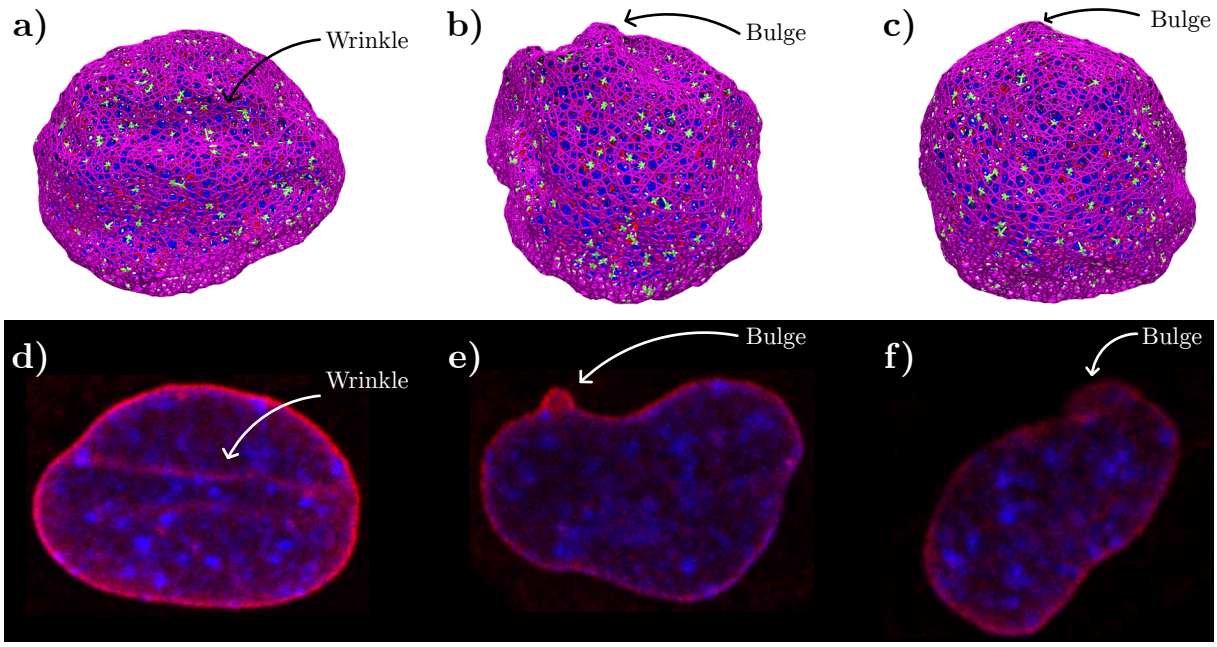

Figure 25 : *Simulation snapshots and experimental images showing abnormal cell nuclear shapes:* (a) Simulation snapshot of a nucleus, (b) and (c) simulation image depicting bulge, (d) experimental image showing a cell nucleus with a wrinkle and (e) and (f) showing the experimental image of bulges. The simulation captures the experimentally observed abnormal nucleus shapes. Experimental images courtesy: Prof. Alison Patteson lab.

the bulge and wrinkle formations.

In this height map, 0 μm represents the normal surface of the nucleus, which we determined by finding the nucleus's center of mass and average radius. With this reference, we identified particles above this surface as part of the bulge and particles below it as part of a wrinkle. In the height map, the average radius is shown in green, valleys or wrinkles appear in dark blue, while mountains or bulges appear in red.

To quantitatively analyze and distinguish the abnormal nuclear shapes, we developed an algorithm as follows. Let's consider the height map shown in Fig 26d as an example. To find the bulges, our algorithm starts by identifying the highest point on the map with respect to the average radius. This highest point is represented by the green dot within the red region in Fig 27a.

Next, to find the boundary of the bulge, we need to consider all the points around this highest point within a specific area and identify all the points above a certain height threshold, which are considered part of the bulge. To achieve this, we draw a circle around the highest point, dividing it into sectors with an adjustable angle, as shown in Fig 27b.

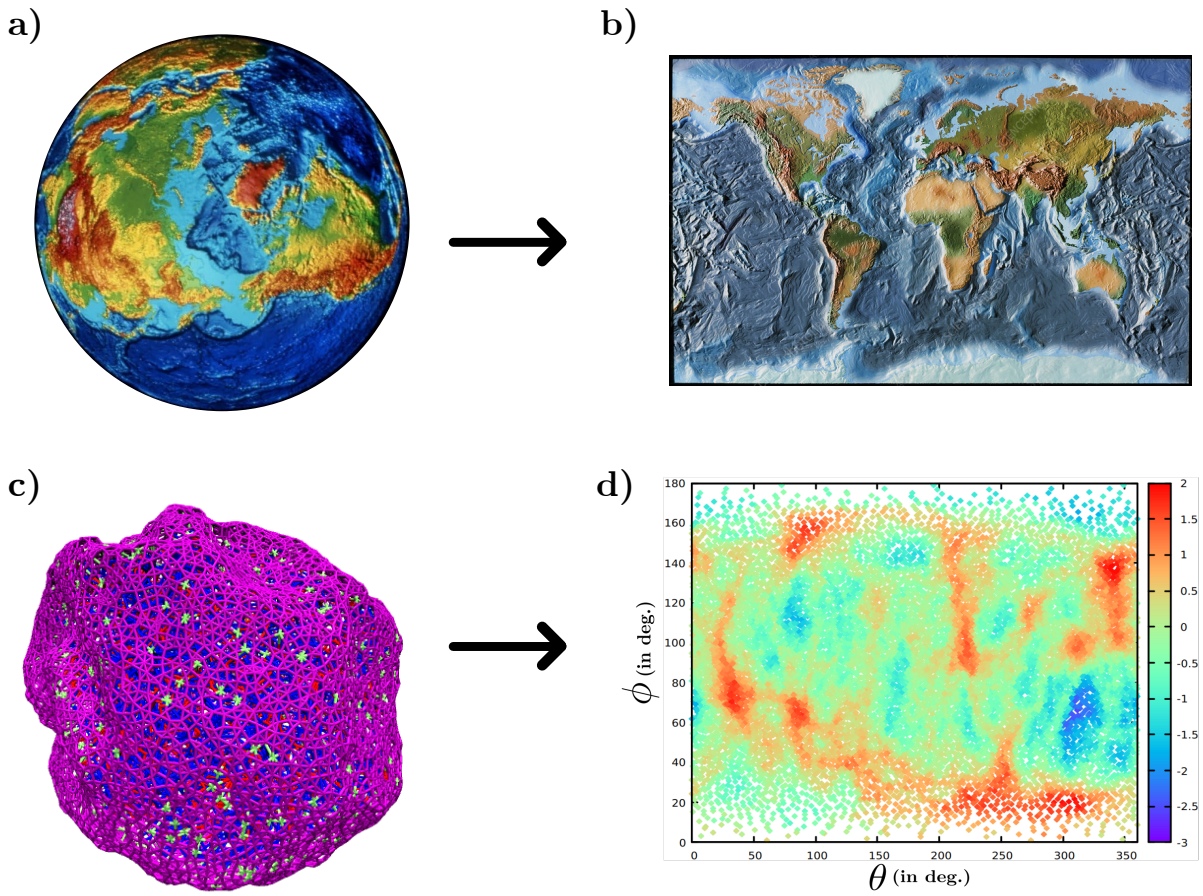

Figure 26 : *Mapping the abnormal nuclear shapes on a height map:* (a) Picture of Earth showing the hills and valleys on its surface. (b) A topographical mapping of the earth on a flat surface showing all hills and valleys (c) The nucleus simulation model showing the bulges and wrinkles similar to a) showing mountains and valleys (d) A height map similar to b) showing all bulges in red and wrinkles in blue. This mapping assists in quantifying the various properties of bulges and wrinkles, including their number and lifetimes.

Additionally, the circle is divided into bands with a tunable width, as shown in Fig 27c. These bands and sectors help divide the circle into smaller areas around the highest point.

The algorithm systematically goes to the first band closest to the height point and its first sector, checking all the points within that region. If all the points in that region are above the threshold, the algorithm moves to the next band and then to the next, moving outwards in the same sector. However, if a point is found below the threshold, it is considered a boundary point, and the algorithm proceeds to the next sector. For each sector, there can only be one boundary point, which may exist in any band, ensuring that enough points in all directions from the highest point are checked. This algorithm provides us with all the boundary points; the priceless can be tuned by making the sector

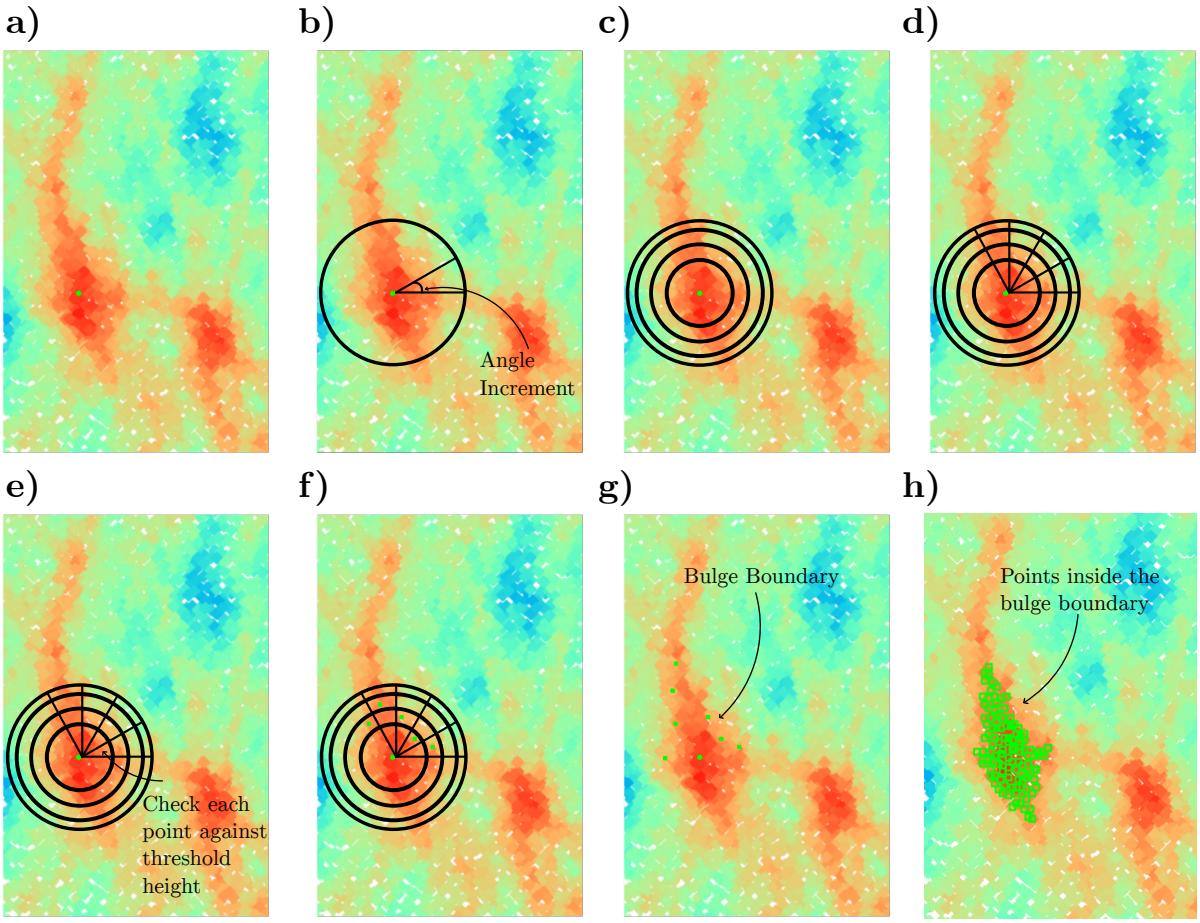

Figure 27 : *Algorithm for quantifying the abnormal nuclear shape including bulges and wrinkles:* (a) Finding the highest point on the map shown as a green dot, around which red points depict the points belonging to a bulge. (b) Making a circle with the height point as a center and drawing a sector of some angle. (c) Bands in the black of some bandwidth around the highest point. (d) Sectors and bands dividing the circle around the height point in smaller areas (e) In each sector, check each point's height; if more than the threshold height, check the next band going outwards; if a point is less than the threshold, consider this a boundary point, move to next sector and repeat to find all points as shown in (f) and in (g) By following the algorithm draw a boundary of bulge (h) All the points inside are part of the bulge.

angle and bandwidth smaller or larger. For clarity, we have shown only a few boundary points as green-filled boxes that the algorithm found in Fig 27g. Fig 27h shows all the points inside the boundary as green empty boxes, which are above the threshold height cutoff and considered part of the bulge.

Using our algorithm, we proceed to remove all the points found in the first bulge and search for the highest point among the remaining points to identify the next bulge. We repeat this process until we have found all the points above the average radius. However, we only consider regions as part of a bulge if the bulge contains more than ten points, as regions with just one or two points above the threshold may be insignificant. The same

algorithm can be applied to find the valleys by setting a negative height cutoff.

By employing this algorithm, we are able to identify and quantify all the bulges and valleys on the nuclear surface, allowing us to compare their numbers and stability with experimental data. This quantification provides valuable insights into the abnormal nuclear shape formations and their characteristics, aiding in comparing our model with experimental observations.

3.2.2 Chromatin interconnections lead to more and stable bulges

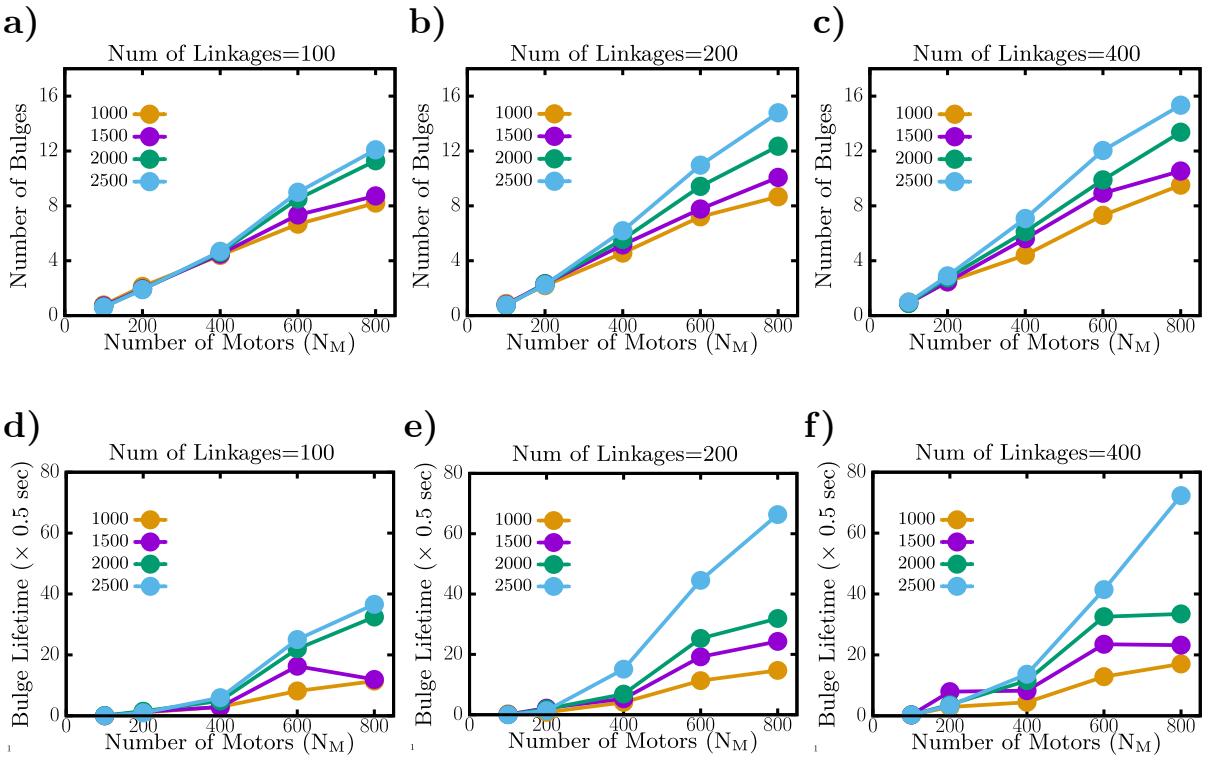

Figure 28 : *Effect of the number of motors, crosslinkers, and linkages on bulge numbers:* (a) Number of bulges as a function of number of motors for 100 linkages (b), same as (a) with 200 linkages (c), same as (a) with 400 linkages. The number of bulges increases with the number of motors and crosslinkers and weakly increases with the number of linkages. (d) Lifetime of a bulge as a function of number of motors with 100 linkages, (e) same as (d) with 200 linkages, (f) same as (d) with 400 linkages. Bulge stability increases with a motor number, crosslinkers, and loosely with linkages.

We observe that the number of bulges increases with the number of motors, as depicted in Fig. 28a, b, and c, regardless of the number of crosslinkers. The presence of more motors increases the overall local pushing forces within the nucleus that adds up locally, resulting in a higher number of bulges. This finding aligns with recent experimental

evidence, which demonstrates that decreasing the activity of a transcriptional factor, such as RNA Pol II, decreases the number of nuclei with blebs.

Moreover, we have found that crosslinkers play a crucial role in bulge formation. The number of bulges increases with an increase in crosslinkers, showing that the connectivity within the chromatin chain contributes to the formation of bulges. This phenomenon is intriguing because one might expect that a more condensed or tethered chromatin chain would be less prone to have a significant role in bulge formation. However, our results show the opposite effect, suggesting a complex interplay between chromatin connectivity and bulge formation.

Additionally, we found that the number of linkages has a weak influence on the number of bulges. While the overall bulge count increases with more linkages, especially for nuclei with higher crosslinker numbers, the effect is not particularly significant. This suggests that while linkages do play a role in bulge formation, their impact is less pronounced than that of crosslinkers.

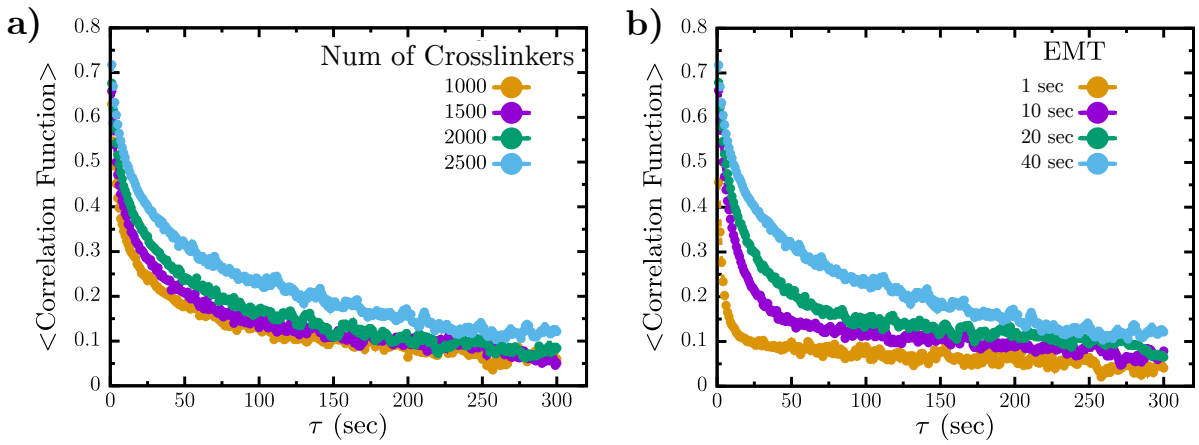

Figure 29 : *Quatifying bulge lifetime with the correlations of height maps:* (a) Correlation function with respect to the time window τ decays. Function decays slowly at high crosslinkers compared to low crosslinkers showing stable bulges with more crosslinkers. (b) Same as (a) with different expected mean time (EMT) or motor turnover time. High motor turnover time has slow decay than low turnover time showing stable bulges at high motor turnover time.

Another important aspect of the experimental quantification is the bulge lifetime, which involves counting the frames in which a bulge remains significant. In our simulations, we define bulges based on the mapping shown in Figures 26 and 27. Since the bulge position and the particles within the bulge change over time, we choose to define the

bulge lifetime using a decaying correlation function of height maps, which provides a characteristic lifetime for each set of parameters.

To achieve this, we create height maps for each frame, representing the height of particles relative to the average nucleus radius. We then calculate the correlation between height maps for frames with a time difference of one frame apart (frame one and two, frame two and three, and so on), the two frames apart till 300 frames apart. The height maps show a good correlation for small time differences since the bulges do not drift apart significantly. However, as the time difference τ increases, the height maps drift apart, as expected. We plot this time correlation function in Fig 29 and observe that the correlation decays as τ increases.

From the correlation function, we notice that the decay is slower for nuclei with higher crosslinkers than those with lower crosslinkers, indicating greater bulge stability for a higher number of crosslinkers. We attempted fitting various decay functions to quantify this observation, but none with a few parameters could provide a good fit. Instead, we used a thresholding method, where we set a correlation threshold of 0.3, and where the correlation function crosses this threshold, we consider the bulge lifetime. Throughout our work, we consistently employ this method to define the bulge lifetime, making the different bulge lifetimes comparable. Additionally, from Fig 29 b, we observe that the bulges become more stable as the motor lifetime increases. In the next section, we will detail the effects of a motor lifetime on bulge formation dynamics.

We systematically quantified the bulge lifetime for multiple parameter sets, as depicted in Fig 28 d, e, and f. The results indicate that an increase in the number of motors enhances the stability of bulges regardless of the number of crosslinkers. Nuclei with a higher motor count can generate sufficient localized force to sustain bulge formation for extended periods, leading to more stable bulges. Likewise, increasing the number of crosslinkers is associated with greater bulge stability. A higher number of crosslinkers allows the pushing forces generated by the increased motor count to reach the lamin shell more efficiently through various parts of the chromatin, contributing to the formation of stable bulges. Moreover, we found a weak correlation between bulge lifetime and linkages.

As the number of linkages increases, more stable bulges form, indicating improved force transmission to the lamin shell via the linkages. Our simulations show that both motor count and crosslinkers play significant roles in enhancing bulge stability, while linkages have a relatively smaller impact on bulge formation dynamics.

3.2.3 Motor turnover time increase leads to stable bulges, but bulge number saturates

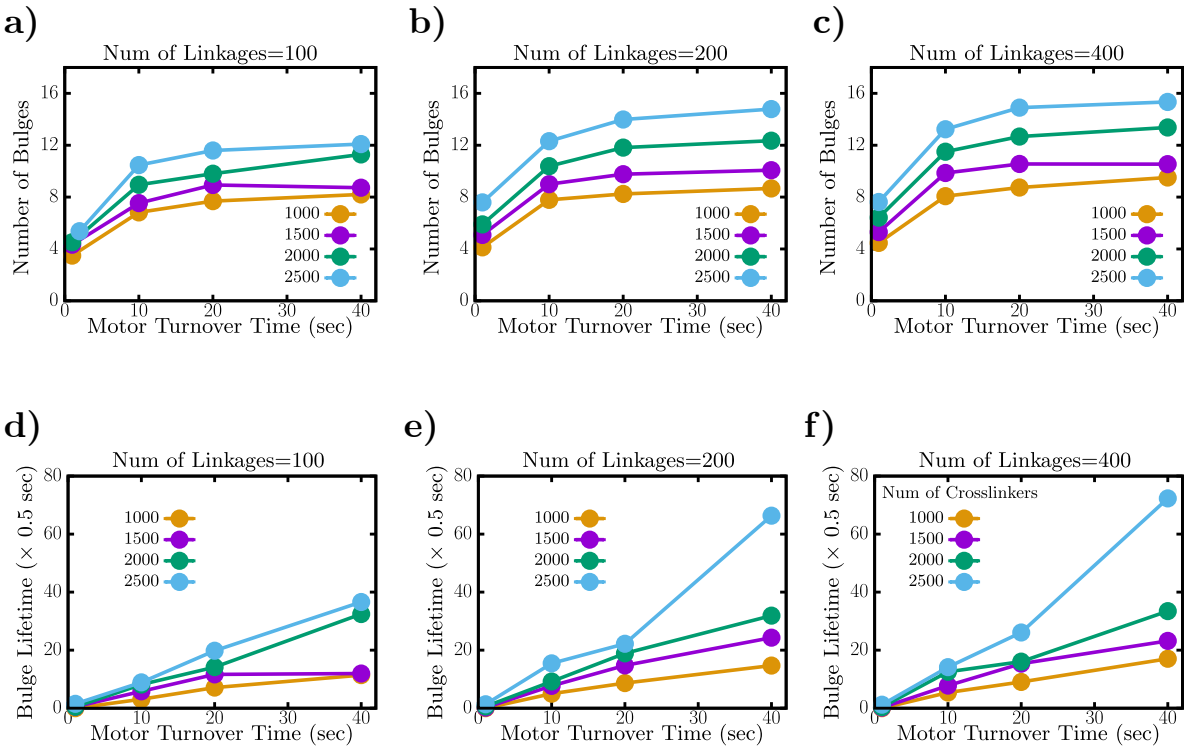

Figure 30 : *Effect of crosslinkers, linkages, and motor turn over time on bulge number and stability :* (a) Number of bulges as a function of motor turn over time with multiple crosslinker values and 100 linkages (b) same as (a) with 200 linkages (c) same as (a) with 400 linkages. Number bulge sutures with motor turnover as nucleus surface area is finite but increases with a number of crosslinkers and linkages. (d) Bulge lifetime as a function of motor turnover rate with multiple crosslinker numbers and 100 linkages (e) same as (d) with 200 linkages (f) same as (d) with 400 linkages. Bulge stability increases with motor turnover time, crosslinkers, and lossless linkages.

Transcriptional factors, such as condensin, cohesin, and RNA polymerase family, functions at the nanometer scale. However, the typical time these motors stay at one place along the chromatin chain remains to be discovered. Experimental data has shown that these motors exhibit movements, including switching off at one location and on at another. In our model, we use the motor turnover time as a parameter to investigate its

influence on the number and stability of bulges. We discovered that increasing the motor turnover time resulted in increased bulges. Motors switch on and off at a higher frequency at lower motor lifetimes, leaving insufficient time to form more bulges. However, bulges increased as we increased the motor lifetime to 10 seconds.

Further increases to 20 or 40 seconds did not significantly impact the number of bulges. Increasing the motor lifetime allows motors to remain at the same monomer for extended periods. However, it does not necessarily lead to a higher number of bulges, as the surface area of the nucleus is finite, imposing a limit on the number of bulges that could form. Thus, increasing the motor lifetime does not result in increased bulges. Additionally, we found that an increase in crosslinkers results in more bulges, and the effect is more pronounced, especially at a higher number of crosslinkers and linkages.

Our observations also revealed that increasing the motor turnover time leads to greater stability of the bulges, as depicted in Fig 30 d, e, and f. With lower motor lifetimes, the motors do not remain at one particle on the chromatin chain for extended periods, resulting in insufficient force generation for bulge stabilization. Conversely, the motors can push chromatin particles for longer durations at higher motor lifetimes, leading to relatively stable bulges. Moreover, we observe even more stable bulges when we increase the number of crosslinkers and linkages along with a higher motor turnover time. This indicates that forces generated by the motors can be sustained locally for a longer time and efficiently transmitted to the lamin shell, forming stable bulges.

3.2.4 Increase in chromatin correlation length increases the number of bulges and their stability

In the preceding sections, we investigated the role of crosslinkers, linkages, and motor lifetime on the number and stability of bulges. Now, to explore the underlying mechanism driving these observations, we focus on analyzing chromatin motion. In Figure 31, we present a vector map illustrating chromatin movement inside the nucleus and the nuclear lamin shell. To obtain this map, we considered a slab centered at the nucleus's center of mass with a width of d and identified all the particles within the slab at a given time

t during the simulation. Next, we analyze how the chromatin chain moves in relation to itself. For this, we consider the particles found within the slab at time t $+\Delta t$, where $\Delta t > 0$, and create vectors in time representing their movement. In Figure 31, the vectors are depicted alongside the lamin shell, shown in grey at time t and black at time t + Δt. The vector color represents the direction of movement. We observe that the vectors moving together push the lamin shell and lead to bulge formation, which is evident from the vectors within the golden rings. Hence, the coordinated movement of the chromatin chain is a crucial factor contributing to bulge formation.

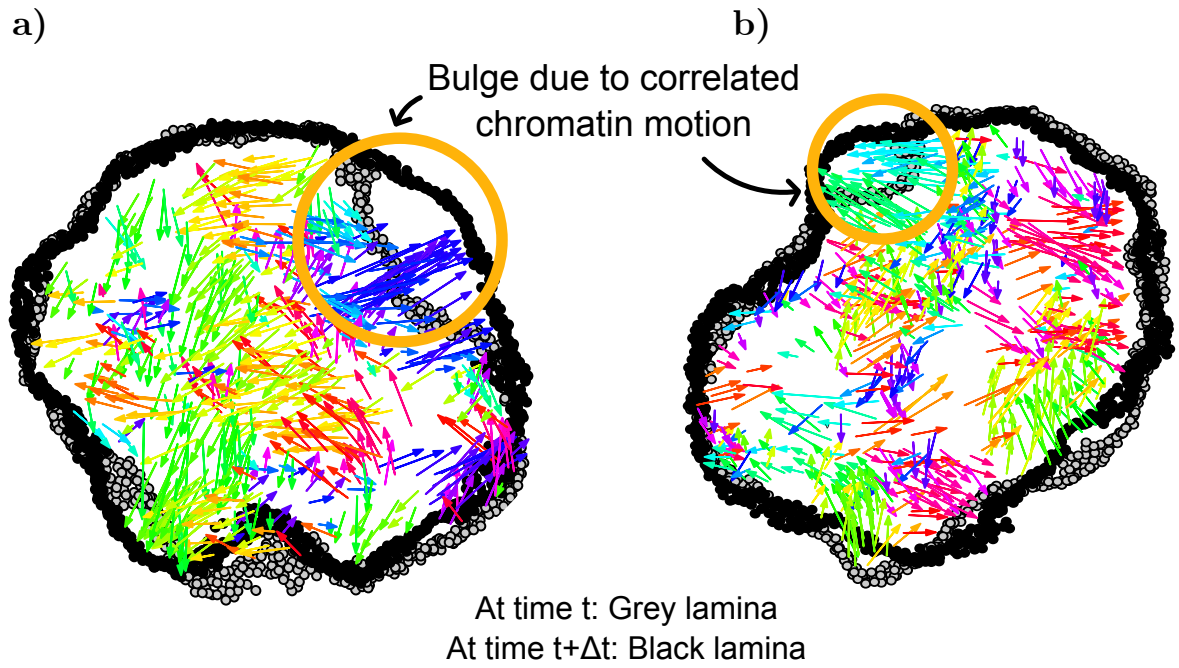

Figure 31 : *Correlated chromatin motion drives bulges:* (a) and (b) showing the vectors between particles at time t and t+Δt, color represents the direction. Lamina's position is black at time t and grey at t +Δt. Parts of chromatin moving together push the lamina outwards to form bulges, as shown in the golden rings suggesting correlated motion governs bulge formation.

To further quantify the coordinated motion of the chromatin chain, we calculated the chromatin-chromatin correlation function, denoted as C_r, which is a normalized spatial autocorrelation function represented by equation 3.3. In this equation, Δt represents the time window during which we analyze the chromatin motion, $N(\Delta r)$ is the total number of pairs of chromatin particles ij that are within a distance Δr of each other at the beginning of the time window, and $\mathbf{d_i}$ denotes the displacement of the ith chain particle over the time Δt.

$$C_r(\Delta r, \Delta t) = \frac{1}{N(\Delta r)} \sum_{N(\Delta r)} \frac{< \mathbf{d_i}(\mathbf{r}, \mathbf{\Delta t}) \cdot \mathbf{d_j}(\mathbf{r} + \mathbf{\Delta r}, \mathbf{\Delta t}) >}{< \mathbf{d^2}(\mathbf{r}, \mathbf{\Delta t}) >} \tag{3.3}$$

To compute this function, we first choose a time window $\Delta t = t_2 - t_1$ and a value for Δr greater than or equal to zero. Then, we identify all pairs of chromatin particles, ij, within a distance Δr at time t_1. Subsequently, these particles will have new coordinates at time t_2. To obtain the displacement vector $\mathbf{d_i}$, we subtract the position of the ith particle at time t_1 from its position at time t_2 (with respect to a fixed origin in the system). We perform the same procedure to find $\mathbf{d_j}$ and then take the dot product of the two displacement vectors, summing it over all the pairs identified earlier.

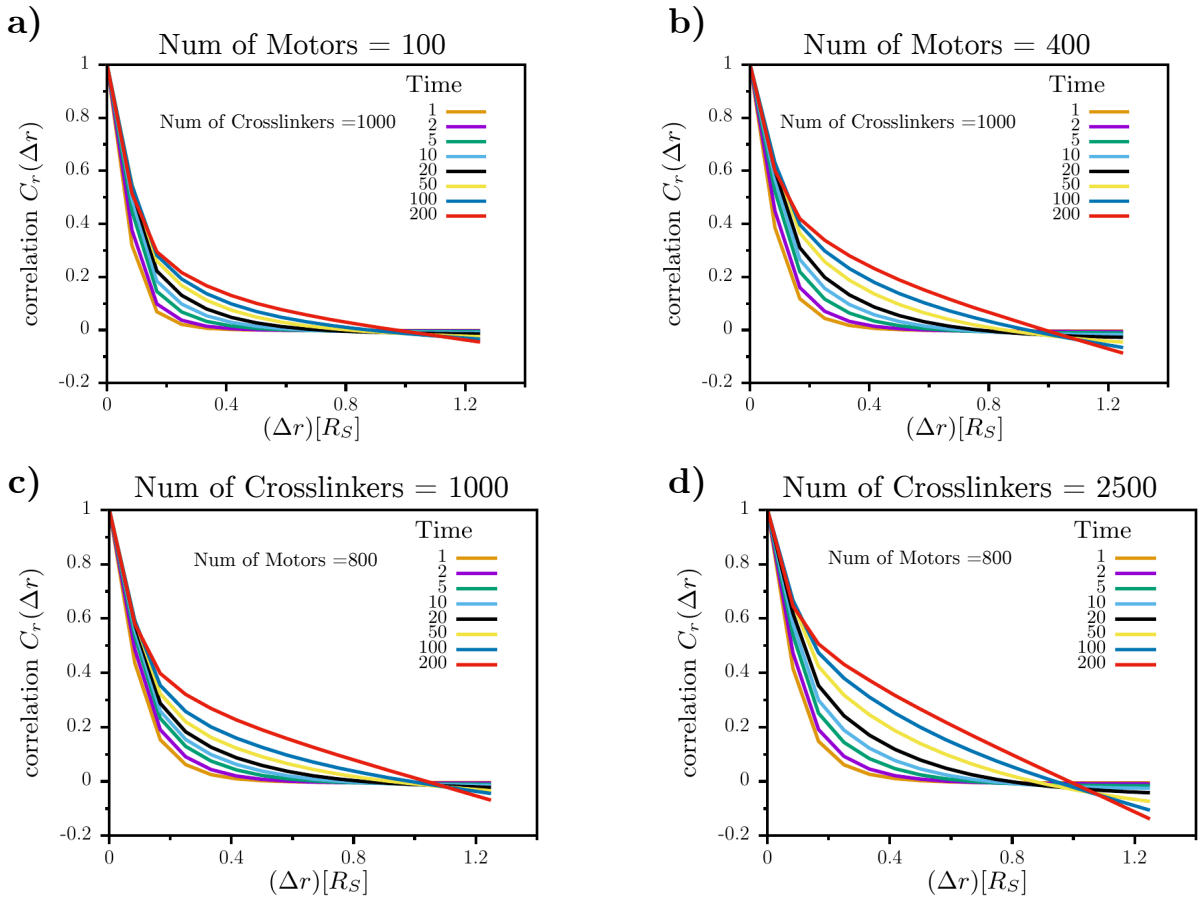

Figure 32 : *Chromatin correlation function:* (a) Correlation function decays as a function of Δr for 100 motors (b) same as (a) with 400 motors. With more motors, chromatin shows a high correlation, especially at larger time windows. (c) Correlation decays as a function of Δr for 1000 crosslinkers (d) same as (c) with 2500 crosslinkers. A higher number of crosslinkers results in higher chromatin correlation.

To normalize the function with respect to the initial vectors, we divide the dot product by the squared magnitude of all vectors formed due to the motion of all particles during

the time window Δt. Finally, we divide by the total number of ij particle pairs found initially to normalize the function further. This chromatin-chromatin correlation function helps us assess whether the chromatin chain moves together (positive correlation) or in opposite directions (negative correlation).

We analyzed the chromatin correlation motion by plotting the chromatin-chromatin correlation function, C_r, for various parameter sets, as depicted in Fig 32. The time window considered ranged from 1 second to 200 seconds, and the distance Δr was taken from zero to 1.2 times the size of the nucleus. Figures 32 a and b reveal that the chromatin correlation function decays more slowly with a higher number of motors, especially at larger time windows and distances. This indicates that the chromatin chain exhibits a more coordinated motion over time and space when more motors are present. In simpler terms, the motion of chromatin particles becomes highly correlated with an increasing number of motors. Furthermore, from Fig. 32 c and d, we observe that increasing the number of crosslinkers also enhances the chromatin correlation motion. In nuclei with a higher number of crosslinkers, the correlation function decays more slowly compared to those with fewer crosslinkers.

Furthermore, we extracted the correlation length by fitting plots in Fig 32 for a time window of 5 sec to the Whittel-Marten (WM) model function [156] given by eq 4.4, where $\nu = 0.2$ for all cases, r_{cl} is the correlated length, K_ν is the Bessel of the second type of order ν.

$$C_r(r) = \frac{2^{1-\nu}}{\Gamma(\nu)} \left(\frac{r}{r_{cl}}\right)^{\nu} K_\nu \left(\frac{r}{r_{cl}}\right) \tag{3.4}$$

We performed curve-fitting on the chromatin correlation function and extracted the correlation length, presented in Fig. 33. Our findings confirmed our earlier observations, showing that the correlation length increases with increased motor numbers and crosslinkers. Having previously established that bulge stability and number increase with higher motor numbers, crosslinkers, and motor lifetime, we show that an increase in chromatin correlation length also increases the motor number and crosslinker. Based on these results, we propose a mechanism that chromatin correlation motion drives the bulge

formation. Intuitively, when there are fewer motors and more crosslinkers, the system has insufficient force to drive bulge formation with the chromatin chain so tethered to each other. Conversely, with more motors and fewer crosslinkers, there is a lack of correlated motion to drive bulge formation. Thus, higher motor and crosslinker numbers are required for a high number of bulge formations and stability. A higher motor lifetime is required to form stable bulges in any parameter range.

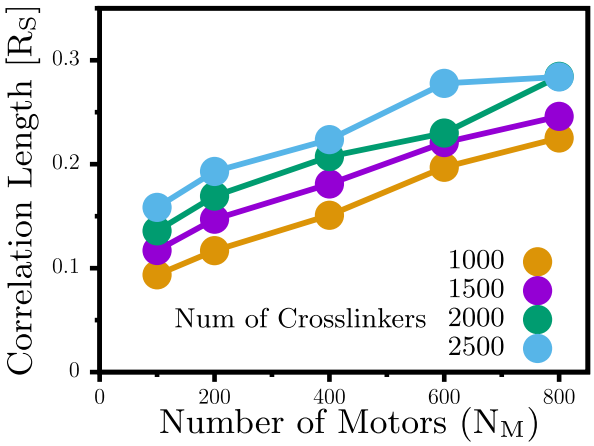

Figure 33 : *Chroamtin correlation length extracted from WM model:* Chromatin correlation length as a function of a number of motors for various values of crosslinkers. An increase in the number of motors and crosslinkers results in higher chromatin-chromatin correlation or more parts of chromatin moving together.

In conclusion, this demonstrates that an increased chromatin correlation length is associated with a higher number of bulges and their stability, shedding light on the underlying mechanisms governing bulge formation.

3.2.5 Nucleus under compression demonstrate compression stiffening behavior

Recent experimental studies have demonstrated that isolated nuclei exhibit compression stiffening behavior at low strains [148]. Compression stiffening refers to the phenomenon where a material becomes progressively harder to compress further as it undergoes increasing compression. In other words, the force required to compress the material increases as the compression level rises.

We subjected our simulation model to compression to gain insights into the underlying

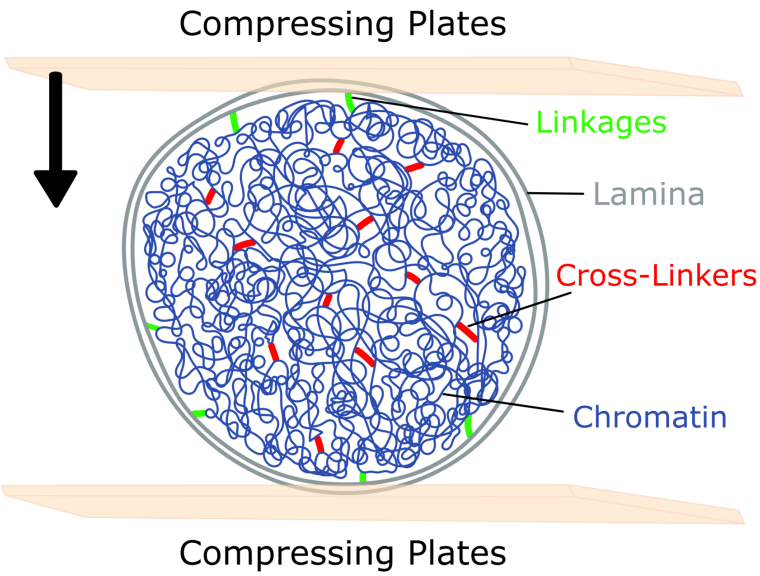

Figure 34 : *Sechamitic of the isolated nucleus under compression:* Nucleus simulation model with nuclear lamina in grey, chromatin in blue, crosslinkers in red, and linkages in red. The nucleus is under two parallel plates in light brown, with the bottom plate stationary and the top plate moving with different strain rates. Note that there are no motors in these simulation runs.

mechanism governing the cell nucleus's behavior under compression, as shown in Fig. 34. Our setup involved two parallel plates positioned at the top and bottom of the isolated nucleus model. The lower plate remained stationary, while the upper plate moved down with different strain rates. To understand the simpler case, we consider the passive case, with no motors switched on and the pushing or pulling on chromatin. However, all other components, including the lamin shell, chromatin chain, crosslinkers, and linkages, were retained, as illustrated in the schematic. For compressing the nucleus, we used boundary conditions like we used to condense the chromatin chain to spherical confinement, detailed in the methods section.

We conducted our simulations using two different strain rates, with one being ten times slower than the other, and both cases have a strain level of 50%. Figure 35 provides insight into the differences observed in the time series of the simulations for both strain rates. In Figure 35a, with the faster compression rate of 24 μ m/s, we noticed that the lower half of the nucleus shell remained relatively spherical. This suggests that the force generated due to compression had not effectively transmitted to the lower half of the shell, as the strain rate was too rapid for the material to respond in time. Conversely, in Figure

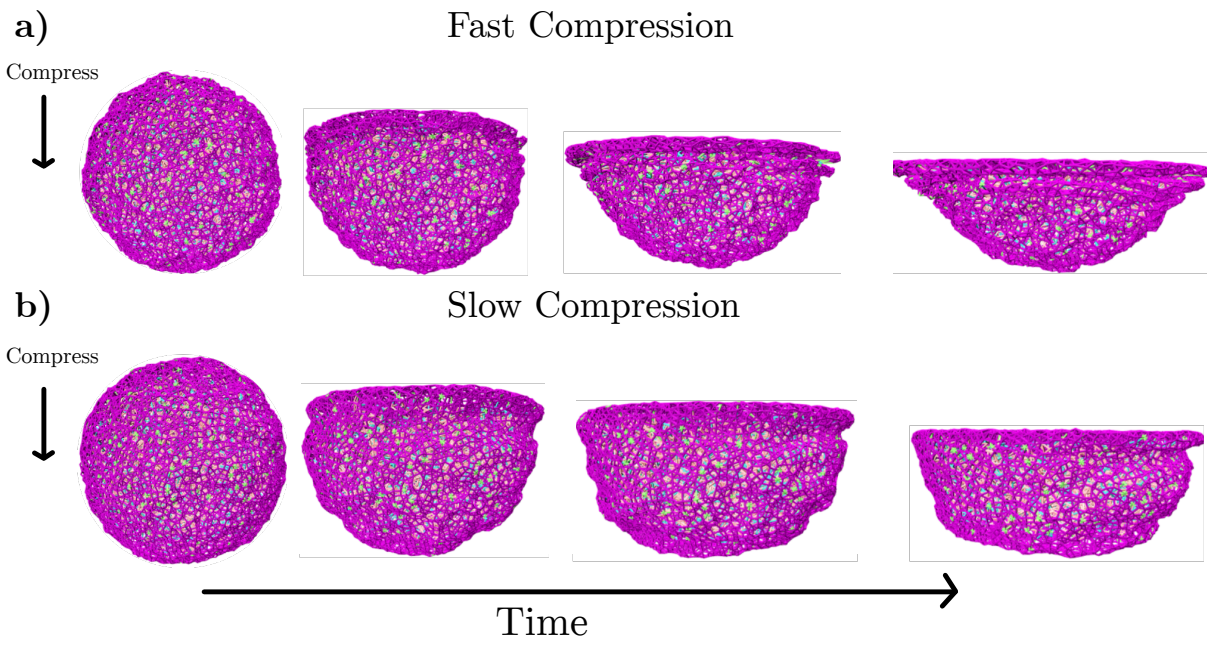

Figure 35 : *Time series of nucleus model under compression:* (a) At higher strain rates of 24 μm/s, the lower half of the nuclear shell remains spherical, indicating that the forces from the moving plate do not reach the lower half in time at this rate. (b) However, at a slower compression rate of 2.4 μm/s, the nucleus in the last panel shows a relatively elongated shape, resembling real-world compressed nuclei. The slower rate allows the nucleus enough time to relax and respond to the compression.

35b, with the slower compression rate of 2.4 μ m/s, the shape of the lower half of the shell became more elongated, which resembled more with the experimental images. In this case, the forces from the plates had sufficient time to propagate to the lower half of the nucleus, resulting in a more realistic response to compression.

To better understand the behavior, we plotted the force vs. strain curves for both cases and compared them to an empty shell, as shown in Figure 36. We considered an empty shell as a control to ensure that the compression stiffening behavior of the nucleus on the inside matters. As depicted in Figure 36a, we observed that compressing the nuclear lamina with chromatin required more force compared to an empty shell for both compression rates. Moreover, the inset reveals that the compression stiffening behavior at strains less than 10% captures the experimental data. Similarly, we found similar behavior at low strain levels with slower compression rates, as shown in the inset of Figure 36b.

Furthermore, we noted that for reaching the same strain level, a different magnitude of force was required for slow and fast compression. While the forces in Figure 36 are in simulation units, the comparison remains valid, as the conversion factor to real-world units

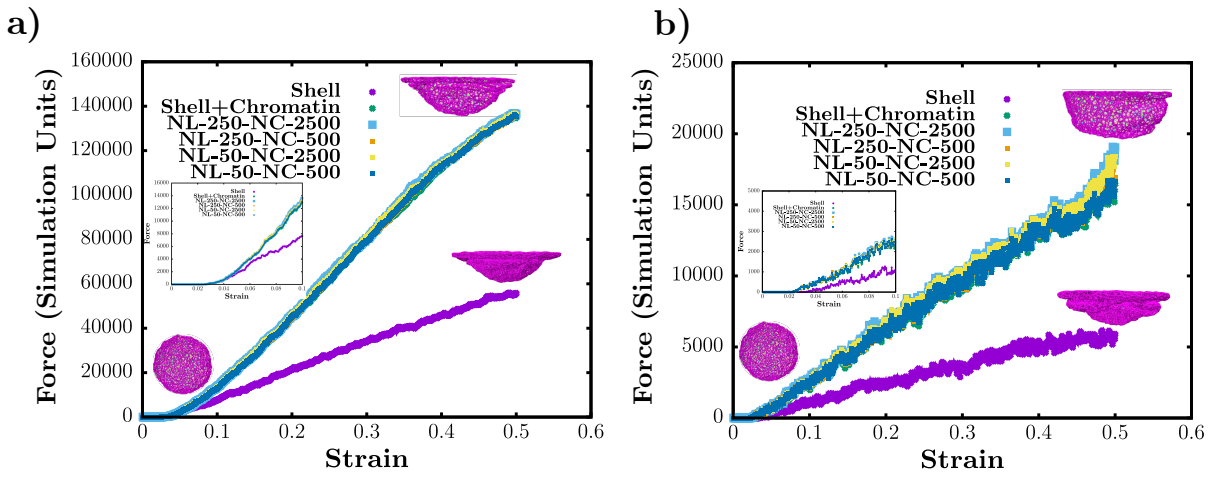

Figure 36 : *Force vs. strain curves of nucleus compression:* (a) Faster compression rates show a linear force-strain curve for the empty shell, while the nucleus with chromatin exhibits compression stiffening behavior at low strain, as seen in the inset. (b) Slower compression rates also show a linear force-strain curve for the empty shell but with more surface wrinkles. The compression stiffening behavior at low strain is less pronounced in this case as shown in the inset. Notably, different strain rates apply forces with an order difference to achieve the same strain, indicating the viscoelastic behavior of the chromatin chain under compression.

is consistent for both cases. Interestingly, the force required to achieve a 50% strain during slow compression was one order of magnitude less than that during fast compression. This behavior indicates that in faster compression, the chromatin chain does not have enough time to move and forms a jamming front at the top of the nucleus. In contrast, during slow compression, the chromatin chain has sufficient time to move into nooks and crannies within the shell under compression.

Moreover, our investigations revealed that the number of crosslinkers or linkages did not significantly impact the compression behavior, as shown in Figure 36. Regardless of the number of crosslinkers or linkages, the compression behavior of the nucleus remained similar in both strain rates.

In conclusion, the behavior observed under compression points to the viscoelastic nature of the chromatin chain. Without attractive forces, the chromatin chain has enough time to slip and move over on itself, requiring lower forces to achieve a 50% strain at low strain rates. However, under faster strain rates, the chromatin chain may form a jamming front at the upper plate, stopping its reorganization, which eventually requires a higher force for compression.

3.3 Conclusions and Discussions

We developed a computational model to investigate the impact of chromatin activity and connectivity on the formation of abnormal nuclear shapes. Additionally, we explored the material properties of the nucleus when subjected to compression. To analyze the formation and stability of bulges and wrinkles, we employed the height maps analysis method to quantify these features with respect to other parameters in the system. Our findings shed light on the crucial role of motor numbers in generating bulges. Increasing the number of motors not only leads to a higher number of bulges but also promotes their stability.

Moreover, we made a surprising discovery regarding the influence of crosslinkers. We discovered a non-intuitive contribution of crosslinkers in bulge formation, finding that increasing the chromatin connection to itself results in a higher number of bulges that are increasingly stable. Since the chain is more connected to itself, it is relatively less free to move but still forms more stable bulges. Furthermore, we investigated the role of linkages in the system. Our simulations indicated a weak dependence between linkage numbers and the number and stability of bulges.

We also investigated the influence of motor lifetimes on abnormal nuclear shapes. In the real world, motors on chromatin constantly move, and we incorporated this behavior into our model by introducing a motor turnover time, representing the switching off and on mechanism. Surprisingly, our results revealed that increasing the motor lifetime does not lead to an increase in the number of bulge formations but saturates at a larger motor lifetime. The reason behind this observation is the finite surface area of the nucleus. Although motors staying at a specific location exert forces for longer, the overall number of bulges does not increase significantly because the available surface area for bulge formation remains limited. However, we did find that higher motor lifetimes contribute to greater bulge stability. This is because the bulges are subjected to the forces generated by motors for more extended periods, leading to their increased stability.

Furthermore, We also examined chromatin motion inside the nucleus and observed correlated movements. To quantify this correlated motion, we employed a correlation

function and extracted a correlation length. Notably, our findings demonstrated that the chromatin correlation motion intensifies with an increase in the number of crosslinkers and motors.

In summary, our findings suggest that the chromatin correlation motion plays a crucial role in driving bulge formation. An increase in motor numbers leads to enhanced correlated motion of the chromatin chain, resulting in more and stable bulges. Similarly, a higher number of crosslinkers also contributes to a longer correlated length of chromatin motion, leading to the formation of more and stable bulges.

But why do we need a higher number of motors and crosslinkers to produce more stable bulges? The answer lies in their combined effect on the system. If we have more crosslinkers but fewer motors, the tethered chromatin chain lacks the necessary force to move and rearrange effectively, hindering bulge formation. On the other hand, having a higher number of motors but fewer crosslinkers results in constant movement of the chain without sufficient correlated motion to generate localized bulges. Therefore, a balanced interplay between motors and crosslinkers is essential to promote stable bulge formation on the nucleus surface.

In the second part of our study, we aimed to investigate the compression stiffening behavior of the nucleus. To achieve this, we placed our computational model between two parallel plates and subjected it to compression at different strain rates. By analyzing the results, we gained insights into the mechanical properties of the nucleus under compression. In our simulations, we observed that at faster compression strain rates, the nucleus's lower half remained spherical. This suggests that the forces generated by the moving plate did not have sufficient time to reach the lower half of the nucleus, and as a result, it retained its original shape. On the other hand, when subjected to slower compression rates, the nucleus showed a more oblong shape at the end of the simulation. This indicates that the forces were effectively transmitted throughout the nucleus, leading to a shape closer to what was observed in experiments.

Furthermore, our force-strain curve analysis revealed an intriguing behavior. We noted that the force required to reach the same strain was an order different for slow and fast

compression rates. This suggests that the nucleus exhibits viscoelastic behavior under compression, with its response varying depending on the rate of compression applied. Additionally, we successfully captured the experimental observation of compression stiffening at lower strains, where the nucleus exhibited increased stiffness as it experienced more compression.

Our work stands out as one of the first studies to investigate the formation of nuclear bulges and wrinkles from the perspective of active chromatin. While previous models have considered the role of external tethering and changes in lamin shell mechanical properties in shaping the nucleus [46, 57], our focus has been on the active dynamics of chromatin. In recent works, chromatin motion has been explored with immovable boundaries, which may only partially capture the realistic behavior of cell nuclei [157, 158, 159]. In contrast, our computational model incorporates the dynamic movement of chromatin within a deformable spherical shell, making it more representative of real-world cell nuclei. By taking into account the activity of chromatin and its interactions with crosslinkers, linkages, and motor properties, our approach provides a more comprehensive understanding of nuclear shape formation, setting it apart from existing models.

Given the complexity of nuclear internals, our future work aims to delve deeper into the effects of nucleosomes and the recently discovered actin within the nucleus on chromatin and nuclear lamin dynamics [160, 161, 162]. We plan to investigate how these components contribute to the nucleus shape during compression and relaxation. Additionally, we are keen to explore the specific roles of euchromatin and heterochromatin in nuclear dynamics, as they play crucial roles in gene regulation and overall nuclear organization. By addressing these aspects, we hope to gain a more comprehensive understanding of the intricate interplay between various components inside the nucleus and their impact on nuclear shape and behavior.

Chapter 4

The role of vimentin-nuclear interactions in persistent cell motility through confined spaces

Cell migration is a fundamental process that contributes to building and maintaining tissue. To be able to migrate, the cell cytoskeleton, which is comprised of three dynamic polymeric systems: F-actin, microtubules, and intermediate filaments (IFs), generates forces. While actin and microtubules are more studied cytoskeletal filaments, intermediate filaments (IFs) also play a role in a range of cell and tissue functions [163, 164, 165]. Vimentin is an IF protein whose expression correlates with *in vivo* cell motility [66, 166] behaviors involved in wound healing [167, 168] and cancer metastasis [169, 170], and, yet, its role in three-dimensional cell migration is poorly understood.

In vivo, cells move through a confining tissue environment made out of other cells and extracellular matrix (see. Figs 37(a) and 37(b)) [171]. Emerging experimental studies show that the structure and dynamics of the cytoskeleton in three-dimensional motility differ from those for cells on surfaces [171, 172]. In confined settings, actin tends to accumulate at the cell cortex [173] and microtubules align with the direction of the confining track [174]. Moreover, in highly confining environments, the nucleus, one of the stiffest organelles in the cell, can be an inhibitor of cell migration due to steric hindrance [175]. Earlier cell motility models in such environments, therefore, focus on the nucleus [176, 177, 178], in contrast with cell motility models for surfaces [179]. Recent studies have shown that in three-dimensional settings the centrosome displays an increased probability to be near the rear of the cell [180]. When cells change direction in a narrow track, the centrosome repositions, moving from one side of the cell to the other, to repolarize the cell by developing a new trailing edge of the cell and setting up the polar direction of the cell. Interestingly, the nucleus appears to be decoupled from this phenomenon in that the removal of the cell nucleus does not alter the centrosome repositioning in most cells [180]. Though for strong confinement, the cell nucleus will presumably play a more dominant role in the repositioning of the centrosome as it deforms.

Given the roles of actin, microtubules, and centrosome positioning in confined cell motility, one is naturally led to ask about the role of vimentin, which couples to both actin and microtubules and forms a cage around the cell nucleus [181]. Recent experiments [68,

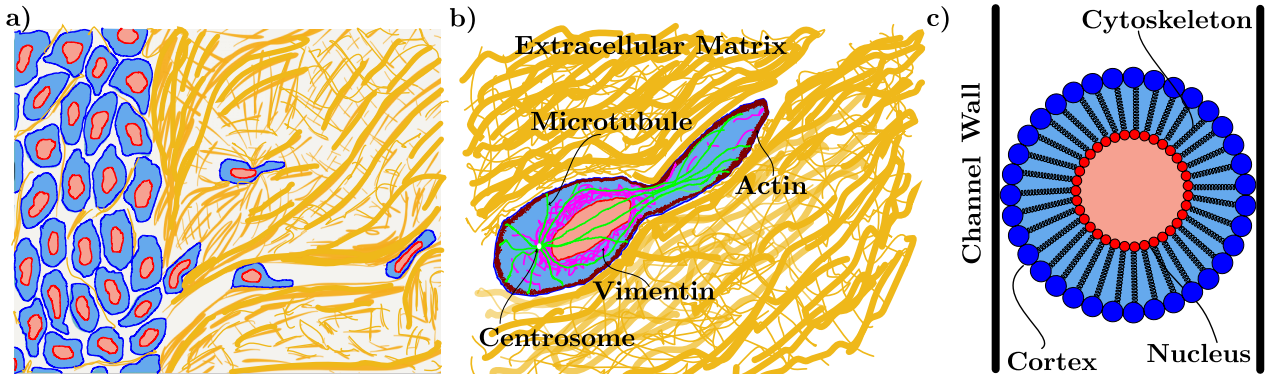

Figure 37 : *Modeling confined cell motility:* (a) Cells move through confining environments due to the extracellular matrix (in gold) and other cells. (b) Schematic of an individual cell with a cytoskeletal network containing actin, microtubules, and intermediate filaments, a nucleus, and a centrosome connected to the nucleus via the protein dynein. (c) A simulation model for the cell: The cortex is made up of blue monomers connected with springs, the nucleus is also made up of red monomers with springs connecting them. The bulk cytoskeletal network is simplified and modeled as springs connecting the nucleus and the cortex. The cell and nucleus contain cytoplasmic and nucleoplasmic material, each of which is modeled as area springs.

182] highlight new roles of vimentin in mediating cell speed and cell persistence in three-dimensional confining environments. Specifically, when comparing the motion of wild-type mouse embryonic fibroblasts (mEFs) with their vimentin-null counterparts moving through three-dimensional micro-fluidic channels, the loss of vimentin increases cell motility and increases rates of nuclear damage in the form of nuclear envelope rupture and DNA breaks. Moreover, unlike in unconfined motility, the loss of vimentin increases the spontaneous persistent migration of cells through 3D micro-channels and 3D collagen matrices [183].

Inspired by these experiments, we seek to quantitatively understand the role of vimentin in confined cell motility via a computational model. To do so, we develop a minimal, yet detailed, cell motility model incorporating actin, microtubules, and vimentin. The starting point of the model is the notion that vimentin plays a distinct role in mediating forces between the actomyosin cortex and the nucleus [115, 184]. Our model, therefore, contains both an actomyosin cortex and a nucleus, whose interaction via a set of linker springs is strengthened by the presence of vimentin. With this level of detail, a new mechanism for cell polarity for motility in which vimentin plays an important role naturally emerges. As the cell moves through the model micro-channel, we will quantitatively show how vimentin modulates cell speed, nuclear shape, dynamics, and cell persistence. In addition

to quantitative comparison with experiments, we pose new insights for the role of vimentin in confined cell motility more generally. In particular, we address the upregulation of vimentin typically found in the epithelial-mesenchymal transition [166] in terms of how vimentin affects a cell's interaction with its environment.

4.1 Model

The players: We begin with the cellular cytoskeleton, composed of actin, microtubules, and intermediate filaments. The persistence length of actin filaments is smaller than microtubules but larger than intermediate filaments [185]. Myosin motors exert forces on actin filaments to reconfigure them. Many actin filaments and myosin motors reside in proximity to the cell membrane to form the actomyosin cortex. The actomyosin cortex is an important piece of the cell motility machinery as its reconfiguring drives cell motion. Microtubules typically originate from the microtubule-organizing center, or centrosome, and have a crucial role in cell polarity as they as required to generate traction forces [186]. Microtubules also have a role in controlling cell shape as they typically span the entire cell and are the stiffest cytoskeletal filaments [185]. Vimentin filaments exist as a cage or mesh structure around the nucleus and are also present in the cytoskeleton in fibrous form as can be seen in Fig. 37(b) [181, 115]. Studies show that vimentin provides structural integrity to the cell [187, 188].

The nucleus is typically the largest, and stiffest, organelle in the cell, yet it is still deformable. Recent studies showed a cell under a highly confined environment, and thereby, the nucleus is so squeezed such that DNA becomes damaged [187]. Cells cannot move through a particular confining geometry if the nucleus cannot do so [175]. Therefore, the nucleus is also an important player in confined cell motility.

These individual players do not act independently of each other. Major cytoskeletal network actin, microtubules, and intermediate filaments are also highly interconnected with each other [189]. For instance, vimentin and actin directly interact with each other via the tail domain of vimentin [190]. Moreover, plectin is a major crosslinker among all three types of filaments [191]. In addition, the interconnected cytoskeletal networks and

the nucleus are also connected to each other. For instance, LINC(Linker of nucleoskeleton and cytoskeleton) complexes made of nesprins and SUN (Sad1 and UNC84) proteins act as connecting bridges between nucleoskeleton, containing lamins, and the actin network in cytoplasm [141]. Microtubules are also joined to the nucleus via kinesin-1 which talks to nesprin-4 [142]. Intermediate filaments are connected via plectin which connects to nesprin-3, which is joined with nucleus [143]. Disruption of these nucleus-cytoskeleton links also leads to impairment of 3D cell migration [192, 193]. The nuclear envelope, or nuclear cortex, consists of inner nuclear lamins and outer vimentin.

Spring network: Given the complexity of such interactions, to model the interplay between cell mechanics, shape, and motility, we took a reductionist approach and simplified this highly tangled picture to a two-dimensional network of harmonic springs with an outer ring of springs representing the cellular cortex and an inner ring of springs representing the nuclear envelope, and harmonic springs connecting the cellular cortex with the nuclear cortex (see Fig. 37(c)). Our model is a two-dimensional cross-section of the three-dimensional system. As we can see from the schematic, each cell cortex monomer is joined to each nuclear cortex monomer via a linker spring. Each spring type, the cellular cortex, the nuclear cortex, and the interacting bulk linker spring, has its own stiffness with the respective potential energies $V_{cc} = \frac{K_{cc}}{2}(r_{cc} - r_{cc,o})^2$, $V_{nc} = \frac{K_{nc}}{2}(r_{nc} - r_{nc,o})^2$, $V_l = \frac{K_l}{2}(r_l - r_{l,o})^2$, respectively, with r_{cc} denoting the distance between the centers of neighboring cell cortex monomers, for example, and $r_{cc,o}$ represents the rest length of the spring. We also include potentials in the form of two area springs, $V_{cell} = \frac{K_{cell}^{area}}{2}(A_c - A_{c,o})^2$ and $V_{nuc} = \frac{K_{nuc}^{area}}{2}(A_n - A_{n,o})^2$, where A_c and A_n denote the areas of the cell and nucleus, respectively. The two area springs prevent the cell and the nucleus from collapsing as the cell becomes increasingly more confined.

How do we explore the role of vimentin in such a mechanical model, particularly when considering wild-type fibroblasts versus their vimentin-null counterparts? Since vimentin-null cells are softer than wild-type cells [188] and exhibit more DNA damage [187], to capture both cell lines we change the stiffness of the cytoplasmic/linker springs K_l and nucleus area springs K_{nuc}. Since removing vimentin does not significantly affect the

cortical stiffness [188], we do not alter the cortical spring constant among two cell lines.

The cell also interacts with its confining walls which are considered to be adhesive due to fibronectin or collagen I or some other kind of protein that is usually coated inside the channels. Specifically, the micro-channel is modeled as two lines of wall monomers fixed in place that interact with the cell cortex monomers via adhesion. In previous studies, adhesion to the surface is modeled as catch and slip bonds [194, 195], where the cell forms a bond to the substrate, and then as it moves those connections peel off. We, therefore, model the adhesion interaction with the Weeks-Chandler-Anderson potential, or

$$V_{cell-wall} = \begin{cases} 4\epsilon_{Ad}\left[\left(\frac{\sigma}{r_{cw}}\right)^{12} - \left(\frac{\sigma}{r_{cw}}\right)^{6}\right] + \epsilon & r \leqslant 1.2\sigma \\ 0 & r > 1.2\sigma, \end{cases} \tag{4.1}$$

where ϵ quantifies the adhesion strength and the minimum of the potential is located at $2^{1/6}\sigma$. While the potential is purely repulsive in short range, there is an attractive component (with a minimum) and a repulsive component. The minimum of the potential thus represents a typical integrin length [196]. We did not vary the adhesion strength between the two cell lines.

Dynamics: As the cell moves, actin is polymerized at the leading edge of the cell to translate the cell in a particular direction with microtubules setting the direction [197]. We model actin polymerization via an active force, $\mathbf{F}_a$. The active force is present for half cortex of the cell, the leading edge half, and has a magnitude F_a. The direction of $\mathbf{F}_a$ is initially chosen to be towards the opening of the micro-channel, which determines the leading edge half—its polarization direction. There are small fluctuations in the direction of $\mathbf{F}_a$ as it moves through the micro-channel. In addition to adhering to the wall, it has been observed that in confined environment experiments, actin bundles start forming at the edges of the cell where it is interacting with the walls [198]. We are proposing that due to this interaction with the wall, the cell generates forces to enhance motility in the direction in which it is polarized. Therefore, any cell cortex monomer with some proximity of a wall monomer exerts an additional force, $\mathbf{F}_w$ in the direction of the leading edge.

Now that we have detailed the forces involved, here is the equation of motion for each

cell monomer of type i at position $\mathbf{r}_i$:

$$\dot{\mathbf{r}}_i = \mu_i(\mathbf{F}_a + \mathbf{F}_w + \mathbf{F}^c) + \sqrt{2D_i}\xi_i(t), \tag{4.2}$$

where $\mathbf{F}_a$ is an active force representing the actin forces at the front end of the cell in the direction of motion and $\mathbf{F}_w$ denotes the force generated at the wall in the direction of the leading edge. Finally, $\mathbf{F}^c$ represents the conservative forces in the system, or $\mathbf{F}^c = \mathbf{F}_{cc} + \mathbf{F}_{nc} + \mathbf{F}_l + \mathbf{F}_{cell} + \mathbf{F}_{nuc} + \mathbf{F}_{cell-wall}$), which are the two-body springs, the area springs, both modeling the mechanics of the cell, and the adhesion force between the cell and the confinement (wall). For the parameters varied in the simulations, see Table 1. We use simulation units defined as unit simulation length equal to μm, unit simulation time is equal to sec and unit simulation force is nN. As for other parameters, $\mathrm{D_{cc}} = 0.02\,\mu\mathrm{m}^2/s$, $\mathrm{D_{nc}} = 0.04\,\mu\mathrm{m}^2/s$ and $\mu_{\mathrm{cc}} = 0.01\,\mu\mathrm{m\,nN/s}$, $\mu_{\mathrm{nc}} = 0.02\,\mu\mathrm{m\,nN/s}$ for both cell lines. The respective diameter of the monomers are $\sigma_{cc} = \sigma_{cw} = 2\,\mu m$, $\sigma_{nc} = 1\,\mu m$, all neighbouring springs in actomyosin cortex and nuclear cortex is $2\,\mu m$ and $1\,\mu m$ respectively and linker spring length is $5.73\,\mu m$. Our simulations used 36 monomers in the both cortices, 74 monomers to simulate each side of the straight part of the wall, and 7 monomers for each side of the slanted channel entry and exit. To iterate Eq. 2, we use the Euler-Marayuma method.

Polarity-mechanism: If one allows for large fluctuations in the direction of $\mathbf{F}_a$, the probability is enhanced of the cell turning around in the channel. Recent experiments in two-dimensional motility suggest that removing the centrosome induces microtubules to grow symmetrically in all directions and, as a result, the cell forms lamellae in many directions and, therefore, loses its polarization [202]. In a 3D setting, the centrosome is typically found to be posterior of the cell, and microtubules are oriented in the direction of motion (for certain cell types) [174]. Therefore, the position of the centrosome sets the polarity of the cell by defining the tail/back of the cell during migration since the change in cell direction results only after the centrosome moves to the new posterior side of the cell [203]. Cell length is also found to be correlated with the time required

Parameters	Wild-type	Vimentin-null	Refs.
K_{cc}	$100\,nm/\mu m$	$100\,nm/\mu m$	[188]
K_{nc}	$1000\,nm/\mu m$	$1000\,nm/\mu m$	[199, 200]
K_l	$10\,nm/\mu m$	$1\,nm/\mu m$	[188, 200]
K_{cell}^{area}	$0.01\,nm/\mu m^3$	$0.01\,nm/\mu m^3$	-
K_{nuc}^{area}	$0.05\,nm/\mu m^3$	$0.005\,nm/\mu m^3$	-
F_a	$3\,nN$	$3\,nN$	[201]
F_w	$3\,nN$	$3\,nN$	-
ϵ_{ad}	$1\,nN\,\mu m$	$1\,nN\,\mu m$	-

Table 3 : Table of parameters used, unless otherwise specified, and kPa is converted nm/μm for the cortex, nucleus, and linker stiffnesses using a relevant length scale.

for cells to change the direction, which is the time the centrosome takes to move to the other side of the cell to define a new tail [180]. Therefore, we posit that the more the centrosome is located away from the cell center of a crawling cell, the more biased cell migration becomes. Thus, the centrosome is essential for the preservation of polarized cell morphology.

While there is no explicit centrosome in our model, the centrosome is also connected to the nuclear outer membrane by a protein emerin [204]. Given the strong coupling between the nucleus and the centrosome, we effectively include a centrosome and a direction of cell polarity as determined by the direction of microtubule polymerization. To do so, we define $\mathbf{d}$ representing the difference between the center of mass of the cell and the center of mass of the nucleus. Its angle is measured from the positive x-axis. For incorporating the centrosome role in motility, we define the following empirical equation:

$$\Delta\theta = \frac{\pi}{2}\left(1 - \frac{|\mathbf{d}|}{R_{nuc}}\right), \tag{4.3}$$

where R_{nuc} denotes the rest radius of the nucleus. With this empirical equation, we define the bounds on the direction a cell can take. We take the nuclear cortex-cellular cortex (NC-CC) axis as our reference axis and for the upper bound and lower bound we can add and subtract $\Delta\theta$ from this axis. See Fig. 40(a). Then, we choose a random angle under these bounds and that represents the direction of the nuclear, or centrosome, axis given the strong coupling between the two, which then drives the direction of migration.

What is the timescale for changing $\Delta\theta$? We assume that vimentin acts as a template for microtubules in the cell on a time scale of 10-20 minutes since (1) vimentin has a slow turnover rate than microtubules and (2) microtubules in vimentin-null cells show less orientation than in wild-type cells [205]. Therefore, this polarity mechanism repeats itself in every 15 min. as on average this is the time after which vimentin restructures. We have used the initial radius of the nucleus as a normalization constant in Eq. 3. Note that there is no memory of the previously taken direction. The NC-CC axis is, again, taken as a reference after each 15 min. and depending on the distance of the nucleus from the cell cortex, $\Delta\theta$ is calculated, and eventually, a new angle is again chosen randomly from within the bounds. Note that the cell does not exactly follow the NC-CC axis for cell migration due to the intracellular dynamics and fluctuations in the cell.

Analysis: We measure the average speed of the center of mass of the cell while it is in the channel. This cell speed average is then averaged over approximately 1000 realizations for each channel width. We also measure the persistence in the motility as defined as the ratio of the path length of the center of mass of the cell divided by the length of the channel. Flux is defined as the fraction of cells that exit the channel on the side different from the entry side. The circularity of the nucleus C is defined as $C = \frac{4\pi A}{P^2}$, where A is the area of the cell and P is its perimeter. When $C = 1$, the nucleus is a circle. The time-averaged energy of the cell is calculated by taking the ensemble average of energy contributions from the conservative potentials. The initial cell energy for the conservative potentials is zero.

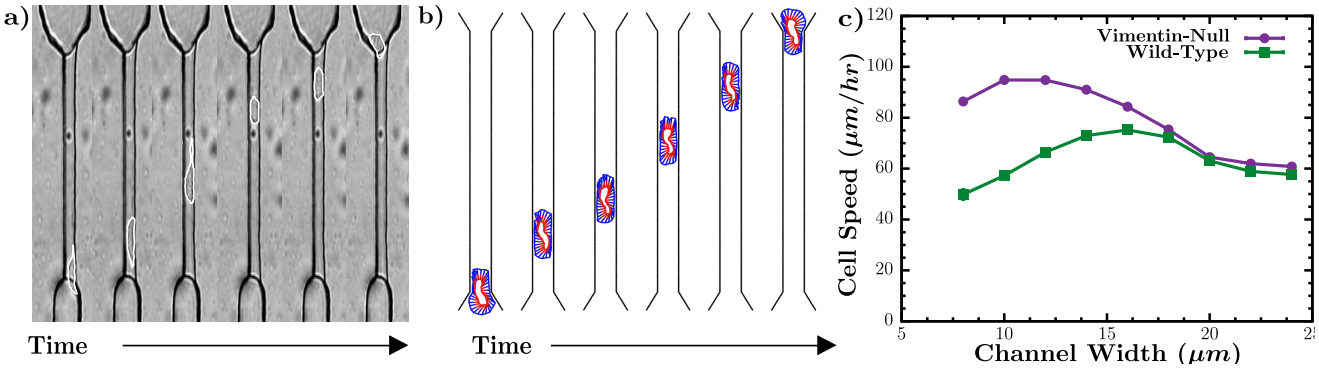

Figure 38 : *Model quantitatively agrees with cell speeds from micro-channel experiments*: (a) Time series of a wild-type mEF cell moving in a microchannel (b) Same as (a) but images are from a computational model. (c) Average cell speed as a function of channel width for wild-type and vimentin-null cells for the computational model.

4.2 Results

4.2.1 Simulations

We model the cell as containing an outer actomyosin cortex, represented by monomers connected by springs, a cell nucleus, also represented by monomers connected by springs, and bulk cytoskeletal filaments—including vimentin, represented as linker springs connecting the two inner and outer cortices. See Fig. 37(c). There is an energetic cost to changing the area of both cortices as well to capture the incompressibility of the cells. The cell also interacts with each wall of the microchannel composed of fixed monomers via an adhesive potential. To study the motility of the cell through the microchannel, there is an active force, $\mathbf{F_a}$ on the half of the acto-myosin cortex monomers in a direction initially towards the opening of the microchannel. Should any actomyosin cortex monomer come within some proximity of the wall, there is an additional force, $\mathbf{F_w}$, exerts on an actomyosin cortex monomer in the direction of the leading edge. The direction of the leading edge is chosen uniformly at random within some range of angle. We propose a form for the range of possible leading edges that depends on the magnitude of the difference between the center of the mass of the cell and the center of mass of the nucleus, with the position of the nucleus serving as a readout for the position of the centrosome. The forces in the model are updated using over-damped dynamics. For a detailed explanation motivating each force in the model, please see the Model section above. See Figs. 38a and 38b for

snapshots of the experiments and the simulations of a cell moving through a microchannel. Two supplementary movies generated with Visual Molecular Dynamics (VMD) [206] have also been provided.

4.2.2 Cell speed is non-monotonic with confinement and affected by vimentin

Strikingly, we observe for both cell types that as the channel width decreases, the average cell speed is non-monotonic (Fig. 38c). This trend has also been observed in experiments [207]. How does such a trend emerge? As the channels become narrower, the cell's cortex increases its contact with the wall. This increase in contact generates more driving force to increase cell speed. However, this trend is competing with the deformability of the cell. As the channel width becomes even narrower, the linker springs become more deformed (more compressed) and so these springs act to increase the effective adhesion to the wall given that unbinding to the wall is driven by a distance threshold. This increased adhesion time leads to a slower cell speed. Thus, the non-monotonic trend emerges from these competing factors, contact with the wall increasing the driving force and increasing the adhesion time as the cells become increasingly more deformed. We can modulate this competition by either increasing the driving force or the adhesion strength. If one increases the driving force, either by increasing the active force or the wall force, not only will the maximum speed increase, the peak will broaden towards smaller channel widths (Fig. 42). If one decreases the adhesion strength, a similar effect occurs (Fig. 43).

How is such a trend modified in vimentin-null cells? Since the presence of vimentin makes cell stiffer [208, 209, 188, 68], the vimentin-null cell line is described by a decreased linker spring strength and a decreased nucleus area spring strength, with the latter capturing the lack of a vimentin cage around the nucleus. We indeed observe a similar non-monotonic trend, but with a larger average cell speed as compared to wild-type cells, at least for narrower channel widths. Moreover, the maximum average cell speed occurs at a narrow channel width. Again, as confinement increases, the bulk cytoskeleton in both cell lines also starts deforming (compressing). However, the wild-type cell provides more resistance as it is a stiffer cell, and, thus, pushes against the walls more to effectively

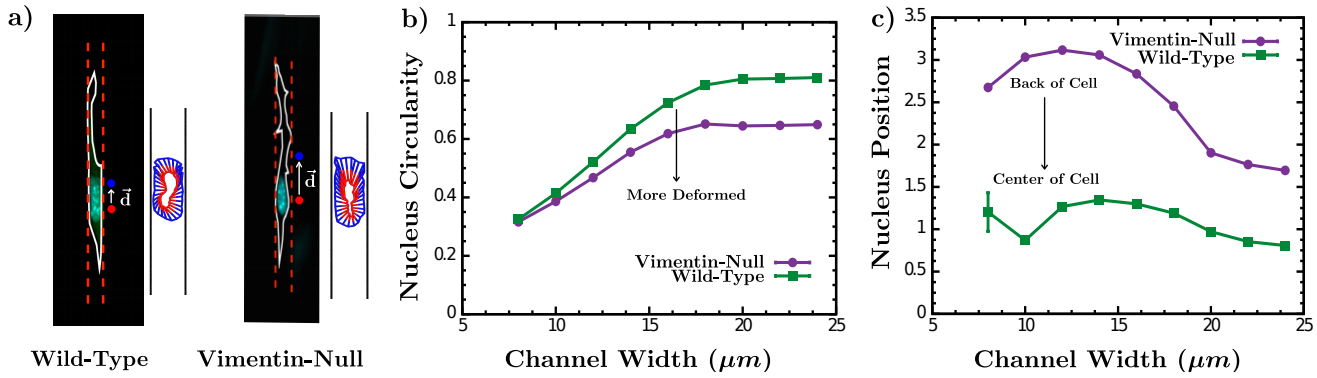

Figure 39 : *Vimentin affects nuclear shape and position.* (a) Images of a wild-type mEF cell and a vimentin-null mEF cell moving in a microchannel and their computational counterparts. In addition, the vector difference between the cell center of mass and the nucleus center of mass, $\boldsymbol{d}$, is labeled on each cell image. (b) The circularity of the cell nucleus as a function of confinement for both cell types. (c) The position of the center of mass of the cell nucleus with respect to the center of mass of the cell as a function of channel width for both cell types.

act a stronger adhesion to the wall. This effective adhesion to the wall is weaker for the vimentin-null cell line because linker spring strength is weaker. This effect results in both a larger maximum average cell speed and the driving force out-competing the adhesion for a larger range of change of channel widths. Note that our results also depend on the nucleus area spring strength. Decreasing the nucleus area spring strength also decreases the effective adhesion to the wall, as the anchoring of the springs to the nucleus is less stiff and so also enhances the average cell speed (Fig. 44).

Now let us compare the computational model with the experiments. Our average cell speed is in reasonable quantitative agreement with the experimental cell speed measurements for both cell types and for two different channel widths (Fig. 38(c)) with wild-type cells moving more slowly than vimentin-null cells in the microchannels channels [68]. This outcome is in stark contrast with two-dimensional cell motility studies [66].The experiments demonstrate that as confinement increases, vimentin-deficient cell's average speed also increases, whereas wild-type cell speed remains largely unchanged [68]. We find similar behavior with the non-monotonic trend in cell speed as a function of channel width weaker in the wild-type case. This non-monotonicity also agrees with the experimental observations of other cell lines migrating in the channels [207]. For vimentin-null cells, we predict that for channels less than a 10-micron width that the cell speed will begin to decrease. Hints of this prediction are evident in transwell experiments [187].

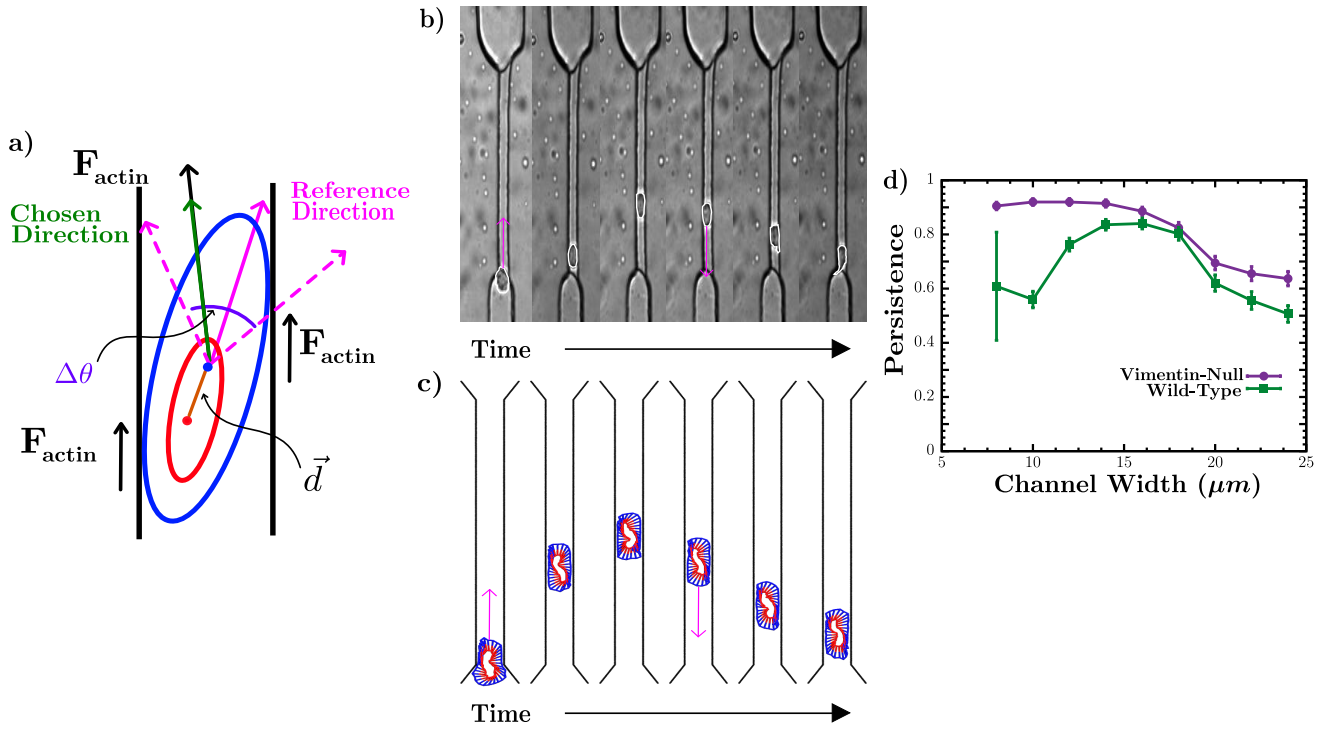

Figure 40 : *Nucleus-centrosome-based polarity mechanism.* (a) Schematic of the polarity mechanism. (b) Time series of a cell moving into the channel and changing direction. For experimental methods, please see [68] (c) Computational example of a cell changing direction in the channel. (d) Persistence as a function of channel width for both cell types.

4.2.3 Vimentin's dual role of stress transmitter and nuclear protector

Since the linker spring strength mediates the transmission of forces between the actin cortex and the nuclear cortex, one, therefore, may anticipate the shape of the nucleus to depend on the linker spring strength. For instance, we expect the nucleus shape to be less correlated with the cell cortex shape as the linker spring strength becomes weaker. Prior experiments indeed indicate that the shape of the nucleus is affected by vimentin as cells move in confinement [210]. To quantify effects of the linker spring strength on nuclear shape, we calculate nuclear circularity C, which is defined as $\frac{4\pi * \mathrm{A}}{\mathrm{P}^2}$, where A denotes the cross-sectional area of the nucleus and P its cross-sectional perimeter (Figs. 39(a) and (b)). When C = 1, the nuclear cross-section is a circle. As the channel width decreases, nuclear circularity decreases for both cell types, however, the nuclei of the vimentin-null cells are typically more deformed than their wild-type counterparts. The greater decrease in C for the wild-type cells with increasing confinement is due to the larger stresses mediated by the bulk cytoskeleton, thereby potentially motivating the need for a mesh-like vimentin

cage around the nucleus to help mediate them.

Interestingly, experiments indicate that the nucleus in vimentin-null cells have more wrinkles than wild-type and has less effective volume [211]. As discussed in the simulation subsection, in addition to modifying the linker spring strength to go from one cell type to the other, we also modify the area spring constant for the nucleus, with the latter accounting for the mesh-like vimentin cage surrounding the nucleus. When we increase the area spring constant for the nucleus, as well as increase the linker spring stiffness, we find that even though the cytoskeleton still transfers forces from outside to the nucleus with increasing confinement, the nucleus resists such deformations with the circularity tracking very similarly for the smaller channel widths between the two cell types.

The nuclear envelope is typically viewed as dominated by the nuclear laminas [212]. Here we suggest that vimentin around the nucleus also has a role in stabilizing the shape of the nucleus. Thus, we can conclude that vimentin protects the nucleus from deformations as well as mediates stress transmission between the two cortices, the actin one and the nuclear one [213, 214]. Now we have quantitative modeling results to substantiate this concept.

Since nuclear positioning is important for cell migration, we next compute the center of mass of the nucleus, the center of mass of the cell, and determined the distance between the two, defined as the magnitude of $\boldsymbol{d}$ with the origin of $\boldsymbol{d}$ at the center of mass of the nucleus as shown in Figs. 39(a) and 38(c). This metric estimates the location of the nucleus with respect to the rest of the cell. When $|\boldsymbol{d}| \approx 1$, the nucleus is closer to the center of the cell as compared to the vimentin-null case. For larger $|\boldsymbol{d}|$, the nucleus moves toward the rear of the cell or away from the leading edge of the cell. We find that the nuclei in the vimentin-null cells are typically positioned toward the rear of the cell, while the nuclei for the wild-type cells are closer to the center of the cell (Fig. 39(c)). As the channel width narrows, this difference becomes even starker.

How does this trend of nuclear positioning emerge? For the more malleable linker springs, springs in the leading half of the cell more readily attach to the wall creating a typically flatter leading edge for the part of the cell cortex not attached to the walls.

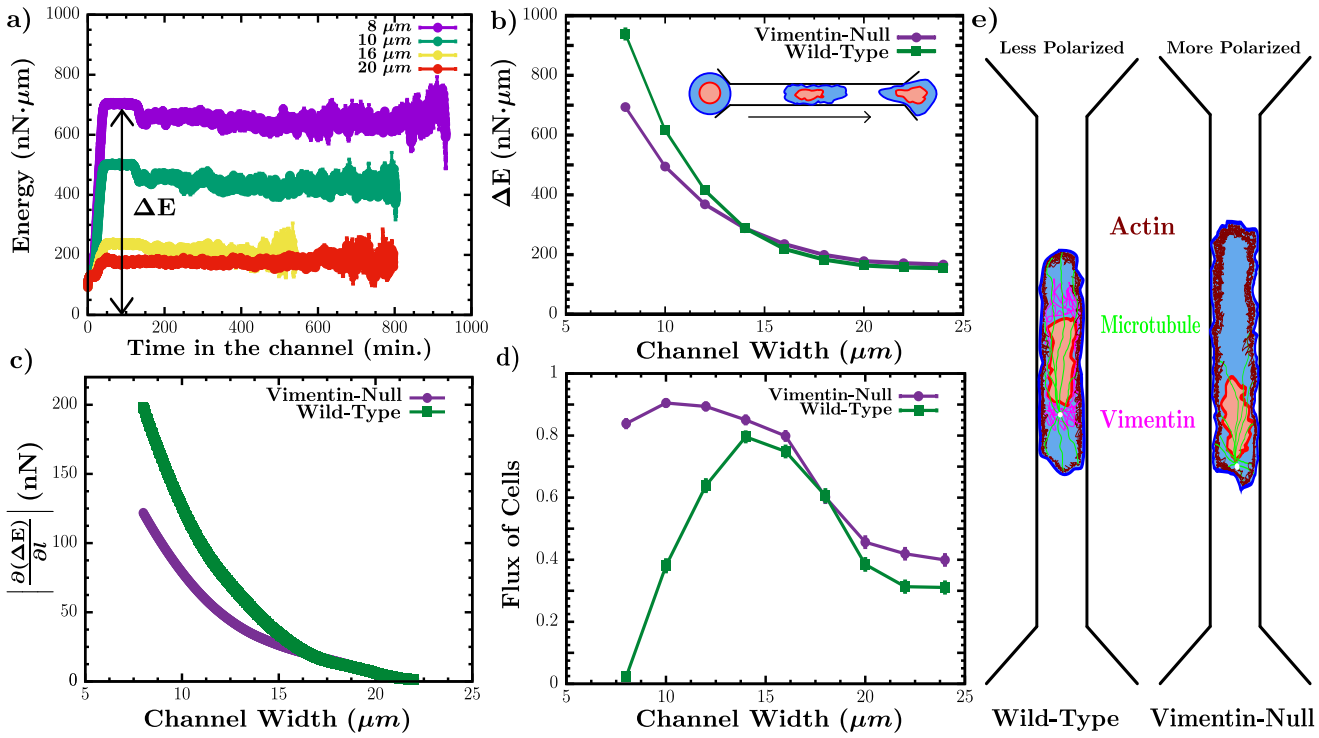

Figure 41 : *Energy barriers in confined cell motility.* (a) The average energy of each cell due to the conservative forces as a function of time for different channel widths. (b) The time-averaged energy as a function of channel width for both cell types. (c) The magnitude of the numerical derivative of the time-averaged energy, which is proportional to the stress on the cell due to the channel, as a function of channel width for both cell types. (d) The flux of each cell type as a function of the channel width. (e) A schematic of the internal organization of more polarized/persistent cells versus less polarized/persistent ones with the centrosome denoted by the white circle.

The linker springs in the leading half of the cell associated with the leading edge are, therefore, more extended (see Fig. 39(a)). From an energetic point-of-view, the extra tension (stretching) in the leading half of the cell is compensated for by the springs in the rear half of the cells configuring to be close to their rest length. This argument also tells us that the nucleus is being pulled by the leading half of the cell as it moves through the channel. We confirm this by calculating the forces on the nucleus due to the cortex (Fig. 45).

4.2.4 Loss of vimentin increases cell persistence in micro-channels

Based on the observed changes in nuclear positioning, we propose a novel polarity mechanism based on the position of the nucleus, which is a readout for the position of the centrosome in the cell. The centrosome plays an important role in cell polarity and

is also connected to the nucleus via various crosslinkers and proteins [215]. We assume that such connections between the centrosome and nucleus remain strong as the cells move through the channel and so the position of the nucleus tracks the position of the centrosome. We posit in confinement that as the magnitude of d increases, the cell becomes more polarized with the possible range of angles of microtubule polymerization scaling as $|\Delta\theta| = \frac{\pi}{2}\left(1 - \frac{|\boldsymbol{d}|}{R_{Nuc}}\right)$, where R_{Nuc} is the rest radius of the nucleus and $\pm\Delta\theta$ is defined clockwise/counter-clockwise from the reference angle of $\boldsymbol{d}$ respectively (Fig. 40(a)). There are two reasons for this scaling. First, as the nucleus is more displaced, only the longest microtubules polymerize towards the leading edge of the cell. The lateral confinement and rear end of the cell disrupt microtubule polymerization in the remaining directions. This spatial arrangement biases microtubule polymerization parallel to the confining walls [216, 217]. See Supplementary Fig. 46 for the distribution of angles possible for the leading edge of the cell (with respect to the x-axis) and the distribution of angles chosen by the cell.

In Figs. 40(b) and (c), we show the time series for a wild-type cell from the earlier micro-channel experiment and compare it with our computational model. As in the experiments, we find that the wild-type cells are more likely to change direction in the channel. To quantify this, we measure the contour length of the trajectory normalized by the length of the micro-channel such that a persistence of unity occurs when the cell does not change direction in the channel. We find that the vimentin-null cell line is more persistent in the channels as compared to the wild-type for all channel widths but more notably different for the smaller channel widths (Fig. 40(d)). We have also studied the persistence as a function of k_L, k_{Nuc}^{Area}, F_a, F_w, and ϵ_{Ad}. See Supplementary Figs. 47, 48, 49. Given the more asymmetric nuclear positioning in the vimentin-null, a stronger F_a will enhance the tensioning in the leading half of the cell and, thus, decrease $\Delta\theta$ to enhance the polarization, for example.

In the wild-type cells, we note that persistence is initially increasing with increased confinement (Fig. 40(d)). We also see there is a decreased persistence towards the tighter channels. This behavior tracks the non-monotonic behavior observed in the magnitude

of d as a function of the channel width. To explain this non-monotonic trend, we turn to the delicate balance between the stiffness of the cell and strain due to channel width. In intermediate channel widths, the wild-type spends less time, thus, have less chance of turning to the other side. The more time wild-type cells spend in the channels, the greater the chance of moving back towards the entrance or getting stuck in the channel. In wider channels, cells do not have enough wall contact but in very narrow channels, stiffness of the cells kicks in and so the cells spend more time in the channel as they travel more slowly in terms of speed.

Indeed, our model recapitulates the experiments. More precisely, experiments found that vimentin-null mEFs were more persistent than wild-type mEFs. For example, in $10\mu m$ channels about half of the wild-type cells did not cross the channel, whereas most of the vimentin-null cells passed to the other side [68]. These results are somewhat surprising as the cells behave opposite on 2D substrates. In 2D, vimentin-deficient cells form lamellipodia in all directions thereby preventing them from polarizing, which is not as likely to occur with their wild-type counterparts.

4.2.5 Energy barriers in confined migration

It has been observed that cells tend to migrate in the direction of least confinement to minimize energetic costs [218]. To test the notion of confinement as an energetic barrier in cell motility, we compute the time-averaged energy due to conservative potentials while the cell is in the channel. See Fig. 41(a). We repeat this measurement for the different channel widths. See Fig. 41(b). For the two cell lines, the average energy increases more for the wild-type cells than for the vimentin-null cells as the confinement increases, as anticipated.

However, the increase in energy is non-linear. Interestingly, recent modeling studies the phenomenon of compression stiffening in cells. Compression stiffening, a nonlinear rheological property in which a material's moduli increase with increasing uniaxial compressive strain, has recently been discovered in static cells [16]. Such a phenomenon could also manifest itself in confined cell motility. We have measured the compressive strain in

the cells and find a good correlation between compressive strain and channel width (Fig. 50). Since the derivative of the energy with respect to strain, or channel width, relates to the compressive stress of the cell, should a quantity proportional to the compressive stress increase faster than linear with the decreasing channel width, then the motile cells are indeed exhibiting compression stiffening. We find this to be the case. See. Fig. 41(c). Since the vimentin-null are more deformable, their compression stiffen is less dramatic and the onset occurs at a slightly higher strain.

In addition to the energetic barrier, there is also a time scale for entering (versus crossing) the channel translates into a rate for attempting to hop over the energy barrier. This attempt rate depends on the polarization of the cell. Prior to entering the channel, the cell effectively sees a two-dimensional surface. In this case, the magnitude of $\boldsymbol{d}$ is smaller for both cell types, so that we anticipate more changes in cell direction for both cell types. Since we initialize the cells to move towards the channel opening, we do not explore the attempt rate here.

The non-linear increase in the energy barrier as confinement increases accounts for the dramatic drop in the flux, or the fraction of the cells exiting out the other side, as a function of channel width for the wild-type cells. For those narrow channels, the wild-type cells are not able to enter the channel in the first place while for the vimentin-null, they are, and hence the dramatic drop in flux for the smaller channel widths (Fig. 41(d)). Such behavior agrees with experimental observations.

4.3 Discussion

To focus on vimentin's role in confined cell motility, we use a computational model that captures the roles of *all three types of cytoskeletal filaments as well as the cell nucleus*. We investigate the potential dual role of vimentin: the first being the mechanical protector of the nucleus and the second being a stress regulator between the cell cortex and the cell nucleus. For the first role, we modify the stiffness of the nucleus, and for the second, we modify the stiffness of the mechanical connections, or linker springs, between the inner and outer cortices. For the wild-type cells, we find a nonmonotonic dependence of cell

speed with channel width. As the channel width narrows, the cell's cortex increases its contact with the wall, which, in turn, generates more driving force to increase cell speed. Yet, this trend competes with the bulk deformability of the cell via the linker springs and nucleus to increase the effective adhesion as the channel width decreases, leading to a slower cell speed. For the vimentin-null cells, we observe a similar non-monotonic trend, but with a larger cell speed. Moreover, the maximum cell speed occurs at a narrow channel width, as compared to wild-type cells, given the enhanced bulk deformability of the cells. Thus, for nondeformable confinement with simple geometry, vimentin-null cell speed is typically faster, which is seemingly contrary to the notion that the EMT cells typically upregulate vimentin to be able to move more efficiently.

And yet, there is another ingredient to cell motility beyond the speed, which is cell direction, or cell polarity. Our results demonstrate that vimentin-null cells are more polarized in confining microchannels. This trend emerges because the nucleus is typically located more to the rear of the cell in the vimentin-null case, which biases the orientation of the longer microtubules, thereby determining the direction of the leading edge. The enhanced polarization indicates that the vimentin-null cells are more subjugated to the confinement since their own internal polarization mechanism that depends on cross-talk of the centrosome with the nucleus and other cytoskeletal connections is diminished. In other words, the *vimentin-null cells rely more heavily on external cues*, at least in this stiff microchannel environment, and so are less autonomous. See Fig. 41(e). Finally, since energetic costs are known to be a predictor of the migration path in confined cell motility, we find a higher nonlinear energy barrier for wild-type cells entering more confined channels as compared to the vimentin-null cells, which, again, is seemingly contrary to the notion of the upregulation of vimentin enhancing cell motility, however, autonomy may supersede energetics in some cases. Moreover, restructuring of the cytoskeleton occurs on longer migration timescales to potentially alter the energy barrier.

What do our findings tell us about the interaction between a cell and its microenvironment more generally? In the absence of vimentin, the cells become more deformable and so more mechanically sensitive to their microenvironment. The downregulation of

vimentin helps the cell travel more effectively from one place to another in a confined, straight channel. However, the real tissue environment, with its interstitial spaces, is more complex. Therefore, for a cell to upregulate vimentin in order to enhance motility translates to a cell enhancing its own internal polarization mechanism to effectively search the microenvironment for a minimal energy barrier by being able to more readily able to change direction. In other words, the cell is less enslaved to the "whims" of the microenvironment and so more autonomous. The cells upregulate vimentin despite the potential increase in a confinement energy barrier because they have developed coping mechanisms, such as Arp2/3 branched actin around the cell nucleus helping it to squeeze through small pores [219]. Such effects are not currently accounted for in the model. Additionally, with the upregulation of vimentin, there is more mechanical cross-talk between the two cortices to perhaps increase the role of the nucleus itself in regulating cell mechanics. Recent work suggests that compressed nuclei release calcium into the cytoplasm to help reconfigure the cytoskeleton [220]. Therefore, our theoretical findings provide a much richer interpretation of how vimentin affects cell migration with the combination of stress coupler between inner and outer parts of the cell, nuclear protector, and now polarity regulator.

How does our model compare with other models of confined cell motility? Active gel models of the cells predict that cells repel their way through confined spaces much like a climber repelling off a wall [178]. Such a model does not explicitly include a nucleus nor a centrosome such that cell polarity is an input. Another model based on the molecular-clutch mechanism explores glial cells moving through microchannels [221]. Cell polarity is, again, an input. A third model with the complexity of an actomyosin cortex and a nucleus and couplings in between demonstrates that there is a nonmonotonic relationship between cell speed and matrix stiffness in two-dimensions [222]. Cell confinement in this model is explored by constraining the beads/nodes to stay within a channel geometry. The cell direction of motion is randomly chosen every so many minutes. While cell speed is studied, cell persistence is not. Here, cell polarization emerges from an intra-cellular detail rooted in the position of the centrosome assumed to be in close proximity with the nucleus. There are indeed additional models, notably, Refs. [223, 224]. Our model walks the fine

line between being minimal and yet detailed enough to quantify the new functionality of vimentin. In terms of comparison with two-dimensional cell motility models [179], we anticipate that the polarizability of the cell changes from our new mechanism to one that depends on the fluctuations in d, as opposed to the average. Moreover, we anticipate the fluctuations in d being larger in the vimentin-null case, which corresponds to more possible directions in the cells.

While we have focused on comparison with mEFs, we expect our findings to generalize to other mesenchymal cell types. Specifically, another cell type would presumably translate to a different set of parameters. Since our findings are robust for a range of several parameters, we expect our conclusions to generalize to other cell types. Given the paradigm of the EMT, we aim to test our predictions on cell types that do undergo an EMT transition while also accounting for the typical downregulation of keratin. Since we have focused here on mesenchymal cells, it would be interesting to generalize our model to include lamins in non-mesenchymal cells and explore the role of vimentin in other motility modes of migration [225]. It would also be interesting to alter the geometry of the microchannel as well as study multiple cells moving in confinement to determine the robustness of our findings. Extending our polarization mechanism to include multicellular interactions will shed more light on the phenomenon of contact inhibition of locomotion in which motile cells stop moving or change direction upon contact with another cell.

4.4 Supplementary Figures and Movies

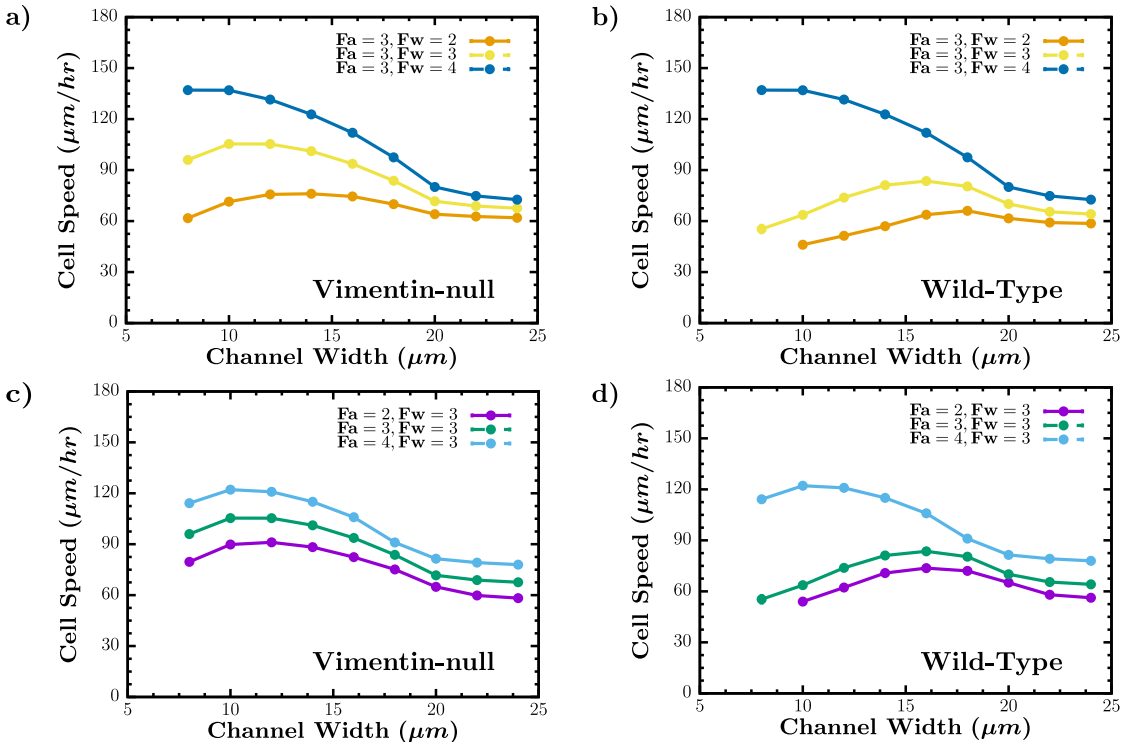

Figure 42 : *Cell speed as a function of channel width for different actin forces at the leading edge and actin forces at the wall.'* In (a) and (b), the magnitude of the actin force at the leading edge F_a is fixed and the magnitude of the actin force at the wall F_w is varied for each cell type and as a function of channel width. In (c) and (d), the magnitude of the actin force at the leading edge is now varied.

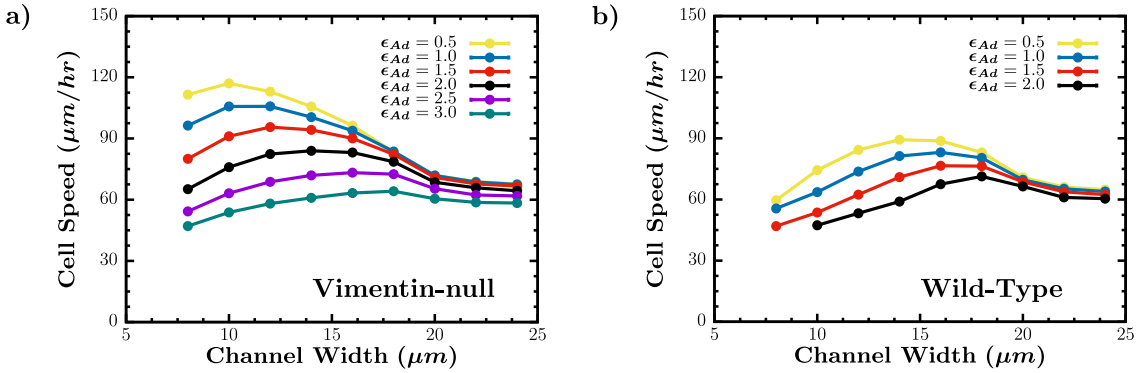

Figure 43 : *Cell speed as a function of channel width for different adhesion strengths.* (a) Vimentin-null cell (b) Wild-type cell.

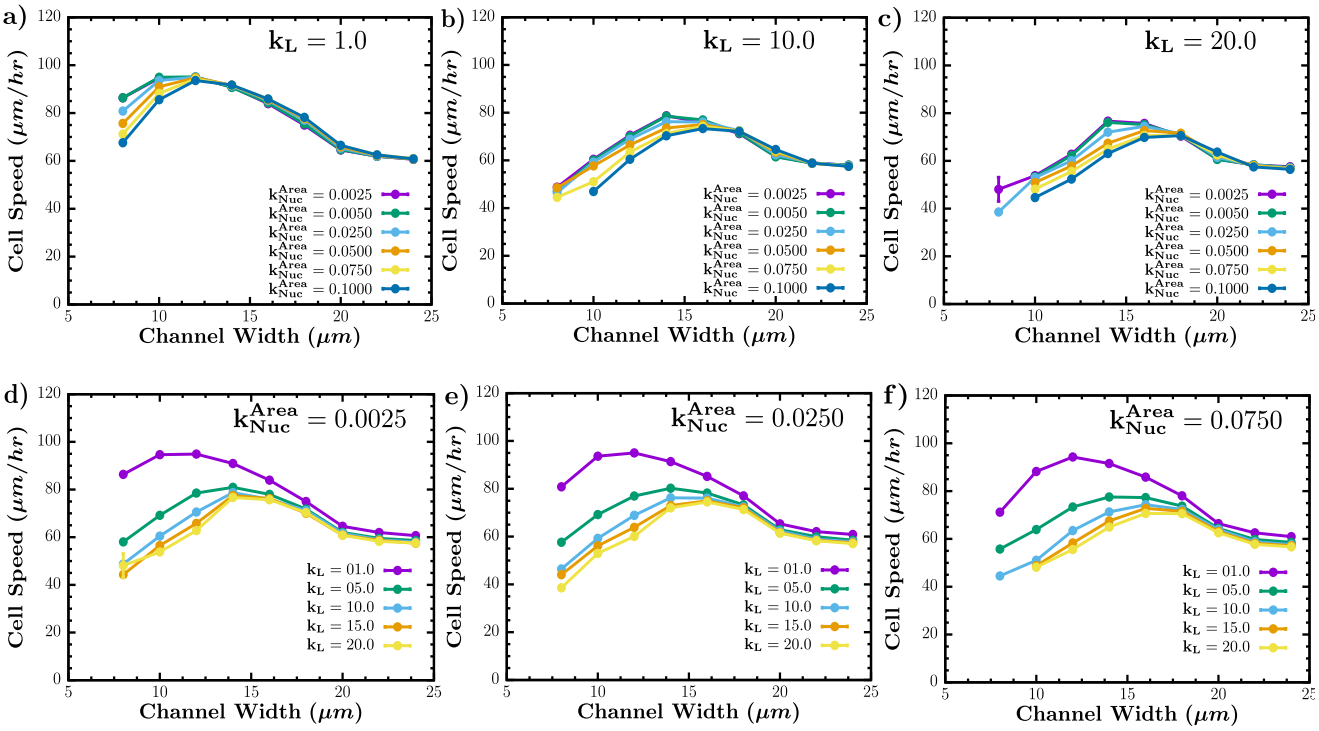

Figure 44 : *Cell Speed as a function of channel width for different linker and nuclear area spring strengths:* (a)-(c) Varying nuclear area spring strength K^{area}_{nuc} for different linker spring strengths, K_L. (d)-(f) Varying linker spring strengths, K_L, for different nuclear area spring strengths K^{area}_{nuc}.

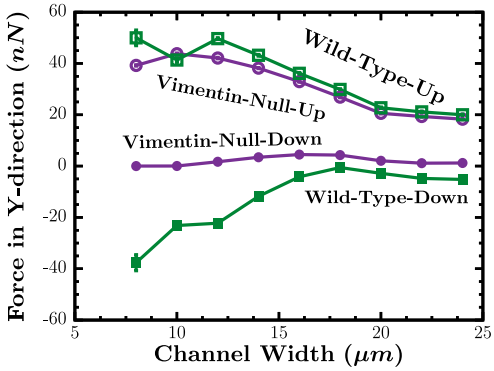

Figure 45 : *Forces on the nucleus due to the actomyosin cortex:* The net force in the y-direction on the top (upper) half of the nucleus due to the leading half of the actomyosin cortex and the net force in the y-direction on the bottom (lower) half of the nucleus due to the rear half of the actomyosin cortex as a function of channel width for each cell type.

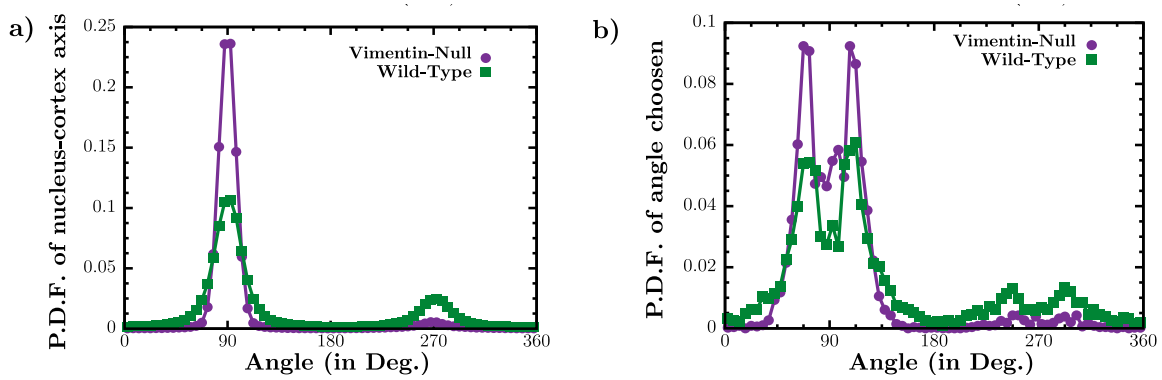

Figure 46 : *Angular information.*(a) Probability distribution function of the angle between x-axis and the Nucleus-axis for both cell types. (b) Probability distribution function of the angle choosen by the cell (with respect to the x-axis) for a 10 μm channel width.

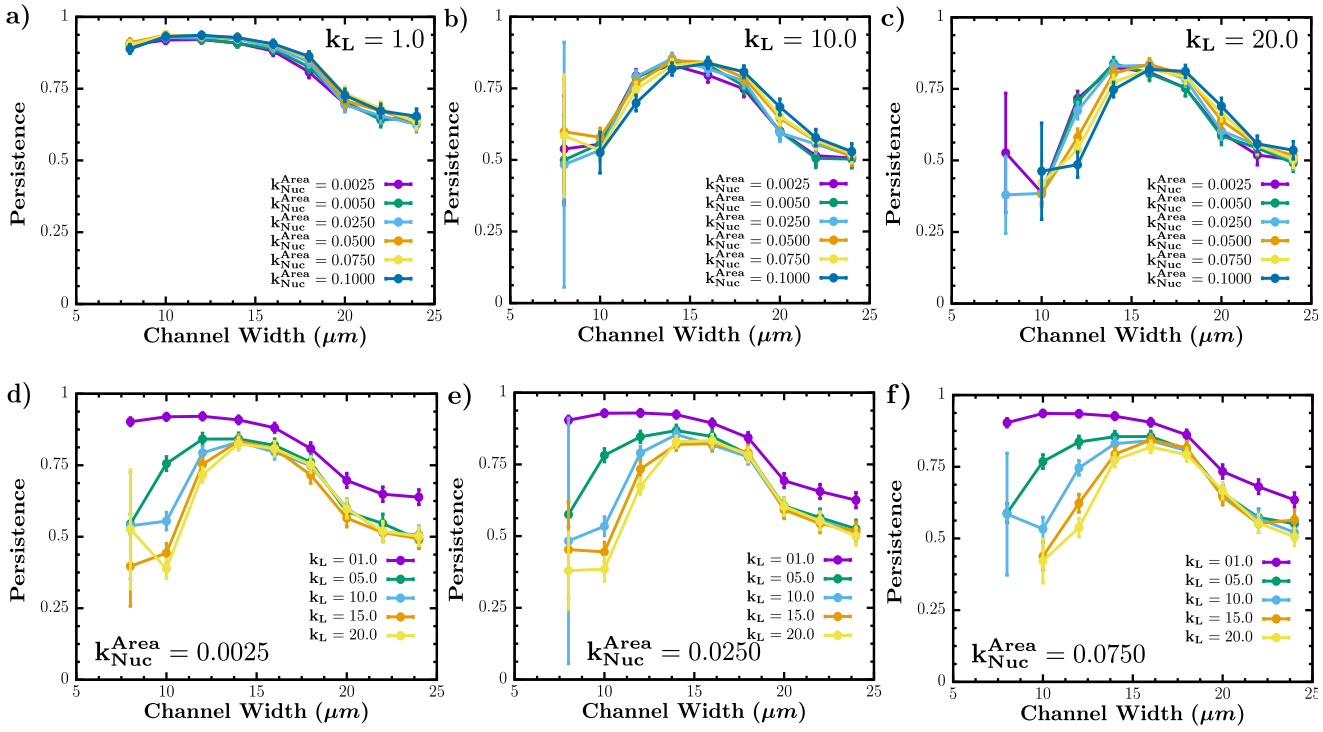

Figure 47 : *Persistence as a function of channel width for different linker and nuclear area spring strengths*: (a)-(c) Varying nuclear area spring strength K_{nuc}^{area} for different linker spring strengths, K_L. (d)-(f) Varying linker spring strengths, K_L, for different nuclear area spring strengths K_{nuc}^{area}.

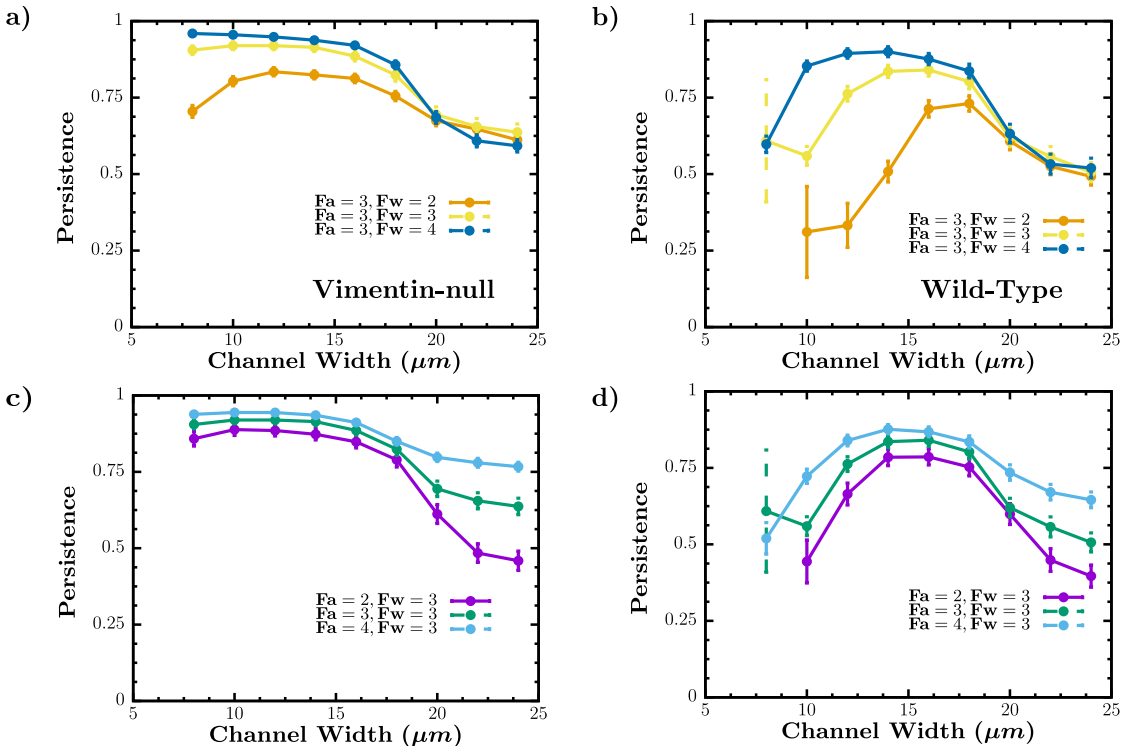

Figure 48 : *Persistence as a function of channel width for different actin forces at the leading edge and actin forces at the wall.'* In (a) and (b), the magnitude of the actin force at the leading edge F_a is fixed and the magnitude of the actin force at the wall F_w is varied for each cell type and as a function of channel width. In (c) and (d), the magnitude of the actin force at the leading edge is now varied.

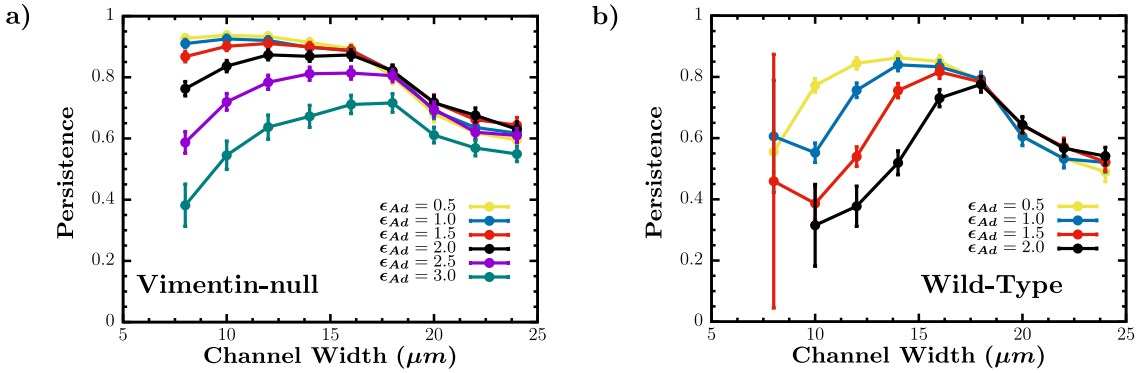

Figure 49 : *Persistence as a function of channel width for different adhesion strengths.* (a) Vimentin-null cell (b) Wild-type cell.

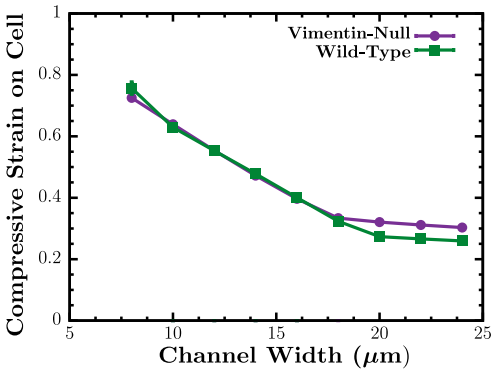

Figure 50 : *Strain on cell.* Compressive strain on the cell versus channel width for both cell types.

Chapter 5

Modeling uniaxial compression of tissues

Tumor growth remains a formidable challenge in medical science, as tumors can become metastatic, spreading to various locations within our bodies [226]. Even after surgical removal, tumors may recur due to their ability to proliferate uncontrollably. Tumor formation initiates when a cell undergoes uncontrolled division, displacing surrounding healthy cells and tissues. To tackle this issue effectively, it is crucial to understand the tumor growth and, more specifically, explore the physical factors that drive tumor cells to leave the primary tumor site and migrate, ultimately forming tumors in other body regions. Such understanding holds the potential to pave the way for developing clinical therapies to combat tumors effectively.

Tumor growth often occurs in constrained environments, where the increased pressure may prompt cells to leave the tumor site. Recent experimental investigations have focused on compressing both malignant and healthy tissues to serve as proxies for tumor growth. The findings from these experiments demonstrate that cells within malignant MDA-MB-231 spheroids exhibit greater motility and invasiveness, leading to them leaving the tumor compared to cells within non-tumorigenic MCF10A spheroids [227]. Moreover, the study of tissue behavior can also provide valuable insights into fibrosis. Experimental work has revealed that different compression stiffening behaviors are exhibited in normal, early-stage, and established lung fibrosis when assessing the shear storage modulus G' under uniaxial stress [228]. Additionally, another study has highlighted that glioma tissue in the brain experiences more pronounced stiffening under compression compared to normal brain tissue. This finding suggests that the function of glial cells could be influenced by local tissue stiffness, and stiffness changes within brain tumors may arise due to pressure gradients originating from within the tumors themselves [229].

We draw inspiration from these experimental findings, and we set out to understand tissue behavior under compression and the conditions under which cells might become invasive using a computational model. To achieve this, we used a three-dimensional vertex model, initially proposed by Okuda and Co. [76]. However, we adopted the publicly available code base provided by Prof. Zhang and our research group [70]. By changing only one parameter, we explore two distinct tissue types under compression: a solid-like tissue

and a fluid-like tissue. Remarkably, by modifying a single parameter in the simulation that controls the mechanical state of the tissue, we could observe significant differences in tissue behavior, closely resembling the experimental observations of malignant and healthy tissues.

5.1 Simulation model and methods

Although the two-dimensional vertex model is well-established for explaining various phenomena in tissue mechanics, such as cell mixing and the transition from solid to fluid behavior, in organisms like Drosophila and Hydra [71, 72, 73, 74, 75], we used three-dimensional vertex model that let us explore more degree of freedom and is closer to real-world systems. Our three-dimensional version represents cells as polyhedra composed of vertices, edges, and faces; vertices make the edges that form faces, which makes the polyhedra [76, 70]. In our model, the periodic box simulation consisted of 591 cells, as depicted in Fig. 52a. Like the two-dimensional model, our three-dimensional model also adheres to the confluent tissue condition, ensuring no gaps between cells within the simulation.

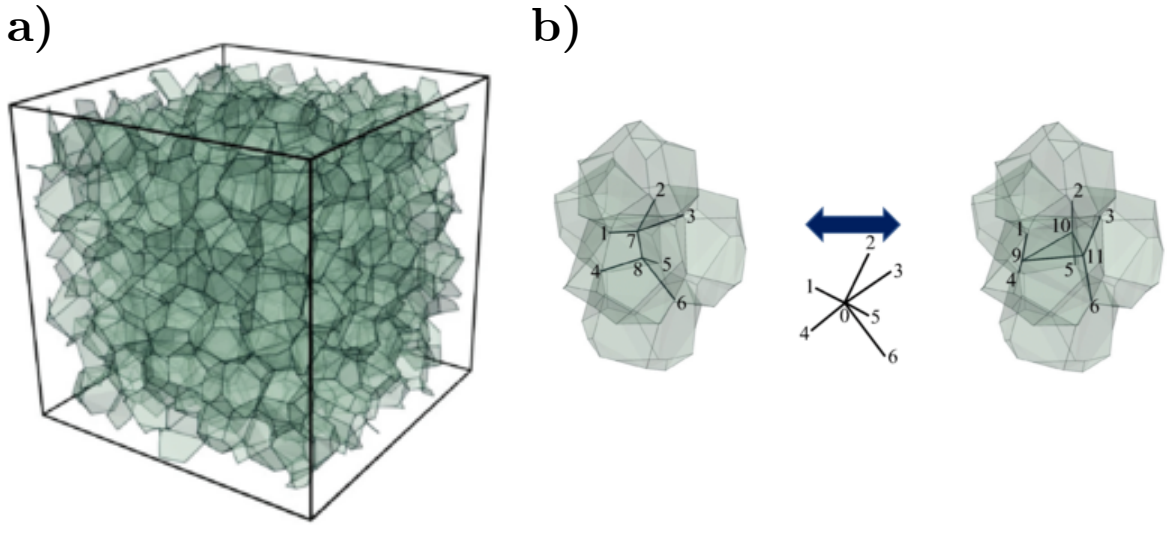

Figure 51 : *Three-dimensional vertex model:* a) Each polygon represents a cell which has volume and surface area conservation to maintain the integrity of a cell b) In three dimensions, cells can change neighbors through face-to-line or vice-versa transition [70].

The energy functional for each cell, expressed as equation 5.1, incorporates several

essential parameters. Firstly, k_V represents the volume stiffness, characterizing the internal stiffness of the cell, and V_i denotes the volume of the ith cell. The first term in the equation, a square term, acts as a volume spring that ensures the cell's volume remains close to the equilibrium value, V_o, which is determined by the volume stiffness k_V. Additionally, the next term in the energy functional is the area spring term, denoted by K_A, representing the cell's surface area stiffness. The variable A_i represents the surface area of the ith cell, while A_o signifies the desired surface area of that specific cell. In the context of the physical properties, the volume terms relate to the bulk elasticity of the cell, with V_o serving as the target volume.

$$E = \sum_i [k_V(V_i - V_o)^2 + k_A(A_i - A_o)^2] \tag{5.1}$$

The area term for cell j can be expressed as $K_A {A_i}^2 + \Gamma A_i + const$, where $\Gamma = -2K_A A_o$. The first term, $K_A {A_i}^2$, corresponds to the contractility of the actomyosin cortex, while the second term, ΓA_i, represents an interfacial tension Γ. This tension is determined by a competition between cell-cell adhesion at negative Γ (resulting in larger A_o) and cortical contractility at positive Γ (resulting in smaller A_o). Thus, the target area A_o is crucial in determining whether cell-cell adhesion or cortical tension dominates the system. Any length l can be normalized using $l = V_o^{1/3}$ to achieve dimensionless results. Furthermore, another critical parameter we utilize to differentiate between different tissue types is the cell shape index, defined as $s0 = A_o/(V_o)^{2/3}$.

In a three-dimensional vertex model to determine how cells exchange neighbors through reconnection events, we adopt the approach introduced by Okuda and his team [76]. Specifically, we focus on edges and triangles during the reconnection process, as shown in Fig. 51b. To determine if a reconnection event is possible, we search for edges with lengths smaller than a threshold value l_{th} and triangles with all three edge lengths below l_{th} as shown in Fig. 51 b. If such edges or triangles are found, we randomly select one of them and proceed with an edge-to-triangle reconnection event, where the edge disappears, and a triangle with its normal vector parallel to the initial edge takes its place, as shown in Fig. 51 b. To go the other way, we can select a triangle and perform a triangle-to-edge

reconnection event if certain conditions, as introduced in the work of Okuda and his team [76], are met to ensure the physical plausibility of the reconnection.

The first condition is that the change in energy before and after the reconnection event should be of the order of l_{th}. The second condition is related to resolving topological irreversibility and is subject to the following sub-conditions: (1) two edges should not share two vertices simultaneously, two polygonal faces should not share two or more edges simultaneously, and two polyhedral cells should not share two or more polygonal faces simultaneously. It ensures a consistent topology throughout the reconnection process. The third sub-condition, though not explicitly discussed in the work of Okuda and his team, is implemented for computational efficiency. Following these criteria, we can reliably determine the feasibility of reconnection events during our simulations.

In the molecular dynamics simulation, after every ten-time steps, reconnection events are identified for edges and triangles that satisfy the specified conditions. These eligible edges and triangles are tagged for potential reconnection. The reconnection events are then executed sequentially, starting with the edge-to-triangle reconnections, followed by the triangle-to-edge reconnections. During this process, some initially tagged edges and triangles may become untagged as reconnections take place. However, only edges and triangles that were previously tagged are removed from the list, and no new elements are added to the tagged list.

$$\dot{\mathbf{r}}_\mathbf{i} = \mu_\mathbf{i}\mathbf{F}_\mathbf{i} + \mu_\mathbf{i}\mathbf{F}_\mathbf{i}^\mathbf{B} \tag{5.2}$$

The system's dynamics follow Brownian dynamics, described by eq. 5.2 for the ith vertex. In this equation, r_i represents the position of the ith vertex, and F_i is the total conservative force acting on the ith vertex, derived from the energy function in eq. 5.1, which takes contributions from both the area and volume terms. Additionally, F_i^B accounts for the random thermal force acting on the ith vertex, and the mobility parameter μ is set to 1. To integrate the equation, we utilize the Euler-Maruyama method. The specific parameter values used for the simulation are provided in the table.

To define each cell's vertices, edges, and faces, we use a three-dimensional Voronoi

tessellation to finalize [230], where initially randomized points are generated in a box and assumed to be cell centers with periodic boundary conditions applied. Instead of computing the partial derivatives $\mathbf{F}_i = \nabla_i E$ of the energy E with respect to the positions of each vertex due to its computational efficiency, we used another approach described as follows. To compute the forces acting on each vertex based on the energetic contributions in Eq. 5.1, we divided down each polygonal face with four or more edges, depending on the number of edges on the polygon, into radially arranged triangles. Each triangle is made up of one polygonal edge, and the edges form by joining the center point of the polygonal face to the polygonal vertices [76]. Next, we calculate the pressure of each cell resulting from the volume term and the tension of each triangular face due to the area term in Eq. 5.1. These values are used to determine the forces acting on each triangular face by multiplying the pressure with the surface area and the tension with the edge length. These forces are then redistributed to the vertices forming each face. Once the forces are computed, we update the positions of the vertices using Eq. 5.2, which includes a random thermal force $\mathbf{F}_i^B$. The simulation timestep is denoted as $d\tau$. Before collecting data for the plots presented in the results section, the system is equilibrated for a duration of $\Delta t = 500$.

To compress the tissue, we employed non-periodic boundary conditions in the top and bottom directions while maintaining periodic boundaries in the x and y directions. Uniaxial compression was achieved by applying a force on the top and bottom vertices, directing them toward the center of the tissue. The cell shape index was utilized to quantitatively assess the tissue's behavior under compression.

Diffusion constant	D	1
Thermal energy	k_BT	10^{-4}
Simulation timestep	$\mathrm{d}\tau$	0.005
Cell area stiffness	K_A	1
Cell volume stiffness	K_V	10
Cell target volume	V_o	1
Cell target shape index	$s0$	5.0/5.8
Reconnection event threshold edge length	l_{th}	0.2
Mobility	μ	1
Maximum strain	ϵ_l	30%

Table 4 : Table of parameters used in the simulation. All values are in simulation units

5.2 Results

5.2.1 Soild-like tissue are more frustated than fluid-like tissue under compression

In our simulations, we focus on two mechanically distinct tissues controlled by the cell shape index. Previous study shows that at $s0 = 5.0$, the tissue behaves like a solid-like tissue, and $s0 = 5.8$, the tissues behave like a fluid-like tissue. Since we would like to understand the behavior of the tumor under compression, we choose these two far-away values of the cell shape index to cover both tissue types.

Under normal conditions without compression, solid-like tissues do not achieve their target shape, but cells in fluid-like tissue achieve their target shape. We observed similar behaviors under copresssion as well but with enhanced behavior. Fig 52 presents a time series of the simulation movie, illustrating the response of solid-like tissue under uniaxial compression. We noticed that the cells responded to compression by undergoing

reconnection events and eventually achieved a relatively flat morphology, aided by periodic boundary conditions acting in the x and y directions.

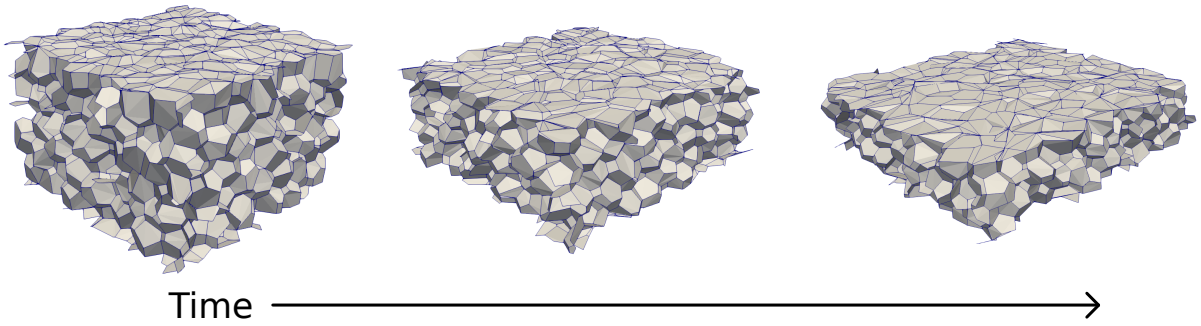

Figure 52 : *Time series snapshots of parallel plates uniaxially compression the vertex model of tissue*

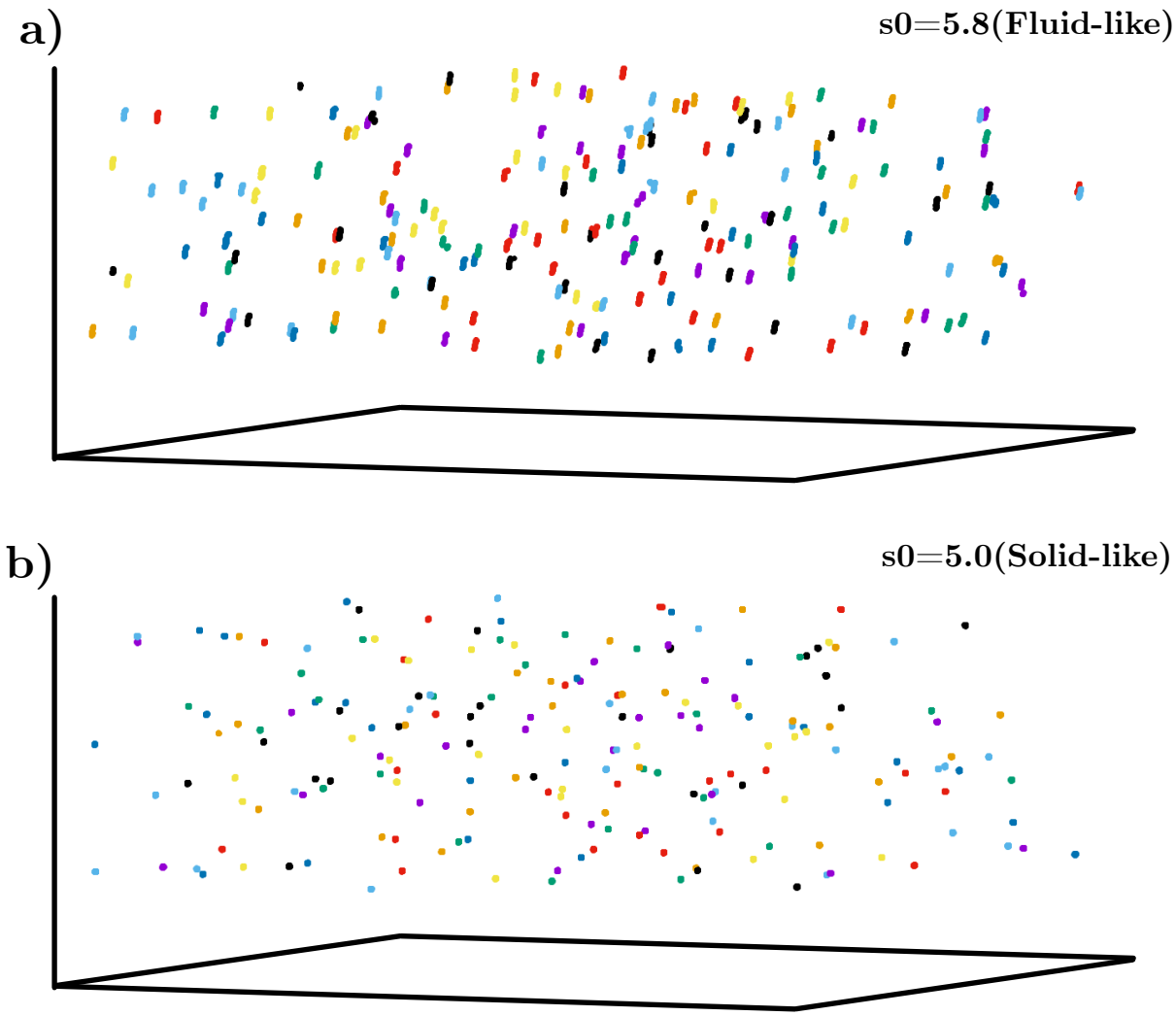

Figure 53 : *Cell trajectory in two tissue types:* a) Cells show more motile behavior in fluid-tissue tissue than in b) cells in solid-like tissue.

To visualize their behavior further, we plotted the trajectory of both tissue types as shown in Fig 53 a (fluid-like) and b (solid-like). We are showing only a few cell trajectories from the tissue for clarity. We observe that the fluid-like tissue displays more overall displacement compared to solid-like tissue, which highlights that the cells in fluid-like tissue are still relatively moving more under compression than the solid-like tissue.

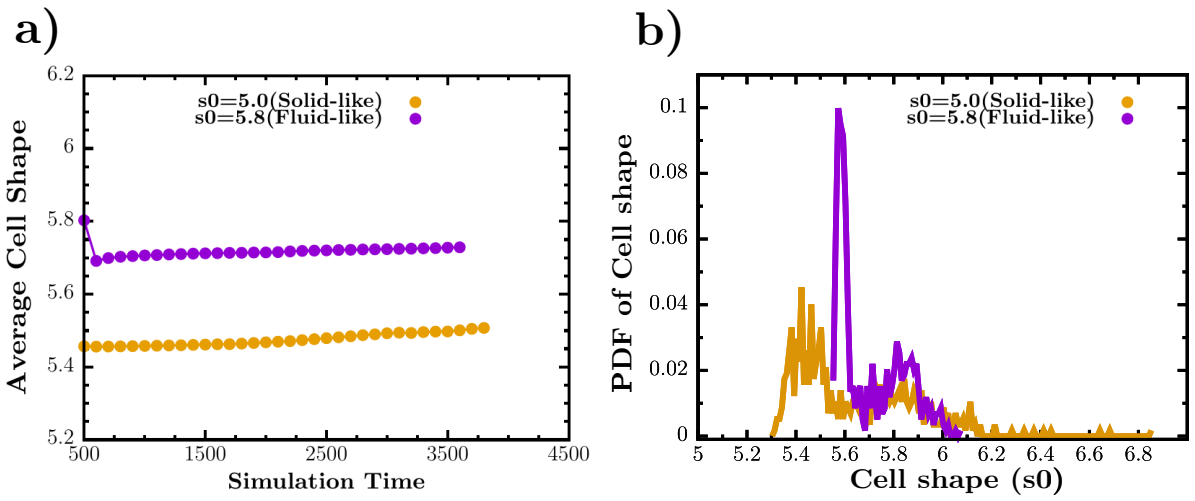

Figure 54 : *Quantification of cell behavior in the tissue under uniaxial compression:* a) Average cell shape with time shows that cells are closer to their target shape in the fluid-like tissue than in solid-like tissue. b) cell shape distribution for cells in both tissue types shows that most cells in fluid-like tissue are closer to their target shape than in solid-like tissue.

To gain further insights into the behavior of cells in the two tissue types, we analyzed the average cell shape index over time, as presented in Fig 54a. Notably, neither tissue type could attain its target cell shape on average during the simulation period. For the solid-like tissue, the observed cell shape index was measured at $s = 5.45$, a significant distance from its target cell shape index of $s_i = 5.0$, which closely resembled its behavior in the uncompressed state. Conversely, the fluid-like tissue, known to achieve its target shape of $s_i = 5.8$ in the uncompressed condition, stabilized around $s = 5.7$ under compression. This observation indicates that cells in the fluid-like tissue are close to reaching their desired shape index but have not achieved it yet. Interestingly, despite being relatively closer to their target shape compared to solid-like tissue, cells in the fluid-like tissue also experienced a state of frustration, preventing them from fully achieving their target shape. These findings unveil the distinct mechanical characteristics of the two tissue types under

compression. The solid-like tissue struggles considerably to reach its desired shape, while even the fluid-like tissue, though closer, faces challenges in attaining its target shape. These findings provide insights into the mechanical responses of different tissue types under compression and highlight the complexity of tissue behavior in such conditions.

Furthermore, to delve deeper into the contrasting cell behavior between the two tissue types, we examined the distribution of the cell shape index for the last simulation frame after compression. Notably, for the fluid-like tissue, we observed that a significant proportion of cells were close to their target shape, with a peak observed cell shape index at $s = 5.6$. Additionally, there was a secondary peak at the target shape $s0 = 5.8$, and even some cells exhibited a higher shape index. This indicates that the cells in the fluid-like tissue possess the ability to change their neighboring cells with the help of reconnection events to achieve their desired target shape. On the other hand, the solid-like tissue displayed a different distribution, with cells not being close to their target cell shape value of $s = 5.0$. The peak of observed cell shape for solid-like cells was at $s = 5.5$, and the distribution extended to higher cell shape indices, indicating a lack of convergence to the target shape. These observations highlight that the cells in the solid-like tissue are unable to effectively change their neighboring cells to reach their target shape, which sets them apart from the fluid-like cells in terms of mechanical behavior.

The observed behavior can potentially be explained by the differing mechanical properties of the cells in solid-like and fluid-like tissues. Cells in the solid-like tissue are more rigid, which means that most edge lengths do not meet the length threshold required for reconnection events. Similarly, they are less likely to undergo triangle-to-edge reconnection events. As a result, these cells face challenges in changing their neighboring cells and are thus unable to achieve their target shape effectively. In contrast, cells in the fluid-like tissue are more deformable and responsive to thermal noise. This increased deformability allows for a higher number of reconnection events, which in turn facilitates the relaxation of the system. Consequently, the cells in the fluid-like tissue are better able to adapt their shape and have a greater likelihood of reaching their target shape due to their increased ability to change neighboring cells.

5.3 Conclusions and Discussions

In this study, we expanded the computational three-dimensional vertex model to investigate how cells behave when tissues undergo uniaxial compression. We used compression to model the growth experienced by real-world tumors, which encounter pressure from their surrounding environment, including neighboring healthy tissues and the extracellular matrix, during uncontrolled growth. Our findings revealed distinct behaviors of cells in fluid-like and solid-like tissues. Specifically, cells in the fluid-like tissue exhibited higher motility and were closer to their target cell shape. In contrast, cells in the solid-like tissue were more frustrated and unable to achieve their desired shape. These observations hold implications for understanding the physical conditions that emerge in a tumor before a tumor cell decides to leave. Our work indicates that the fluid-like tissue may more closely resemble malignant tumors, where cells are more likely to metastasize and spread to other parts of the body. On the other hand, the solid-like tissue bears similarities to benign tumors. Overall, our study sheds light on the mechanical dynamics of tumor tissues under compression and provides valuable insights into the possible behavior of tumor cells before they metastasize.

This work is currently ongoing, and for our next steps, we aim to conduct a more detailed investigation of individual cell behavior in both fluid-like and solid-like tissues. To achieve this, we will analyze the overlap index and mean square displacement of cells and compare our results with existing experimental data. This analysis will help us gain deeper insights into the mechanical properties of these tissues and how they respond to compression. Furthermore, we are interested in exploring whether the transition point from solid-like to fluid-like behavior changes for tissues under compression. Understanding this transition point and its underlying mechanisms will be crucial in deciphering how tissues adapt and respond to external mechanical forces.

Chapter 6

Discussions and conclusions

In this thesis, we studied the two and three-dimensional computational models of living systems, which give new insights into how mechanics plays an important role at multiple scales of biological systems, from viruses at the nanometer scale to nuclei and cells at the micrometer scale, all the way up to tissues at the millimeter range.

We began with investigating the interaction between viruses and cell surface coreceptors, focusing on the process of viral uptake. We identified an optimal density of cell surface filaments that resulted in the most efficient viral uptake. Additionally, we observed that cell surface bending rigidity played a critical role in the wrapping process: low rigidity led to crumpling-like wrapping, while high rigidity resulted in fold-like wrapping. We found that fold-like wrapping was not only faster but also more efficient in terms of utilizing the cell surface. However, achieving fold-like wrapping was not only a function of the optimal filament density. We also discovered the importance of optimal stretching strength for folding. Without the appropriate stretching strength, even with an optimal filament density, we observed crumpling-like wrapping instead of faster and efficient fold-like wrapping. Thus, filament density and stretching strength are crucial to achieving efficient viral uptake through fold-like wrapping.

For the next steps, there are several exciting directions to explore in this work. For instance, while we assumed that the virus is tethered to the cell surface via the primary receptor, understanding how the virus locates the primary receptor amidst a forest of coreceptors remains a compelling question. Investigating the virus's search strategy to find the primary receptors could provide valuable insights into virus-cell mechanics. Moreover, our current study focused on single viruses interacting with the cell surface, but in reality, multiple viruses could attach simultaneously. Exploring how virus-virus interactions shape viral uptake efficiency and influence cell surface morphology presents an exciting avenue for further investigation.

In the next part of the thesis, we explored the physical mechanisms contributing to the formation of abnormal nuclear shapes due to chromatin dynamics. We reproduced various nuclear shape aberrations from experimental studies, ranging from round nuclei to those with bulges and wrinkles. To distinguish between different bulges, we develop an

algorithm that identifies the bulge boundaries and quantifies their lifetimes. Interestingly, cell nuclei with more crosslinkers exhibited more stable bulges when coupled with higher chromatin activity. However, increasing the number of stable motors did not lead to more bulges, as the finite surface area of the nucleus limited bulge formation. Nonetheless, when we combined stable motors with a higher number of crosslinkers, we found that the stability of the bulge increased. Furthermore, our investigation revealed that internal chromatin dynamics play a significant role in explaining these observations at the nuclear surface level. As chromatin activity, crosslinkers, and motor stability increased, so did the chromatin correlation length, representing the extent to which different parts of chromatin moved together. These factors also contributed to an increase in the number and stability of bulges. Thus, we concluded that the motion of chromatin correlation was the driving force behind bulge formation on the nuclear surface.

In our investigation of the nucleus material properties, we performed compression simulations to understand its behavior under different strain rates. We observed that the nucleus responded differently depending on the applied strain rate. At high-strain rates, the lower half of the nuclei exhibited relatively fewer changes in shape, while at slow-strain rates, the nucleus displayed a more elongated shape, which closely resembled experimental observations. This finding suggests that the speed at which the compression is applied influences the deformation of the nucleus. Furthermore, we identified the viscoelastic behavior of the nucleus, where the force required to achieve the same strain level varied significantly with different strain rates. This implies that the nucleus exhibits viscoelastic characteristics, with its response to compression depending on the rate at which the force is applied.

Given the complexity of nuclear internal structures, we plan to explore the role of nuclear actin and nucleosomes. Additionally, we aim to investigate how the nucleus interacts with the dynamic environment outside, including cytoskeletal elements. Understanding the nuclear surface behavior between two active regions will shed light on how internal and external interactions could influence the formation of abnormal nuclear shapes. In nuclear compression work, next, we would like to understand the influence of motors on

the nucleus's morphology under compression and how the nucleus relaxation time scale changes with varying strain rates. This research direction will provide valuable insights into how chromatin behavior alters during cell migration in confined environments. By studying the response of the nucleus to compression, we can gain a deeper understanding of its mechanical properties and role in cellular processes.

In the following chapter, we investigated how the absence of one of the intermediate filament vimentin affects cell motility and polarity in confined environments. Our findings revealed that vimentin-null cells exhibit higher speeds in confinement, as the absence of vimentin makes both the nucleus and cytoskeleton weaker, allowing for easier compression. In contrast, wild-type cells, with vimentin providing rigidity to the nucleus and cytoskeleton, move slower in confinement, despite generating similar polymerization forces. Additionally, we discovered that vimentin plays a protective role for the nucleus during movement in confined spaces. Our novel polarity model demonstrated that vimentin-null cells exhibit higher polarity than wild-type cells, as the centrosome's movement is restricted in the absence of vimentin, leading to more persistent cell directions.

For future investigations, we plan to explore the influence of flexible walls on cell motility and polarity, as biological confinements are not as rigid as microchannels. Moreover, we aim to study our model in other confined environments, such as spherical or T-shape channels. It would be interesting to understand how multiple cells interact within the modeling framework, providing confinement for each other. These future steps will provide further insights into how cellular components and structures contribute to cell behavior in confined spaces.

In the final chapter, we focused on tissue compression to gain insights into the mechanical behavior of tumors. Our results demonstrated that solid and fluid-like tissues exhibit distinct responses under compression. Solid-type tissues experience more frustration, as they are limited in their ability to achieve the desired cell shape due to their limited ability to change neighboring cells. On the other hand, fluid-type tissues are more deformable, allowing them to change their neighboring cells more efficiently. The work is still ongoing, and our next step involves examining the individual cell behavior in each tissue type under

compression. By doing so, we aim to identify the physical conditions that could lead to tumor breakup. Understanding how tumor tissues behave under compression could provide valuable information for predicting tumor growth and progression in different mechanical environments.

This thesis explores the role of mechanics in biological processes across various scales. However, these different scales work together in the real world to maintain homeostasis. In future work, I intend to integrate these individual models into a nested, interacting multi-scale model that includes both mechanical and chemical feedback. This comprehensive computational model, spanning from chromatin to tissue scales, will provide a quantitative interpretative framework to understand the vast array of experimental results. By doing so, we can gain a deeper understanding of how tissues and organs function and, ultimately, the fundamental principles governing life itself through the lens of simple physical principles.

Bibliography

[1] Robert Hooke. "Micrographia : or, Some physiological descriptions of minute bodies made by magnifying glasses. With observations and inquiries thereupon". In: *Royal Society of London* XXX (1664), p. 60. URL: http://resource.nlm.nih.gov/2366075R.

[2] Mervyn Susser and Zena Stein. "Germ Theory, Infection, and Bacteriology". In: *Eras in Epidemiology*. Evans 1993. Oxford University Press, 2009, pp. 107–122. ISBN: 9780195300666. DOI: 10.1093/acprof:oso/9780195300666.003.0010. URL: https://doi-org.libezproxy2.syr.edu/10.1093/acprof:oso/9780195300666.003.0010https://academic.oup.com/book/10733/chapter/158820423.

[3] J. R Mayer. "Über die Kräfte der Unbelebten Natur, Ann Chem Pharm". In: *Ann Chem Pharm, 42, 233-240* (1842).

[4] Gregory S. Girolami. "A Brief History of Thermodynamics, As Illustrated by Books and People". In: *Journal of Chemical and Engineering Data* 65.2 (2020), pp. 298–311. ISSN: 15205134. DOI: 10.1021/acs.jced.9b00515.

[5] California : W.A. Benjamin Menlo Park. "Bioenergetics : the molecular basis of biological energy transformations". In: *Annual Review of Biochemistry* 46.1 (1977), pp. 955–966. ISSN: 0066-4154.

[6] Teresa Rocha-Homem. "Robert Mayer: Conservation of Energy and Venous Blood Colour". In: *Advances in Historical Studies* 04.04 (2015), pp. 309–313. ISSN: 2327-0438. DOI: 10.4236/ahs.2015.44020.

[7] Erwin Schrodinger. “What is Life? The Physical Aspect of the Living Cell”. In: *Cambridge University Press* (1944).

[8] Francis Crick and James Watson. “Molecular Structure of Nucleic Acids”. In: (1953). URL: https://www.mskcc.org/teaser/1953-nature-papers-watson-crick-wilkins-franklin.pdf.

[9] Pablo Gottheil et al. “State of Cell Unjamming Correlates with Distant Metastasis in Cancer Patients”. In: *Physical Review X* 13.3 (2023), p. 031003. ISSN: 2160-3308. DOI: 10.1103/PhysRevX.13.031003. URL: https://link.aps.org/doi/10.1103/PhysRevX.13.031003.

[10] Guannan Liu et al. “Self-Driven Phase Transitions Drive Myxococcus xanthus Fruiting Body Formation”. In: *Physical Review Letters* 122.24 (2019), p. 248102. ISSN: 10797114. DOI: 10.1103/PhysRevLett.122.248102. arXiv: 1709.06012. URL: https://doi.org/10.1103/PhysRevLett.122.248102.

[11] Shradha Mishra, Aparna Baskaran, and M. Cristina Marchetti. “Fluctuations and pattern formation in self-propelled particles”. In: *Physical Review E - Statistical, Nonlinear, and Soft Matter Physics* 81.6 (2010), pp. 1–14. ISSN: 15393755. DOI: 10.1103/PhysRevE.81.061916. arXiv: 1001.3334.

[12] M. Cristina Marchetti et al. “Minimal model of active colloids highlights the role of mechanical interactions in controlling the emergent behavior of active matter”. In: *Current Opinion in Colloid and Interface Science* 21 (2016), pp. 34–43. ISSN: 18790399. DOI: 10.1016/j.cocis.2016.01.003. arXiv: 1510.00425. URL: https://doi.org/10.1016/j.cocis.2016.01.003.

[13] Clemens Bechinger et al. “Active Particles in Complex and Crowded Environments”. In: *Reviews of Modern Physics* 88.4 (2016), p. 045006. ISSN: 0034-6861. DOI: 10.1103/RevModPhys.88.045006. URL: https://link.aps.org/doi/10.1103/RevModPhys.88.045006.

[14] Nuno A. M. Araújo et al. “Steering self-organisation through confinement”. In: (2022), pp. 1–17. arXiv: 2204.10059. URL: http://arxiv.org/abs/2204.10059.

[15] Jordan L. Shivers et al. "Compression stiffening of fibrous networks with stiff inclusions". In: *Proceedings of the National Academy of Sciences of the United States of America* 117.35 (2020), pp. 21037–21044. ISSN: 10916490. DOI: 10.1073/pnas.2003037117. arXiv: 2002.07220.

[16] M. C. Gandikota et al. "Loops versus lines and the compression stiffening of cells". In: *Soft Matter* 16.18 (2020), pp. 4389–4406. ISSN: 1744-683X. DOI: 10.1039/C9SM01627A. URL: http://xlink.rsc.org/?DOI=C9SM01627A.

[17] M. C. Marchetti et al. "Hydrodynamics of soft active matter". In: *Reviews of Modern Physics* 85.3 (2013), pp. 1143–1189. ISSN: 00346861. DOI: 10.1103/RevModPhys.85.1143.

[18] M. Cristina Marchetti et al. "Minimal model of active colloids highlights the role of mechanical interactions in controlling the emergent behavior of active matter". In: *Current Opinion in Colloid and Interface Science* 21 (2016), pp. 34–43. ISSN: 18790399. DOI: 10.1016/j.cocis.2016.01.003. arXiv: 1510.00425. URL: https://doi.org/10.1016/j.cocis.2016.01.003.

[19] Sriram Ramaswamy. "The mechanics and statistics of active matter". In: *Annual Review of Condensed Matter Physics* 1 (2010), pp. 323–345. ISSN: 19475454. DOI: 10.1146/annurev-conmatphys-070909-104101. arXiv: 1004.1933.

[20] Michael E. Cates and Julien Tailleur. "Motility-induced phase separation". In: *Annual Review of Condensed Matter Physics* 6.1 (2015), pp. 219–244. ISSN: 19475462. DOI: 10.1146/annurev-conmatphys-031214-014710. arXiv: 1406.3533.

[21] Tal Einav et al. "Harnessing Avidity: Quantifying the Entropic and Energetic Effects of Linker Length and Rigidity for Multivalent Binding of Antibodies to HIV-1". In: *Cell Systems* 9.5 (2019), 466–474.e7. ISSN: 24054720. DOI: 10.1016/j.cels.2019.09.007. URL: https://doi.org/10.1016/j.cels.2019.09.007.

[22] Guadalupe Ayora-Talavera. "Sialic acid receptors: Focus on their role in influenza infection". In: *Journal of Receptor, Ligand and Channel Research* 10 (2018), pp. 1–11. ISSN: 1178699X. DOI: 10.2147/JRLCR.S140624.

[23] Michael Laue et al. “Morphometry of SARS-CoV and SARS-CoV-2 particles in ultrathin plastic sections of infected Vero cell cultures”. In: *Scientific Reports* 11.1 (2021), pp. 1–11. ISSN: 20452322. DOI: 10.1038/s41598-021-82852-7. URL: https://doi.org/10.1038/s41598-021-82852-7.

[24] J. D. Almeida; D. M. Berry; C. H. Cunningham; D. Hamre; M. S. Hofstad; L. Mallucci; K. McIntosh; and D. A. J. Tyrrell. “Virology: Coronaviruses”. In: *Nature* 220 (1968), p. 1968.

[25] David Tyrrell and Michael Fielder. “Cold Wars: The Fight Against the Common Cold”. In: *American Journal of Preventive Medicine* 26.1 (2004), pp. 93–94. ISSN: 07493797. DOI: 10.1016/j.amepre.2003.09.007.

[26] Mark Marsh and Ari Helenius. “Virus entry: Open sesame”. In: *Cell* 124.4 (2006), pp. 729–740. ISSN: 00928674. DOI: 10.1016/j.cell.2006.02.007.

[27] Yohei Yamauchi and Ari Helenius. “Virus entry at a glance”. In: *Journal of Cell Science* 126.6 (2013), pp. 1289–1295. ISSN: 00219533. DOI: 10.1242/jcs.119685.

[28] Inés Ripa et al. “Membrane Rafts: Portals for Viral Entry”. In: *Frontiers in Microbiology* 12.February (2021). ISSN: 1664-302X. DOI: 10.3389/fmicb.2021.631274. URL: https://www.frontiersin.org/articles/10.3389/fmicb.2021.631274/full.

[29] Łukasz Suprewicz et al. “Extracellular Vimentin as a Target Against SARS-CoV-2 Host Cell Invasion”. In: *Small* 18.6 (2022), pp. 1–16. ISSN: 16136829. DOI: 10.1002/smll.202105640.

[30] Razie Amraei et al. “Extracellular vimentin is an attachment factor that facilitates SARS-CoV-2 entry into human endothelial cells”. In: *Proceedings of the National Academy of Sciences* 119.6 (2022), e2113874119. ISSN: 0027-8424. URL: http://www.pnas.org/lookup/doi/10.1073/pnas.2113874119https://pnas.org/doi/full/10.1073/pnas.2113874119.

[31] Wei Hao et al. “Binding of the SARS-CoV-2 spike protein to glycans”. In: *Science Bulletin* xxxx (2021). ISSN: 20959281. DOI: 10.1016/j.scib.2021.01.010.

[32] Melissa S. Maginnis. "Virus–Receptor Interactions: The Key to Cellular Invasion". In: *Journal of Molecular Biology* 430.17 (2018), pp. 2590–2611. ISSN: 00222836. DOI: 10.1016/j.jmb.2018.06.024. URL: https://doi.org/10.1016/j.jmb.2018.06.024https://linkinghub.elsevier.com/retrieve/pii/S0022283618306302.

[33] Beata Turoňová et al. "In situ structural analysis of SARS-CoV-2 spike reveals flexibility mediated by three hinges". In: *Science (New York, N.Y.)* 370.6513 (2020), pp. 203–208. ISSN: 10959203. DOI: 10.1126/science.abd5223.

[34] Sarthak Gupta et al. "How cells wrap around virus-like particles using extracellular filamentous protein structures". In: (2023). arXiv: 2301.08776. URL: http://arxiv.org/abs/2301.08776.

[35] Irene Ramos et al. "Vimentin as a multifaceted player and potential therapeutic target in viral infections". In: *International Journal of Molecular Sciences* 21.13 (2020), pp. 1–27. ISSN: 14220067. DOI: 10.3390/ijms21134675.

[36] Lin Liu et al. "Heparan Sulfate Proteoglycans as Attachment Factor for SARS-CoV-2". In: *ACS Central Science* 7.6 (2021), pp. 1009–1018. ISSN: 23747951. DOI: 10.1021/acscentsci.1c00010.

[37] Ludovico Cantuti-Castelvetri et al. "Neuropilin-1 facilitates SARS-CoV-2 cell entry and infectivity". In: *Science* 370.6518 (2020), pp. 856–860. ISSN: 0036-8075. DOI: 10.1126/science.abd2985. URL: https://www.science.org/doi/10.1126/science.abd2985.

[38] Kazuya Shirato, Miyuki Kawase, and Shutoku Matsuyama. "Wild-type human coronaviruses prefer cell-surface TMPRSS2 to endosomal cathepsins for cell entry". In: *Virology* 517.September 2017 (2018), pp. 9–15. ISSN: 10960341. DOI: 10.1016/j.virol.2017.11.012. URL: https://doi.org/10.1016/j.virol.2017.11.012.

[39] Kazuhiro Maeshima, Satoru Ide, and Michael Babokhov. "Dynamic chromatin organization without the 30-nm fiber". In: *Current Opinion in Cell Biology* 58.30 (2019), pp. 95–104. ISSN: 18790410. DOI: 10.1016/j.ceb.2019.02.003. URL: https://doi.org/10.1016/j.ceb.2019.02.003.

[40] Jyotsana J. Parmar, Maxime Woringer, and Christophe Zimmer. "How the Genome Folds: The Biophysics of Four-Dimensional Chromatin Organization". In: *Annual Review of Biophysics* 48 (2019), pp. 231–253. ISSN: 19361238. DOI: 10.1146/annurev-biophys-052118-115638.

[41] Takeshi Shimi et al. "The A- and B-type nuclear lamin networks: Microdomains involved in chromatin organization and transcription". In: *Genes and Development* 22.24 (2008), pp. 3409–3421. ISSN: 08909369. DOI: 10.1101/gad.1735208.

[42] Nishit Srivastava et al. "Nuclear fragility, blaming the blebs". In: *Current Opinion in Cell Biology* 70.Figure 1 (2021), pp. 100–108. ISSN: 09550674. DOI: 10.1016/j.ceb.2021.01.007. URL: https://doi.org/10.1016/j.ceb.2021.01.007https://linkinghub.elsevier.com/retrieve/pii/S0955067421000077.

[43] Andrew D. Stephens et al. "Chromatin histone modifications and rigidity affect nuclear morphology independent of lamins". In: *Molecular Biology of the Cell* 29.2 (2018), pp. 220–233. ISSN: 19394586. DOI: 10.1091/mbc.E17-06-0410.

[44] Brian D. Cosgrove et al. "Nuclear envelope wrinkling predicts mesenchymal progenitor cell mechano-response in 2D and 3D microenvironments". In: *Biomaterials* 270.May 2020 (2021), p. 120662. ISSN: 18785905. DOI: 10.1016/j.biomaterials.2021.120662. URL: https://doi.org/10.1016/j.biomaterials.2021.120662.

[45] Michele M. Nava et al. "Heterochromatin-Driven Nuclear Softening Protects the Genome against Mechanical Stress-Induced Damage". In: *Cell* 181.4 (2020), 800–817.e22. ISSN: 10974172. DOI: 10.1016/j.cell.2020.03.052.

[46] Maria Chiara Lionetti et al. "Chromatin and Cytoskeletal Tethering Determine Nuclear Morphology in Progerin-Expressing Cells". In: *Biophysical Journal* 118.9 (2020), pp. 2319–2332. ISSN: 00063495. DOI: 10.1016/j.bpj.2020.04.001. URL: https://doi.org/10.1016/j.bpj.2020.04.001https://linkinghub.elsevier.com/retrieve/pii/S0006349520303015.

[47] Brian T. Helfand et al. "Chromosomal regions associated with prostate cancer risk localize to lamin B-deficient microdomains and exhibit reduced gene transcription".

In: *Journal of Pathology* 226.5 (2012), pp. 735–745. ISSN: 00223417. DOI: 10.1002/path.3033.

[48] Veronika Butin-Israeli et al. "Nuclear lamin functions and disease". In: *Trends in Genetics* 28.9 (2012), pp. 464–471. ISSN: 01689525. DOI: 10.1016/j.tig.2012.06.001. URL: http://dx.doi.org/10.1016/j.tig.2012.06.001.

[49] Wen Chen Liang et al. "TMEM43 mutations in emery-dreifuss muscular dystrophy-related myopathy". In: *Annals of Neurology* 69.6 (2011), pp. 1005–1013. ISSN: 03645134. DOI: 10.1002/ana.22338.

[50] Amy R. Strom et al. "Hp1α is a chromatin crosslinker that controls nuclear and mitotic chromosome mechanics". In: *eLife* 10 (2021), pp. 1–30. ISSN: 2050084X. DOI: 10.7554/eLife.63972.

[51] Joel C. Eissenberg and Sarah Cr Elgin. "The HP1 protein family: Getting a grip on chromatin". In: *Current Opinion in Genetics and Development* 10.2 (2000), pp. 204–210. ISSN: 0959437X. DOI: 10.1016/S0959-437X(00)00058-7.

[52] Lars Guelen et al. "Domain organization of human chromosomes revealed by mapping of nuclear lamina interactions". In: *Nature* 453.7197 (2008), pp. 948–951. ISSN: 14764687. DOI: 10.1038/nature06947.

[53] Yosef Gruenbaum et al. "The nuclear lamina comes of age". In: *Nature Reviews Molecular Cell Biology* 6.1 (2005), pp. 21–31. ISSN: 14710072. DOI: 10.1038/nrm1550.

[54] Joanna M. Bridger and Ian R. Kill. "Aging of Hutchinson-Gilford progeria syndrome fibroblasts is characterised by hyperproliferation and increased apoptosis". In: *Experimental Gerontology* 39.5 (2004), pp. 717–724. ISSN: 05315565. DOI: 10.1016/j.exger.2004.02.002.

[55] Merel Stiekema et al. "Structural and Mechanical Aberrations of the Nuclear Lamina in Disease". In: *Cells* 9.8 (2020). ISSN: 20734409. DOI: 10.3390/cells9081884.

[56] Jonathan A. Jackson et al. "Dynamics, scaling behavior, and control of nuclear wrinkling". In: (2022). arXiv: 2210.11581. URL: http://arxiv.org/abs/2210.11581.

[57] Chloe M. Funkhouser et al. "Mechanical model of blebbing in nuclear lamin meshworks". In: *Proceedings of the National Academy of Sciences of the United States of America* 110.9 (2013), pp. 3248–3253. ISSN: 00278424. DOI: 10.1073/pnas.1300215110.

[58] Isabel K Berg et al. "Transcription regulates bleb formation and stability independent of nuclear rigidity". In: *bioRxiv* (2022), p. 2022.11.14.516344. URL: http://biorxiv.org/content/early/2022/11/15/2022.11.14.516344.abstract.

[59] Cal Huang et al. "JNK phosphorylates paxillin and regulates cell migration". In: *Nature* 424.6945 (2003), pp. 219–223. ISSN: 00280836. DOI: 10.1038/nature01745.

[60] Marina Bacac and Ivan Stamenkovic. "Metastatic cancer cell". In: *Annual Review of Pathology: Mechanisms of Disease* 3 (2008), pp. 221–247. ISSN: 15534006. DOI: 10.1146/annurev.pathmechdis.3.121806.151523.

[61] Kenneth M. Yamada and Michael Sixt. "Mechanisms of 3D cell migration". In: *Nature Reviews Molecular Cell Biology* 20.12 (2019), pp. 738–752. ISSN: 14710080. DOI: 10.1038/s41580-019-0172-9. URL: http://dx.doi.org/10.1038/s41580-019-0172-9.

[62] Saima Usman et al. "Vimentin is at the heart of epithelial mesenchymal transition (Emt) mediated metastasis". In: *Cancers* 13.19 (2021), pp. 1–26. ISSN: 20726694. DOI: 10.3390/cancers13194985.

[63] Sharon Wu et al. "Upregulation of the EMT marker vimentin is associated with poor clinical outcome in acute myeloid leukemia". In: *Journal of Translational Medicine* 16.1 (2018), pp. 1–9. ISSN: 14795876. DOI: 10.1186/s12967-018-1539-y. URL: https://doi.org/10.1186/s12967-018-1539-y.

[64] Jean Paul Thiery et al. “Epithelial-Mesenchymal Transitions in Development and Disease”. In: *Cell* 139.5 (2009), pp. 871–890. ISSN: 00928674. DOI: 10.1016/j.cell.2009.11.007. URL: https://linkinghub.elsevier.com/retrieve/pii/S0092867409014196.

[65] John E. Eriksson et al. “Introducing intermediate filaments: From discovery to disease”. In: *Journal of Clinical Investigation* 119.7 (2009), pp. 1763–1771. ISSN: 15588238. DOI: 10.1172/JCI38339.

[66] Brian T. Helfand et al. “Vimentin organization modulates the formation of lamellipodia”. In: *Molecular Biology of the Cell* 22.8 (2011). Ed. by M. Bishr Omary, pp. 1274–1289. ISSN: 1059-1524. DOI: 10.1091/mbc.e10-08-0699. URL: https://www.molbiolcell.org/doi/10.1091/mbc.e10-08-0699.

[67] Maxx Swoger et al. “Vimentin Intermediate Filaments Mediate Cell Morphology on Viscoelastic Substrates”. In: *ACS Applied Bio Materials* 5.2 (2022), pp. 552–561. ISSN: 2576-6422. DOI: 10.1021/acsabm.1c01046.

[68] Alison E. Patteson et al. “Loss of Vimentin Enhances Cell Motility through Small Confining Spaces”. In: *Small* 15.50 (2019), p. 1903180. ISSN: 1613-6810. DOI: 10.1002/smll.201903180. URL: https://onlinelibrary.wiley.com/doi/abs/10.1002/smll.201903180.

[69] Sarthak Gupta, Alison E. Patteson, and J. M. Schwarz. “The role of vimentin-nuclear interactions in persistent cell motility through confined spaces”. In: *New Journal of Physics* 23.9 (2021). ISSN: 13672630. DOI: 10.1088/1367-2630/ac2550. arXiv: 2103.09207.

[70] Tao Zhang and J. M. Schwarz. “Topologically-protected interior for three-dimensional confluent cellular collectives”. In: *Physical Review Research* 4.4 (2022), pp. 1–10. ISSN: 26431564. DOI: 10.1103/PhysRevResearch.4.043148.

[71] Dapeng Bi et al. “Motility-driven glass and jamming transitions in biological tissues”. In: *Physical Review X* 6.2 (2016), pp. 1–13. ISSN: 21603308. DOI: 10.1103/PhysRevX.6.021011. arXiv: 1509.06578.

[72] Silvanus Alt, Poulami Ganguly, and Guillaume Salbreux. "Vertex models: From cell mechanics to tissue morphogenesis". In: *Philosophical Transactions of the Royal Society B: Biological Sciences* 372.1720 (2017). ISSN: 14712970. DOI: 10.1098/rstb.2015.0520.

[73] Preeti Sahu et al. "Small-scale demixing in confluent biological tissues". In: *Soft Matter* 16.13 (2020), pp. 3325–3337. ISSN: 17446848. DOI: 10.1039/c9sm01084j. arXiv: 1905.00657.

[74] D. B. Staple et al. "Mechanics and remodelling of cell packings in epithelia". In: *European Physical Journal E* 33.2 (2010), pp. 117–127. ISSN: 12928941. DOI: 10.1140/epje/i2010-10677-0.

[75] Yingzi Li et al. "Mechanisms of regulating cell topology in proliferating epithelia: Impact of division plane, mechanical forces, and cell memory". In: *PLoS ONE* 7.8 (2012). ISSN: 19326203. DOI: 10.1371/journal.pone.0043108.

[76] Satoru Okuda et al. "Reversible network reconnection model for simulating large deformation in dynamic tissue morphogenesis". In: *Biomechanics and Modeling in Mechanobiology* 12.4 (2013), pp. 627–644. ISSN: 1617-7959. DOI: 10.1007/s10237-012-0430-7. URL: http://link.springer.com/10.1007/s10237-012-0430-7.

[77] Thomas Fuhs et al. "Rigid tumours contain soft cancer cells". In: *Nature Physics* 18.12 (2022), pp. 1510–1519. ISSN: 17452481. DOI: 10.1038/s41567-022-01755-0.

[78] Tao Zhang et al. "How human-derived brain organoids are built differently from brain organoids derived of genetically-close relatives: A multi-scale hypothesis". In: (2023). arXiv: 2304.08622. URL: https://arxiv.org/abs/2304.08622v1.

[79] Robijn F. Bruinsma and William S. Klug. "Physics of viral shells". In: *Annual Review of Condensed Matter Physics* 6.1 (2015), pp. 245–268. ISSN: 19475462. DOI: 10.1146/annurev-conmatphys-031214-014325.

[80] L. E. Perotti et al. "Useful scars: Physics of the capsids of archaeal viruses". In: *Physical Review E* 94.1 (2016), pp. 1–16. ISSN: 24700053. DOI: 10.1103/PhysRevE.94.012404.

[81] Armando Stano et al. “Dense Array of Spikes on HIV-1 Virion Particles”. In: *Journal of Virology* 91.14 (2017). ISSN: 0022-538X. DOI: 10.1128/jvi.00415-17.

[82] Nicolas Moreno et al. “Hydrodynamics of spike proteins dictate a transport-affinity competition for SARS-CoV-2 and other enveloped viruses”. In: *Scientific Reports* 12.1 (2022), pp. 1–13. ISSN: 20452322. DOI: 10.1038/s41598-022-14884-6. URL: https://doi.org/10.1038/s41598-022-14884-6.

[83] Bálint Kiss et al. “Topography, Spike Dynamics, and Nanomechanics of Individual Native SARS-CoV-2 Virions”. In: *Nano Letters* (2021). ISSN: 15306992. DOI: 10.1021/acs.nanolett.0c04465.

[84] Rodrigo A. Moreira et al. “Quantitative determination of mechanical stability in the novel coronavirus spike protein”. In: *Nanoscale* 12.31 (2020), pp. 16409–16413. ISSN: 20403372. DOI: 10.1039/d0nr03969a.

[85] Yiwen Hu and Markus J. Buehler. “Comparative Analysis of Nanomechanical Features of Coronavirus Spike Proteins and Correlation with Lethality and Infection Rate”. In: *Matter* (2020), pp. 1–11. ISSN: 25902385. DOI: 10.1016/j.matt.2020.10.032. URL: https://doi.org/10.1016/j.matt.2020.10.032.

[86] Berend Jan Bosch et al. “The Coronavirus Spike Protein Is a Class I Virus Fusion Protein: Structural and Functional Characterization of the Fusion Core Complex”. In: *Journal of Virology* 77.16 (2003), pp. 8801–8811. ISSN: 0022-538X. DOI: 10.1128/jvi.77.16.8801-8811.2003.

[87] Cody B. Jackson et al. “Mechanisms of SARS-CoV-2 entry into cells”. In: *Nature Reviews Molecular Cell Biology* 23.1 (2022), pp. 3–20. ISSN: 14710080. DOI: 10.1038/s41580-021-00418-x.

[88] Joe Grove and Mark Marsh. “The cell biology of receptor-mediated virus entry”. In: *Journal of Cell Biology* 195.7 (2011), pp. 1071–1082. ISSN: 00219525. DOI: 10.1083/jcb.201108131.

[89] Jason P. Laliberte, Andrea S. Weisberg, and Bernard Moss. "The membrane fusion step of vaccinia virus entry is cooperatively mediated by multiple viral proteins and host cell components". In: *PLoS Pathogens* 7.12 (2011). ISSN: 15537366. DOI: 10.1371/journal.ppat.1002446.

[90] Zhiqiang Shen et al. "Membrane Wrapping Efficiency of Elastic Nanoparticles during Endocytosis: Size and Shape Matter". In: *ACS Nano* 13.1 (2019), pp. 215–228. ISSN: 1936-0851. DOI: 10.1021/acsnano.8b05340. URL: https://pubs.acs.org/doi/10.1021/acsnano.8b05340.

[91] Xinghua Shi et al. "Cell entry of one-dimensional nanomaterials occurs by tip recognition and rotation". In: *Nature Nanotechnology* 6.11 (2011), pp. 714–719. ISSN: 17483395. DOI: 10.1038/nnano.2011.151.

[92] Liping Chen et al. "Shape-dependent internalization kinetics of nanoparticles by membranes". In: *Soft Matter* 12.9 (2016), pp. 2632–2641. ISSN: 17446848. DOI: 10.1039/c5sm01869b.

[93] Robert Vácha, Francisco J. Martinez-Veracoechea, and Daan Frenkel. "Receptor-mediated endocytosis of nanoparticles of various shapes". In: *Nano Letters* 11.12 (2011), pp. 5391–5395. ISSN: 15306984. DOI: 10.1021/nl2030213.

[94] Joel C. Forster et al. "Exploring the Design Rules for Efficient Membrane-Reshaping Nanostructures". In: *Physical Review Letters* 125.22 (2020), pp. 1–6. ISSN: 10797114. DOI: 10.1103/PhysRevLett.125.228101.

[95] Wenpeng Cao et al. "Biomechanical characterization of SARS-CoV-2 spike RBD and human ACE2 protein-protein interaction". In: *Biophysical Journal* 120.6 (2021), pp. 1011–1019. ISSN: 15420086. DOI: 10.1016/j.bpj.2021.02.007. URL: https://doi.org/10.1016/j.bpj.2021.02.007.

[96] Jennifer E. Stencel-Baerenwald et al. "The sweet spot: Defining virus-sialic acid interactions". In: *Nature Reviews Microbiology* 12.11 (2014), pp. 739–749. ISSN: 17401534. DOI: 10.1038/nrmicro3346.

[97] Anastasia A. Chernyatina et al. “Atomic structure of the vimentin central α-helical domain and its implications for intermediate filament assembly”. In: *Proceedings of the National Academy of Sciences of the United States of America* 109.34 (2012), pp. 13620–13625. ISSN: 00278424. DOI: 10.1073/pnas.1206836109.

[98] Kenta Komura, Hirohiko Ise, and Toshihiro Akaike. “Dynamic behaviors of vimentin induced by interaction with GlcNAc molecules”. In: *Glycobiology* 22.12 (2012), pp. 1741–1759. ISSN: 09596658. DOI: 10.1093/glycob/cws118.

[99] Cheng Zeng et al. “Contact Mechanics of a Small Icosahedral Virus”. In: *Physical Review Letters* 119.3 (2017), pp. 1–6. ISSN: 10797114. DOI: 10.1103/PhysRevLett.119.038102.

[100] P. J. de Pablo and I. A. T. Schaap. “Atomic Force Microscopy of Viruses”. In: *Advances in Experimental Medicine and Biology*. Vol. 1140. 2019, pp. 159–179. ISBN: 9783030147419. DOI: 10.1007/978-3-030-14741-9_8. URL: http://link.springer.com/10.1007/978-3-030-14741-9_8.

[101] Anna V Schepers, Charlotta Lorenz, and Sarah Köster. “Tuning intermediate filament mechanics by variation of pH and ion charges”. In: *Nanoscale* 12.28 (2020), pp. 15236–15245. ISSN: 2040-3364. DOI: 10.1039/D0NR02778B. URL: http://xlink.rsc.org/?DOI=D0NR02778B.

[102] Wenpeng Cao et al. “Biomechanical characterization of SARS-CoV-2 spike RBD and human ACE2 protein-protein interaction”. In: *Biophysical Journal* 120.6 (2021), pp. 1011–1019. ISSN: 15420086. DOI: 10.1016/j.bpj.2021.02.007. URL: https://doi.org/10.1016/j.bpj.2021.02.007.

[103] Chen Bai and Arieh Warshel. “Critical Differences between the Binding Features of the Spike Proteins of SARS-CoV-2 and SARS-CoV”. In: *Journal of Physical Chemistry B* 124.28 (2020), pp. 5907–5912. ISSN: 15205207. DOI: 10.1021/acs.jpcb.0c04317.

[104] Spyros D. Georgatos, Daniel C. Weaver, and Vincent T. Marchesi. “Site specificity in vimentin-membrane interactions: Intermediate filament subunits associate with

the plasma membrane via their head domains". In: *Journal of Cell Biology* 100.6 (1985), pp. 1962–1967. ISSN: 15408140. DOI: 10.1083/jcb.100.6.1962.

[105] Qi Zhang et al. "Heparan sulfate assists SARS-CoV-2 in cell entry and can be targeted by approved drugs in vitro". In: *Cell Discovery* 6.1 (2020). ISSN: 20565968. URL: http://dx.doi.org/10.1038/s41421-020-00222-5.

[106] Sara B. Sieczkarski and Gary R. Whittaker. "Influenza Virus Can Enter and Infect Cells in the Absence of Clathrin-Mediated Endocytosis". In: *Journal of Virology* 76.20 (2002), pp. 10455–10464. ISSN: 0022-538X. DOI: 10.1128/jvi.76.20.10455-10464.2002.

[107] Andreia L. Pinto et al. "Ultrastructural insight into SARS-CoV-2 entry and budding in human airway epithelium". In: *Nature Communications* 13.1 (2022), pp. 1–14. ISSN: 20411723. DOI: 10.1038/s41467-022-29255-y.

[108] Rudolf A. Römer, Navodya S. Römer, and A. Katrine Wallis. "Flexibility and mobility of SARS-CoV-2-related protein structures". In: *Scientific Reports* 11.1 (2021), pp. 1–13. ISSN: 20452322. DOI: 10.1038/s41598-021-82849-2. URL: https://doi.org/10.1038/s41598-021-82849-2.

[109] Hangping Yao et al. "Molecular Architecture of the SARS-CoV-2 Virus". In: *Cell* 183.3 (2020), 730–738.e13. ISSN: 10974172. DOI: 10.1016/j.cell.2020.09.018. URL: https://doi.org/10.1016/j.cell.2020.09.018.

[110] Hoang Linh Nguyen et al. "Does SARS-CoV-2 bind to human ACE2 more strongly than does SARS-CoV?" In: *Journal of Physical Chemistry B* 124.34 (2020), pp. 7336–7347. ISSN: 15205207. DOI: 10.1021/acs.jpcb.0c04511.

[111] Jun Lan et al. "Structure of the SARS-CoV-2 spike receptor-binding domain bound to the ACE2 receptor". In: *Nature* 581.7807 (2020), pp. 215–220. ISSN: 14764687. DOI: 10.1038/s41586-020-2180-5. URL: http://dx.doi.org/10.1038/s41586-020-2180-5.

[112] Melissa S. Maginnis. "Virus–Receptor Interactions: The Key to Cellular Invasion". In: *Journal of Molecular Biology* 430.17 (2018), pp. 2590–2611. ISSN: 00222836. DOI: 10.1016/j.jmb.2018.06.024. URL: https://linkinghub.elsevier.com/retrieve/pii/S0022283618306302.

[113] Yuuta Imoto et al. "Dynamin is primed at endocytic sites for ultrafast endocytosis". In: *Neuron* (2022), pp. 2815–2835. ISSN: 08966273. DOI: 10.1016/j.neuron.2022.06.010.

[114] Natali L. Chanaday and Ege T. Kavalali. "Optical detection of three modes of endocytosis at hippocampal synapses". In: *eLife* 7 (2018), pp. 1–24. ISSN: 2050084X. DOI: 10.7554/eLife.36097.

[115] Alison E. Patteson et al. "Mechanical and Non-Mechanical Functions of Filamentous and Non-Filamentous Vimentin". In: *BioEssays* 42.11 (2020), p. 2000078. ISSN: 0265-9247. DOI: 10.1002/bies.202000078. URL: https://onlinelibrary.wiley.com/doi/10.1002/bies.202000078.

[116] Ahmet Riza Sahin. "2019 Novel Coronavirus (COVID-19) Outbreak: A Review of the Current Literature". In: *Eurasian Journal of Medicine and Oncology* 4.1 (2020), pp. 1–7. DOI: 10.14744/ejmo.2020.12220.

[117] Zunlong Ke et al. "Structures and distributions of SARS-CoV-2 spike proteins on intact virions". In: *Nature* 588.7838 (2020), pp. 498–502. ISSN: 0028-0836. URL: http://dx.doi.org/10.1038/s41586-020-2665-2https://www.nature.com/articles/s41586-020-2665-2.

[118] Lei Xie et al. "A Nanomechanical Study on Deciphering the Stickiness of SARS-CoV-2 on Inanimate Surfaces". In: *ACS Applied Materials and Interfaces* 12.52 (2020), pp. 58360–58368. ISSN: 19448252. DOI: 10.1021/acsami.0c16800.

[119] Daniel L. Blair and Arshad Kudrolli. "Geometry of crumpled paper". In: *Physical Review Letters* 94.16 (2005), pp. 1–4. ISSN: 00319007. DOI: 10.1103/PhysRevLett.94.166107.

[120] Evgeni Magid, Octavian Soldea, and Ehud Rivlin. "A comparison of Gaussian and mean curvature estimation methods on triangular meshes of range image data". In: *Computer Vision and Image Understanding* 107.3 (2007), pp. 139–159. ISSN: 10773142. DOI: 10.1016/j.cviu.2006.09.007.

[121] Xiaoqian Lin, Xubo Lin, and Ning Gu. "Optimization of hydrophobic nanoparticles to better target lipid rafts with molecular dynamics simulations". In: *Nanoscale* 12.6 (2020), pp. 4101–4109. ISSN: 20403372. DOI: 10.1039/c9nr09226a.

[122] Jiawei Li et al. "Why synthetic virus-like nanoparticles can achieve higher cellular uptake efficiency". In: *Nanoscale* 12.27 (2020), pp. 14911–14918. ISSN: 20403372. DOI: 10.1039/d0nr03234d.

[123] Qiang Sheng Xia, Hong Ming Ding, and Yu Qiang Ma. "Can dual-ligand targeting enhance cellular uptake of nanoparticles?" In: *Nanoscale* 9.26 (2017), pp. 8982–8989. ISSN: 20403372. DOI: 10.1039/c7nr01020f.

[124] Hong ming Ding and Yu qiang Ma. "Role of physicochemical properties of coating ligands in receptor-mediated endocytosis of nanoparticles". In: *Biomaterials* 33.23 (2012), pp. 5798–5802. ISSN: 01429612. DOI: 10.1016/j.biomaterials.2012.04.055. URL: http://dx.doi.org/10.1016/j.biomaterials.2012.04.055.

[125] Yinfeng Li et al. "Surface-structure-regulated penetration of nanoparticles across a cell membrane". In: *Nanoscale* 4.12 (2012), pp. 3768–3775. ISSN: 20403372. DOI: 10.1039/c2nr30379e.

[126] Haizhen Zhang et al. "Effect of receptor structure and length on the wrapping of a nanoparticle by a lipid membrane". In: *Materials* 7.5 (2014), pp. 3855–3866. ISSN: 19961944. DOI: 10.3390/ma7053855.

[127] Ye Li et al. "Size, geometry and mobility of protein assemblage regulate the kinetics of membrane wrapping on nanoparticles". In: *Journal of Molecular Liquids* 333 (2021). ISSN: 01677322. DOI: 10.1016/j.molliq.2021.115990.

[128] Tao Zhang et al. "On the Modeling of Endocytosis in Yeast". In: *Biophysical Journal* 108.3 (2015), pp. 508–519. ISSN: 00063495. DOI: 10.1016/j.bpj.2014.11.3481. URL: http://dx.doi.org/10.1016/j.bpj.2014.11.3481https://linkinghub.elsevier.com/retrieve/pii/S0006349514047468.

[129] Emma Colucci-Guyon et al. "Mice lacking vimentin develop and reproduce without an obvious phenotype". In: *Cell* 79.4 (1994), pp. 679–694. ISSN: 00928674. DOI: 10.1016/0092-8674(94)90553-3.

[130] Francesco Di Virgilio et al. "Extracellular ATP and P2 purinergic signalling in the tumour microenvironment". In: *Nature Reviews Cancer* 18.10 (2018), pp. 601–618. ISSN: 14741768. DOI: 10.1038/s41568-018-0037-0. URL: http://dx.doi.org/10.1038/s41568-018-0037-0.

[131] Bora Lim et al. "Inflammatory breast cancer biology: the tumour microenvironment is key". In: *Nature Reviews Cancer* 18.8 (2018), pp. 485–499. ISSN: 14741768. DOI: 10.1038/s41568-018-0010-y. URL: http://dx.doi.org/10.1038/s41568-018-0010-y.

[132] Michele De Palma, Daniela Biziato, and Tatiana V. Petrova. "Microenvironmental regulation of tumour angiogenesis". In: *Nature Reviews Cancer* 17.8 (2017), pp. 457–474. ISSN: 14741768. DOI: 10.1038/nrc.2017.51. URL: http://dx.doi.org/10.1038/nrc.2017.51.

[133] Amanda Parker et al. "How does the extracellular matrix affect the rigidity of an embedded spheroid?" In: 1 (2020). arXiv: 2006.16203. URL: http://arxiv.org/abs/2006.16203.

[134] Ludger Johannes, Christian Wunder, and Massiullah Shafaq-Zadah. "Glycolipids and Lectins in Endocytic Uptake Processes". In: *Journal of Molecular Biology* 428.24 (2016), pp. 4792–4818. ISSN: 10898638. DOI: 10.1016/j.jmb.2016.10.027. URL: http://dx.doi.org/10.1016/j.jmb.2016.10.027.

[135] Sophie Marbach, Jeana Aojie Zheng, and Miranda Holmes-Cerfon. "The nanocaterpillar's random walk: diffusion with ligand–receptor contacts". In: *Soft Matter*

18.16 (2022), pp. 3130–3146. ISSN: 1744-683X. DOI: 10.1039/D1SM01544C. URL: http://xlink.rsc.org/?DOI=D1SM01544C.

[136] Amr Abouelezz and Leonardo Almeida-Souza. "The mammalian endocytic cytoskeleton". In: *European Journal of Cell Biology* 101.2 (2022), p. 151222. ISSN: 16181298. DOI: 10.1016/j.ejcb.2022.151222. URL: https://doi.org/10.1016/j.ejcb.2022.151222.

[137] Meiyan Jin et al. "Branched actin networks are organized for asymmetric force production during clathrin-mediated endocytosis in mammalian cells". In: *Nature Communications* 13.1 (2022), p. 3578. ISSN: 2041-1723. URL: https://www.nature.com/articles/s41467-022-31207-5.

[138] Letizia Lanzetti, Pier Paolo Di Fiore, and Giorgio Scita. "Pathways linking endocytosis and actin cytoskeleton in mammalian cells". In: *Experimental Cell Research* 271.1 (2001), pp. 45–56. ISSN: 00144827. DOI: 10.1006/excr.2001.5369.

[139] Yohalie Kalukula et al. "Mechanics and functional consequences of nuclear deformations". In: *Nature Reviews Molecular Cell Biology* 23.9 (2022), pp. 583–602. ISSN: 1471-0072. DOI: 10.1038/s41580-022-00480-z. URL: https://www.nature.com/articles/s41580-022-00480-z.

[140] Sirio Dupont and Sara A. Wickström. "Mechanical regulation of chromatin and transcription". In: *Nature Reviews Genetics* 23.10 (2022), pp. 624–643. ISSN: 14710064. DOI: 10.1038/s41576-022-00493-6.

[141] Melissa Crisp et al. "Coupling of the nucleus and cytoplasm: Role of the LINC complex". In: *Journal of Cell Biology* 172.1 (2006), pp. 41–53. ISSN: 1540-8140. DOI: 10.1083/jcb.200509124. URL: https://rupress.org/jcb/article/172/1/41/52138/Coupling-of-the-nucleus-and-cytoplasm-Role-of-the.

[142] Kyle J. Roux et al. "Nesprin 4 is an outer nuclear membrane protein that can induce kinesin-mediated cell polarization". In: *Proceedings of the National Academy of Sciences* 106.7 (2009), pp. 2194–2199. ISSN: 0027-8424. DOI: 10.1073/pnas.0808602106. URL: http://www.pnas.org/cgi/doi/10.1073/

pnas.0808602106http://www.ncbi.nlm.nih.gov/pubmed/19164528http://www.pubmedcentral.nih.gov/articlerender.fcgi?artid=PMC2650131.

[143] Kevin Wilhelmsen et al. "Nesprin-3, a novel outer nuclear membrane protein, associates with the cytoskeletal linker protein plectin". In: *Journal of Cell Biology* 171.5 (2005), pp. 799–810. ISSN: 1540-8140. DOI: 10.1083/jcb.200506083. URL: http://www.jcb.org/cgi/https://rupress.org/jcb/article/171/5/799/52045/Nesprin3-a-novel-outer-nuclear-membrane-protein.

[144] Andrew D. Stephens. "Chromatin rigidity provides mechanical and genome protection". In: *Mutation Research - Fundamental and Molecular Mechanisms of Mutagenesis* 821.January (2020), p. 111712. ISSN: 18792871. DOI: 10.1016/j.mrfmmm.2020.111712. URL: https://doi.org/10.1016/j.mrfmmm.2020.111712.

[145] A. K. Balaji et al. "Nuclear envelope, chromatin organizers, histones, and DNA: The many achilles heels exploited across cancers". In: *Frontiers in Cell and Developmental Biology* 10.December (2022), pp. 1–21. ISSN: 2296634X. DOI: 10.3389/fcell.2022.1068347.

[146] Coral Y. Zhou et al. "Mechanisms of ATP-Dependent Chromatin Remodeling Motors". In: *Annual Review of Biophysics* 45 (2016), pp. 153–181. ISSN: 19361238. DOI: 10.1146/annurev-biophys-051013-022819.

[147] Karl A. Haushalter and James T. Kadonaga. "Chromatin assembly by DNA-translocating motors". In: *Nature Reviews Molecular Cell Biology* 4.8 (2003), pp. 613–620. ISSN: 14710072. DOI: 10.1038/nrm1177.

[148] Katarzyna Pogoda et al. "Unique Role of Vimentin Networks in Compression Stiffening of Cells and Protection of Nuclei from Compressive Stress". In: *Nano Letters* 22.12 (2022), pp. 4725–4732. ISSN: 15306992. DOI: 10.1021/acs.nanolett.2c00736.

[149] Michael C. Keeling et al. "Actomyosin and vimentin cytoskeletal networks regulate nuclear shape, mechanics and chromatin organization". In: *Scientific Reports* 7.1 (2017), pp. 1–14. ISSN: 20452322. DOI: 10.1038/s41598-017-05467-x.

[150] Jeong Ki Kim et al. “Nuclear lamin A/C harnesses the perinuclear apical actin cables to protect nuclear morphology”. In: *Nature Communications* 8.1 (2017), pp. 1–13. ISSN: 20411723. DOI: 10.1038/s41467-017-02217-5. URL: http://dx.doi.org/10.1038/s41467-017-02217-5.

[151] Kuang Liu et al. “Dynamic Nuclear Structure Emerges from Chromatin Cross-Links and Motors”. In: *Physical Review Letters* 126.15 (2021), p. 158101. ISSN: 0031-9007. DOI: 10.1103/PhysRevLett.126.158101. arXiv: 2008.07417. URL: https://doi.org/10.1103/PhysRevLett.126.158101https://link.aps.org/doi/10.1103/PhysRevLett.126.158101.

[152] Andrew D. Stephens et al. “Chromatin and lamin a determine two different mechanical response regimes of the cell nucleus”. In: *Molecular Biology of the Cell* 28.14 (2017), pp. 1984–1996. ISSN: 19394586. DOI: 10.1091/mbc.E16-09-0653.

[153] K. Tanuj Sapra et al. “Nonlinear mechanics of lamin filaments and the meshwork topology build an emergent nuclear lamina”. In: *Nature Communications* 11.1 (2020), pp. 1–14. ISSN: 20411723. DOI: 10.1038/s41467-020-20049-8. URL: http://dx.doi.org/10.1038/s41467-020-20049-8.

[154] Nathan Gamarra and Geeta J. Narlikar. “Collaboration through chromatin: motors of transcription and chromatin structure”. In: *Journal of Molecular Biology* 433.14 (2021). ISSN: 10898638. DOI: 10.1016/j.jmb.2021.166876.

[155] Coral Y. Zhou et al. “Mechanisms of ATP-Dependent Chromatin Remodeling Motors”. In: *Annual Review of Biophysics* 45 (2016), pp. 153–181. ISSN: 19361238. DOI: 10.1146/annurev-biophys-051013-022819.

[156] Haitham A. Shaban, Roman Barth, and Kerstin Bystricky. “Formation of correlated chromatin domains at nanoscale dynamic resolution during transcription”. In: *Nucleic Acids Research* 46.13 (2018), e77. ISSN: 13624962. DOI: 10.1093/nar/gky269.

[157] Gaurav Bajpai et al. “Mesoscale phase separation of chromatin in the nucleus”. In: *eLife* 10 (2021), pp. 1–26. ISSN: 2050084X. DOI: 10.7554/eLife.63976.

[158] Achal Mahajan et al. “Euchromatin Activity Enhances Segregation and Compaction of Heterochromatin in the Cell Nucleus”. In: *Physical Review X* 12.4 (2022), p. 41033. ISSN: 21603308. DOI: 10.1103/PhysRevX.12.041033. URL: https://doi.org/10.1103/PhysRevX.12.041033.

[159] Nicholas S. Wren et al. “Modeling nuclear blebs in a nucleoskeleton of independent filament networks”. In: *Cellular and Molecular Bioengineering* 5.1 (2012), pp. 73–81. ISSN: 18655025. DOI: 10.1007/s12195-011-0196-5.

[160] Noa Lamm et al. “Nuclear F-actin counteracts nuclear deformation and promotes fork repair during replication stress”. In: *Nature Cell Biology* 22.12 (2020), pp. 1460–1470. ISSN: 14764679. DOI: 10.1038/s41556-020-00605-6. URL: http://dx.doi.org/10.1038/s41556-020-00605-6.

[161] Jennifer Zagelbaum et al. “Multiscale reorganization of the genome following DNA damage facilitates chromosome translocations via nuclear actin polymerization”. In: *Nature Structural and Molecular Biology* 30.1 (2023), pp. 99–106. ISSN: 15459985. DOI: 10.1038/s41594-022-00893-6.

[162] Haruka Oda et al. “Actin filaments accumulated in the nucleus remain in the vicinity of condensing chromosomes in the zebrafish early embryo”. In: *Biology Open* 12.5 (2023). DOI: 10.1242/bio.059783.

[163] Cécile Leduc and Sandrine Etienne-Manneville. “Intermediate filaments in cell migration and invasion: the unusual suspects”. In: *Current Opinion in Cell Biology* 32 (2015), pp. 102–112. ISSN: 09550674. DOI: 10.1016/j.ceb.2015.01.005. URL: https://linkinghub.elsevier.com/retrieve/pii/S0955067415000071.

[164] Frida Danielsson et al. “Vimentin Diversity in Health and Disease”. In: *Cells* 7.10 (2018), p. 147. ISSN: 2073-4409. DOI: 10.3390/cells7100147. URL: http://www.mdpi.com/2073-4409/7/10/147.

[165] Milos Pekny and E. Birgitte Lane. “Intermediate filaments and stress”. In: *Experimental Cell Research* 313.10 (2007), pp. 2244–2254. ISSN: 00144827. DOI:

10.1016/j.yexcr.2007.04.023. URL: https://linkinghub.elsevier.com/retrieve/pii/S0014482707001681.

[166] Melissa G. Mendez, Shin-Ichiro Kojima, and Robert D. Goldman. "Vimentin induces changes in cell shape, motility, and adhesion during the epithelial to mesenchymal transition". In: *The FASEB Journal* 24.6 (2010), pp. 1838–1851. ISSN: 0892-6638. DOI: 10.1096/fj.09-151639. URL: https://onlinelibrary.wiley.com/doi/abs/10.1096/fj.09-151639.

[167] B. Eckes et al. "Impaired wound healing in embryonic and adult mice lacking vimentin." In: *Journal of cell science* 113 (Pt 1.13 (2000), pp. 2455–62. ISSN: 0021-9533. DOI: https://doi.org/10.1242/jcs.113.13.2455. URL: http://www.ncbi.nlm.nih.gov/pubmed/10852824.

[168] Micah R. Rogel et al. "Vimentin is sufficient and required for wound repair and remodeling in alveolar epithelial cells". In: *The FASEB Journal* 25.11 (2011), pp. 3873–3883. ISSN: 0892-6638. DOI: 10.1096/fj.10-170795. URL: https://onlinelibrary.wiley.com/doi/abs/10.1096/fj.10-170795.

[169] Martha E. Kidd, Dale K. Shumaker, and Karen M. Ridge. "The Role of Vimentin Intermediate Filaments in the Progression of Lung Cancer". In: *American Journal of Respiratory Cell and Molecular Biology* 50.1 (2013), p. 130827094923003. ISSN: 1044-1549. DOI: 10.1165/rcmb.2013-0314TR. URL: http://www.atsjournals.org/doi/abs/10.1165/rcmb.2013-0314TR.

[170] Arun Satelli and Shulin Li. "Vimentin in cancer and its potential as a molecular target for cancer therapy". In: *Cellular and Molecular Life Sciences* 68.18 (2011), pp. 3033–3046. ISSN: 1420-682X. DOI: 10.1007/s00018-011-0735-1. URL: http://link.springer.com/10.1007/s00018-011-0735-1.

[171] P. Friedl and E.-B. Brocker. "The biology of cell locomotion within three-dimensional extracellular matrix". In: *Cellular and Molecular Life Sciences (CMLS)* 57.1 (2000), pp. 41–64. ISSN: 1420-682X. DOI: 10.1007/s000180050498. URL: http://link.

springer.com/10.1007/s000180050498http://www.ncbi.nlm.nih.gov/pubmed/10949580.

[172] Ryan J. Petrie and Kenneth M. Yamada. "At the leading edge of three-dimensional cell migration". In: *Journal of Cell Science* 125.24 (2012), pp. 5917–5926. ISSN: 0021-9533. DOI: 10.1242/jcs.093732. URL: http://jcs.biologists.org/cgi/doi/10.1242/jcs.093732.

[173] Eric M. Balzer et al. "Physical confinement alters tumor cell adhesion and migration phenotypes". In: *FASEB Journal* 26.10 (2012), pp. 4045–4056. ISSN: 15306860. DOI: 10.1096/fj.12-211441.

[174] Andrew D. Doyle et al. "One-dimensional topography underlies three-dimensional fibrillar cell migration". In: *Journal of Cell Biology* 184.4 (2009), pp. 481–490. ISSN: 1540-8140. DOI: 10.1083/jcb.200810041. URL: https://rupress.org/jcb/article/184/4/481/35229/Onedimensional-topography-underlies.

[175] Peter Friedl, Katarina Wolf, and Jan Lammerding. "Nuclear mechanics during cell migration". In: *Current Opinion in Cell Biology* 23.1 (2011), pp. 55–64. ISSN: 09550674. DOI: 10.1016/j.ceb.2010.10.015. URL: https://linkinghub.elsevier.com/retrieve/pii/S0955067410001869.

[176] Anne Reversat et al. "Cellular locomotion using environmental topography". In: *Nature* 582.7813 (2020), pp. 582–585. ISSN: 0028-0836. DOI: 10.1038/s41586-020-2283-z. URL: https://doi.org/10.1038/s41586-020-2283-zhttp://www.nature.com/articles/s41586-020-2283-z.

[177] M. Le Berre et al. "Geometric Friction Directs Cell Migration". In: *Physical Review Letters* 111.19 (2013), p. 198101. ISSN: 0031-9007. DOI: 10.1103/PhysRevLett.111.198101. URL: https://link.aps.org/doi/10.1103/PhysRevLett.111.198101.

[178] R. J. Hawkins et al. "Pushing off the Walls: A Mechanism of Cell Motility in Confinement". In: *Physical Review Letters* 102.5 (2009), p. 058103. ISSN: 0031-9007. DOI: 10.1103/PhysRevLett.102.058103. URL: https://link.aps.org/doi/10.1103/PhysRevLett.102.058103.

[179] Gaudenz Danuser, Jun Allard, and Alex Mogilner. "Mathematical Modeling of Eukaryotic Cell Migration: Insights Beyond Experiments". In: *Annual Review of Cell and Developmental Biology* 29.1 (2013), pp. 501–528. ISSN: 1081-0706. DOI: 10.1146/annurev-cellbio-101512-122308. URL: http://www.annualreviews.org/doi/10.1146/annurev-cellbio-101512-122308.

[180] Jian Zhang and Yu-li Wang. "Centrosome defines the rear of cells during mesenchymal migration". In: *Molecular Biology of the Cell* 28.23 (2017). Ed. by Manuel Théry, pp. 3240–3251. ISSN: 1059-1524. DOI: 10.1091/mbc.e17-06-0366. URL: https://www.molbiolcell.org/doi/10.1091/mbc.e17-06-0366.

[181] Nancy Costigliola et al. "Vimentin fibers orient traction stress". In: *Proceedings of the National Academy of Sciences* 114.20 (2017), pp. 5195–5200. ISSN: 0027-8424. DOI: 10.1073/pnas.1614610114. URL: http://www.pnas.org/lookup/doi/10.1073/pnas.1614610114.

[182] Rachel A. Battaglia et al. "Vimentin on the move: new developments in cell migration". In: *F1000Research* 7.0 (2018), p. 1796. ISSN: 2046-1402. DOI: 10.12688/f1000research.15967.1. URL: https://f1000research.com/articles/7-1796/v1.

[183] Emma J. van Bodegraven and Sandrine Etienne-Manneville. "Intermediate filaments against actomyosin: the david and goliath of cell migration". In: *Current Opinion in Cell Biology* 66 (2020), pp. 79–88. ISSN: 09550674. DOI: 10.1016/j.ceb.2020.05.006. URL: https://doi.org/10.1016/j.ceb.2020.05.006https://linkinghub.elsevier.com/retrieve/pii/S0955067420300697.

[184] Alison E. Patteson et al. "The vimentin cytoskeleton: when polymer physics meets cell biology". In: *Physical Biology* 18.1 (2020), p. 011001. ISSN: 1478-3975. DOI: 10.1088/1478-3975/abbcc2. URL: https://iopscience.iop.org/article/10.1088/1478-3975/abbcc2.

[185] P. A. Janmey et al. "Viscoelastic properties of vimentin compared with other filamentous biopolymer networks." In: *Journal of Cell Biology* 113.1 (1991), pp. 155–

160. ISSN: 0021-9525. DOI: 10.1083/jcb.113.1.155. URL: https://rupress.org/jcb/article/113/1/155/55931/Viscoelastic-properties-of-vimentin-compared-with.

[186] Benjamin P. Bouchet and Anna Akhmanova. "Microtubules in 3D cell motility". In: *Journal of Cell Science* 130.1 (2017), pp. 39–50. ISSN: 0021-9533. DOI: 10.1242/jcs.189431. URL: http://jcs.biologists.org/lookup/doi/10.1242/jcs.189431.

[187] Alison E. Patteson et al. "Vimentin protects cells against nuclear rupture and DNA damage during migration". In: *Journal of Cell Biology* 218.12 (2019), pp. 4079–4092. ISSN: 0021-9525. DOI: 10.1083/jcb.201902046. URL: https://rupress.org/jcb/article/218/12/4079/132537/Vimentin-protects-cells-against-nuclear-rupture.

[188] Ming Guo et al. "The Role of Vimentin Intermediate Filaments in Cortical and Cytoplasmic Mechanics". In: *Biophysical Journal* 105.7 (2013), pp. 1562–1568. ISSN: 00063495. DOI: 10.1016/j.bpj.2013.08.037. URL: https://linkinghub.elsevier.com/retrieve/pii/S0006349513009843.

[189] Shailaja Seetharaman and Sandrine Etienne-Manneville. "Cytoskeletal Crosstalk in Cell Migration". In: *Trends in Cell Biology* 30.9 (2020), pp. 720–735. ISSN: 09628924. DOI: 10.1016/j.tcb.2020.06.004. URL: https://doi.org/10.1016/j.tcb.2020.06.004https://linkinghub.elsevier.com/retrieve/pii/S0962892420301227.

[190] Osigwe Esue et al. "A Direct Interaction between Actin and Vimentin Filaments Mediated by the Tail Domain of Vimentin*". In: *Journal of Biological Chemistry* 281.41 (2006), pp. 30393–30399. ISSN: 00219258. DOI: 10.1074/jbc.M605452200. URL: https://linkinghub.elsevier.com/retrieve/pii/S0021925819892517.

[191] Tatyana M. Svitkina, Alexander B. Verkhovsky, and Gary B. Borisy. "Plectin Sidearms Mediate Interactions of Intermediate Filaments With Microtubules and Other Components of the Cytoskeleton". In: *The Biological Bulletin* 194.3 (1998),

pp. 409–410. ISSN: 0006-3185. DOI: 10.2307/1543127. URL: https://www.journals.uchicago.edu/doi/10.2307/1543127.

[192] Shyam B. Khatau et al. "The distinct roles of the nucleus and nucleus-cytoskeleton connections in three-dimensional cell migration". In: *Scientific Reports* 2.1 (2012), p. 488. ISSN: 2045-2322. DOI: 10.1038/srep00488. URL: http://www.nature.com/articles/srep00488.

[193] Takamasa Harada et al. "Nuclear lamin stiffness is a barrier to 3D migration, but softness can limit survival". In: *Journal of Cell Biology* 204.5 (2014), pp. 669–682. ISSN: 15408140. DOI: 10.1083/jcb.201308029.

[194] Benjamin L. Bangasser, Steven S. Rosenfeld, and David J. Odde. "Determinants of Maximal Force Transmission in a Motor-Clutch Model of Cell Traction in a Compliant Microenvironment". In: *Biophysical Journal* 105.3 (2013), pp. 581–592. ISSN: 00063495. DOI: 10.1016/j.bpj.2013.06.027. URL: https://linkinghub.elsevier.com/retrieve/pii/S0006349513007066.

[195] J. H. Lopez, Moumita Das, and J. M. Schwarz. "Active elastic dimers: Cells moving on rigid tracks". In: *Physical Review E* 90.3 (2014), p. 032707. ISSN: 1539-3755. DOI: 10.1103/PhysRevE.90.032707. arXiv: 1406.4833. URL: https://link.aps.org/doi/10.1103/PhysRevE.90.032707.

[196] E. A. Evans and D. A. Calderwood. "Forces and Bond Dynamics in Cell Adhesion". In: *Science* 316.5828 (2007), pp. 1148–1153. ISSN: 0036-8075. DOI: 10.1126/science.1137592. URL: https://www.sciencemag.org/lookup/doi/10.1126/science.1137592.

[197] Joyce C.M. Meiring, Boris I. Shneyer, and Anna Akhmanova. "Generation and regulation of microtubule network asymmetry to drive cell polarity". In: *Current Opinion in Cell Biology* 62 (2020), pp. 86–95. ISSN: 09550674. DOI: 10.1016/j.ceb.2019.10.004. URL: https://doi.org/10.1016/j.ceb.2019.10.004https://linkinghub.elsevier.com/retrieve/pii/S0955067419300912.

[198] Colin D. Paul et al. "Engineered Models of Confined Cell Migration". In: *Annual Review of Biomedical Engineering* 18.1 (2016), pp. 159–180. ISSN: 1523-9829. DOI: 10.1146/annurev-bioeng-071114-040654. URL: http://www.annualreviews.org/doi/10.1146/annurev-bioeng-071114-040654.

[199] Nathalie Caille et al. "Contribution of the nucleus to the mechanical properties of endothelial cells". In: *Journal of Biomechanics* 35.2 (2002), pp. 177–187. ISSN: 00219290. DOI: 10.1016/S0021-9290(01)00201-9.

[200] Amir Vahabikashi et al. "Probe Sensitivity to Cortical versus Intracellular Cytoskeletal Network Stiffness". In: *Biophysical Journal* 116.3 (2019), pp. 518–529. ISSN: 00063495. DOI: 10.1016/j.bpj.2018.12.021. URL: https://pubs.acs.org/doi/10.1021/acs.analchem.8b05923https://linkinghub.elsevier.com/retrieve/pii/S0006349519300189.

[201] Harrison V. Prentice-Mott et al. "Biased migration of confined neutrophil-like cells in asymmetric hydraulic environments". In: *Proceedings of the National Academy of Sciences* 110.52 (2013), pp. 21006–21011. ISSN: 0027-8424. DOI: 10.1073/pnas.1317441110. URL: http://www.pnas.org/cgi/doi/10.1073/pnas.1317441110.

[202] Nicole M. Wakida et al. "An Intact Centrosome Is Required for the Maintenance of Polarization during Directional Cell Migration". In: *PLoS ONE* 5.12 (2010). Ed. by Maria G. Castro, e15462. ISSN: 1932-6203. DOI: 10.1371/journal.pone.0015462. URL: https://dx.plos.org/10.1371/journal.pone.0015462.

[203] Masahiro Ueda et al. "Centrosome positioning and directionality of cell movements". In: *Proceedings of the National Academy of Sciences* 94.18 (1997), pp. 9674–9678. ISSN: 0027-8424. DOI: 10.1073/pnas.94.18.9674. URL: http://www.pnas.org/cgi/doi/10.1073/pnas.94.18.9674.

[204] Georgia Salpingidou et al. "A novel role for the nuclear membrane protein emerin in association of the centrosome to the outer nuclear membrane". In: *Journal of Cell Biology* 178.6 (2007), pp. 897–904. ISSN: 1540-8140. DOI: 10.1083/jcb.200702026.

URL: https://rupress.org/jcb/article/178/6/897/44839/A-novel-role-for-the-nuclear-membrane-protein.

[205] Zhuo Gan et al. "Vimentin Intermediate Filaments Template Microtubule Networks to Enhance Persistence in Cell Polarity and Directed Migration". In: *Cell Systems* 3.5 (2016), pp. 500–501. ISSN: 24054712. DOI: 10.1016/j.cels.2016.11.011. URL: https://linkinghub.elsevier.com/retrieve/pii/S2405471216303763.

[206] William Humphrey, Andrew Dalke, and Klaus Schulten. "VMD: Visual molecular dynamics". In: *Journal of Molecular Graphics* 14.1 (1996), pp. 33–38. ISSN: 02637855. DOI: 10.1016/0263-7855(96)00018-5. URL: https://linkinghub.elsevier.com/retrieve/pii/0263785596000185.

[207] Guillaume Charras and Erik Sahai. "Physical influences of the extracellular environment on cell migration". In: *Nature Reviews Molecular Cell Biology* 15.12 (2014), pp. 813–824. ISSN: 1471-0072. DOI: 10.1038/nrm3897. URL: http://www.nature.com/articles/nrm3897.

[208] Beate Eckes et al. "Impaired mechanical stability, migration and contractile capacity in vimentin-deficient fibroblasts." In: *Journal of cell science* 111 (Pt 1.13 (1998), pp. 1897–907. ISSN: 0021-9533. URL: https://jcs.biologists.org/content/111/13/1897http://www.ncbi.nlm.nih.gov/pubmed/9625752.

[209] Ning Wang and Dimitrijie Stamenovic. "Mechanics of vimentin intermediate filaments." In: *Journal of muscle research and cell motility* 23.5-6 (2002), pp. 535–40. ISSN: 0142-4319. DOI: 10.1023/a:1023470709071. URL: http://www.ncbi.nlm.nih.gov/pubmed/12785103.

[210] Jason Lowery et al. "Intermediate Filaments Play a Pivotal Role in Regulating Cell Architecture and Function". In: *Journal of Biological Chemistry* 290.28 (2015), pp. 17145–17153. ISSN: 00219258. DOI: 10.1074/jbc.R115.640359. URL: https://linkinghub.elsevier.com/retrieve/pii/S0021925820353217.

[211] Tanmay P. Lele, Richard B. Dickinson, and Gregg G. Gundersen. "Mechanical principles of nuclear shaping and positioning". In: *Journal of Cell Biology* 217.10

(2018), pp. 3330–3342. ISSN: 0021-9525. DOI: 10.1083/jcb.201804052. URL: https://rupress.org/jcb/article/217/10/3330/120218/Mechanical-principles-of-nuclear-shaping-and.

[212] Alexandra Lynn McGregor, Chieh-Ren Hsia, and Jan Lammerding. "Squish and squeeze — the nucleus as a physical barrier during migration in confined environments". In: *Current Opinion in Cell Biology* 40 (2016), pp. 32–40. ISSN: 09550674. DOI: 10.1016/j.ceb.2016.01.011. URL: https://linkinghub.elsevier.com/retrieve/pii/S0955067416300035.

[213] Andrew J. Maniotis, Christopher S. Chen, and Donald E. Ingber. "Demonstration of mechanical connections between integrins, cytoskeletal filaments, and nucleoplasm that stabilize nuclear structure". In: *Proceedings of the National Academy of Sciences* 94.3 (1997), pp. 849–854. ISSN: 0027-8424. DOI: 10.1073/pnas.94.3.849. URL: http://www.pnas.org/cgi/doi/10.1073/pnas.94.3.849.

[214] Srujana Neelam et al. "Direct force probe reveals the mechanics of nuclear homeostasis in the mammalian cell". In: *Proceedings of the National Academy of Sciences* 112.18 (2015), pp. 5720–5725. ISSN: 0027-8424. DOI: 10.1073/pnas.1502111112. URL: http://www.pnas.org/lookup/doi/10.1073/pnas.1502111112.

[215] GW Gant Luxton and Gregg G. Gundersen. "Orientation and function of the nuclear–centrosomal axis during cell migration". In: *Current Opinion in Cell Biology* 23.5 (2011), pp. 579–588. ISSN: 09550674. DOI: 10.1016/j.ceb.2011.08.001. URL: https://linkinghub.elsevier.com/retrieve/pii/S0955067411001037.

[216] Marco Cosentino Lagomarsino et al. "Microtubule Organization in Three-Dimensional Confined Geometries: Evaluating the Role of Elasticity Through a Combined In Vitro and Modeling Approach". In: *Biophysical Journal* 92.3 (2007), pp. 1046–1057. ISSN: 00063495. DOI: 10.1529/biophysj.105.076893. URL: https://linkinghub.elsevier.com/retrieve/pii/S0006349507709128.

[217] M. Pinot et al. "Effects of Confinement on the Self-Organization of Microtubules and Motors". In: *Current Biology* 19.11 (2009), pp. 954–960. ISSN: 09609822. DOI:

10.1016/j.cub.2009.04.027. URL: https://linkinghub.elsevier.com/retrieve/pii/S0960982209010252.

[218] Matthew R. Zanotelli et al. "Energetic costs regulated by cell mechanics and confinement are predictive of migration path during decision-making". In: *Nature Communications* 10.1 (2019), p. 4185. ISSN: 2041-1723. DOI: 10.1038/s41467-019-12155-z. URL: http://dx.doi.org/10.1038/s41467-019-12155-zhttp://www.nature.com/articles/s41467-019-12155-z.

[219] Hawa-Racine Thiam et al. "Perinuclear Arp2/3-driven actin polymerization enables nuclear deformation to facilitate cell migration through complex environments." In: *Nature communications* 7.1 (2016), p. 10997. ISSN: 2041-1723. DOI: 10.1038/ncomms10997. URL: http://www.nature.com/articles/ncomms10997.

[220] A. J. Lomakin et al. "The nucleus acts as a ruler tailoring cell responses to spatial constraints". In: *Science* 370.6514 (2020), eaba2894. ISSN: 0036-8075. DOI: 10.1126/science.aba2894. URL: https://www.sciencemag.org/lookup/doi/10.1126/science.aba2894.

[221] Louis S. Prahl et al. "Predicting Confined 1D Cell Migration from Parameters Calibrated to a 2D Motor-Clutch Model". In: *Biophysical Journal* 118.7 (2020), pp. 1709–1720. ISSN: 00063495. DOI: 10.1016/j.bpj.2020.01.048. URL: http://www.ncbi.nlm.nih.gov/p.

[222] Amit Pathak. "Modeling and predictions of biphasic mechanosensitive cell migration altered by cell-intrinsic properties and matrix confinement". In: *Physical Biology* 15.6 (2018), p. 065001. ISSN: 1478-3975. DOI: 10.1088/1478-3975/aabdcc. URL: https://iopscience.iop.org/article/10.1088/1478-3975/aabdcc.

[223] David B. Brückner et al. "Disentangling the behavioural variability of confined cell migration". In: *Journal of The Royal Society Interface* 17.163 (2020), p. 20190689. ISSN: 1742-5689. DOI: 10.1098/rsif.2019.0689. URL: https://royalsocietypublishing.org/doi/10.1098/rsif.2019.0689.

[224] Brian A. Camley and Wouter-Jan Rappel. "Velocity alignment leads to high persistence in confined cells". In: *Physical Review E* 89.6 (2014), p. 062705. ISSN: 1539-3755. DOI: 10.1103/PhysRevE.89.062705. URL: https://link.aps.org/doi/10.1103/PhysRevE.89.062705.

[225] Ryan J Petrie and Kenneth M Yamada. "Fibroblasts Lead the Way: A Unified View of 3D Cell Motility". In: *Trends in Cell Biology* 25.11 (2015), pp. 666–674. ISSN: 09628924. DOI: 10.1016/j.tcb.2015.07.013. URL: http://dx.doi.org/10.1016/j.tcb.2015.07.013https://linkinghub.elsevier.com/retrieve/pii/S0962892415001464.

[226] Thomas R. Geiger and Daniel S. Peeper. "Metastasis mechanisms". In: *Biochimica et Biophysica Acta - Reviews on Cancer* 1796.2 (2009), pp. 293–308. ISSN: 0304419X. DOI: 10.1016/j.bbcan.2009.07.006. URL: http://dx.doi.org/10.1016/j.bbcan.2009.07.006.

[227] Mrinal Pandey et al. "Mechanical compression regulates tumor spheroid invasion into a 3D collagen matrix ." In: ().

[228] Maryna Perepelyuk et al. "Normal and fibrotic rat livers demonstrate shear strain softening and compression stiffening: A model for soft tissue mechanics". In: *PLoS ONE* 11.1 (2016), pp. 1–18. ISSN: 19326203. DOI: 10.1371/journal.pone.0146588.

[229] Katarzyna Pogoda et al. "Compression stiffening of brain and its effect on mechanosensing by glioma cells". In: *New Journal of Physics* 16 (2014). ISSN: 13672630. DOI: 10.1088/1367-2630/16/7/075002.

[230] Chris H. Rycroft. "VORO++: A three-dimensional Voronoi cell library in C++". In: *Chaos* 19.4 (2009). ISSN: 10541500. DOI: 10.1063/1.3215722.

Sarthak Gupta

(+1) 315-515-7370 • sgupta14@syr.edu

Education

Ph.D. in Physics **Aug 2017 - Aug 2023**
Syracuse University, Syracuse, NY, USA
Thesis Advisors: Prof. Jennifer Schwarz & Prof. Alison Patteson
Thesis Title: Physical Insights into Biological Processes: From Viral Uptake to Chromatin Organization to Cell Motility to Tissue Rigidity

M.S. in Physics **Aug 2014 - Jun 2017**
Indian Institute of Science Education and Research, Bhopal, MP, India
Thesis Advisor: Prof. Snigdha Thakur
Thesis Title: Probing the Dynamics of Passive Polymers in an Active Bath

B.Sc. in Physical Science **Aug 2010 - Jun 2013**
University of Delhi, Delhi, India
First in a class of 200 students

Publications and Preprints

7. T. Zhang, **S. Gupta**, M.A. Lancaster, J.M. Schwarz "How human-derived brain organoids are built differently from brain organoids derived of genetically-close relatives: A multi-scale hypothesis"arXiv:2304.08622 (2023)
6. **S. Gupta**, C.D. Santangelo, A.E. Patteson, J.M. Schwarz "How cells wrap around virus-like particles using extracellular filamentous protein structures" arXiv:2301.08776 (2023)
5. I.K. Berg*, M.L. Currey*, **S. Gupta**, Y. Berrada, B.N. Viet, M. Pho, A.E. Patteson, J.M. Schwarz, E.J. Banigan, A.D. Stephens "Transcription regulates bleb formation and stability independent of nuclear rigidity" bioRxiv, 2022.11. 14.516344 (2022)
4. M. Asp, E. Jutzeler, J. Kochanowski, K. Kerr, D. Song, **S. Gupta**, B. Carroll, A.E. Patteson "A Torsion-Based Rheometer for Measuring Viscoelastic Material Properties" The Biophysicist 3 (2), 94-105 (2022)
3. M. Swoger, **S. Gupta**, E.E. Charrier, M. Bates, H. Hehnly, and A.E. Patteson "Vimentin Intermediate Filaments Mediate Cell Morphology on Viscoelastic Substrates" ACS Applied Bio Materials 5, 2, 552-561 (2022)
2. Ł. Suprewicz*, M. Swoger*, **S. Gupta**, E. Piktel, F.J. Byfield, D.V. Iwamoto, D. Germann, J. Reszeć, N. Marcińczyk, R.J. Carroll, P.A. Janmey, J.M. Schwarz, R. Bucki, A.E. Patteson "Extracellular Vimentin as a Target Against SARS-CoV-2 Host Cell Invasion" Small 18, 2105640 (2021)
1. **S. Gupta**, A.E. Patteson, J.M. Schwarz, "Vimentin Mediates Nuclear Shape and Position to Affect Cell Speed and Polarity in Confinement" New Journal of Physics 23, 093042 (2021)

* Co-first Authors

In Preparation

2. **S. Gupta**, A.D. Stephens, A.E. Patteson, J.M. Schwarz, E.J. Banigan "Active chromatin drives cell nuclear bulge formation"
1. **S. Gupta**, T. Zhang, A.E. Patteson, J.M. Schwarz "Investigation of Tissue Mechanics Under Compression with Three-Dimensional Vertex Model"

Research Experience

Research Assistant, Department of Physics **May 2019 - Present**
Syracuse University

Role of Cytoskeleton in Confined Cell Motility and Polarity

- Developed a simulation model of a cell in confinement and reproduced the experimental results investigating the role of vimentin intermediate filament in cell motility.
- Proposed a new confined cell polarity mechanism based on the nucleus-vimentin interactions with centrosome positioning for vimentin-null and wild-type cells.

Cell Surface Components aids in Viral Uptake via Endocytosis

- Developed a simulation model of coronavirus with spikes, a cell membrane (with bending rigidity), and cell surface components to understand the role of coreceptors' mechanical properties in endocytosis.

Investigation of Bulge Formations in Cell Nuclear Lamina due to Chromatin Activity

- Developed a simulation model of chromatin, and nuclear lamina with crosslinkers, linkages, and extensile and contractile motors acting on chromatin.
- Designed a new algorithm to generate a shell made up of a random network of particles with non-neighboring repulsion.

Research Assistant, Department of Physics **May 2015 - July 2017**
Indian Institute of Science Education and Research

Computational study of a passive polymer in an active bath

- Investigated the role of polymer's semi-flexibility and bath activity in achieving various polymer configurations using Langevin dynamics.
- Implemented multi-particle collision dynamics to understand the effects of hydrodynamics on polymer configurations in an active bath.

Computational Skills

Programming: FORTRAN 90 (Proficient), C++ (Basic), Python (Basic), Shell Script

Simulation Techniques: Molecular Dynamics, Monte Carlo, Langevin Dynamics, Multi-Particle Collison Dynamics

Software Proficiency: Visual Molecular Dynamics (VMD), InkScape, LaTeX, Gnuplot, ImageJ

Grant

Principal Investigator at American Physical Society's [Link] **Apr 2021**
New York State Section Outreach Grant (Value of $2060)

Awards, Honors, and Fellowships

Dissertation Awards

Graduate Dean's Award for Excellence in Research and Creative Work **March 2023**
Syracuse University, NY, USA (Value of $500)

Fellowships

Syracuse University Dissertation Fellowship **July 2022**
Syracuse University, NY, USA (Value of $25,290/ One year stipend)

Summer Dissertation Fellowship **May 2022**
Syracuse University, NY, USA (Value of $4,000)

Research Excellence Doctoral Funding (REDF) Graduate Fellowship **Aug 2020**
Syracuse University, NY, USA (Value of $26,010/ One year stipend)

College of Arts and Sciences Summer Fellowship **May 2018**
Syracuse University, NY, USA (Value of $750)

Institute Fellowship, Indian Institute of Science Education and Research **Aug 2014**
Bhopal, Madhya Pradesh, India (Three full year stipend)

Talk and Poster Awards

Emerging Soft Matter Excellence Award (ESME) **March 2023**
Divison of Soft Matter, APS March Meeting 2023, Las Vegas, USA

Poster Award in 122^{nd} Topical Symposium of the New York State Section **Nov 2020**
American Physical Society (APS) (Virtual) (Value of $200)

Travel Awards

American Physical Society's (APS) FIP Distinguished Student award **March 2023**
for presenting in APS March Meeting 2023 in Las Vegas, USA (Value of $300)

American Physical Society's (APS) DSOFT Future Investigator Travel **Jan 2023**
Award for presenting in Apsen Active Matter Conference Jan, 2023 in Colorado, USA (Value of $500)

SU Graduate Student Organization's Professional, Academic, and Creative **Dec 2022**
Work Grant for presenting in Apsen Active Matter Conference Jan, 2023 in Colorado, USA (Value of $500)

American Physical Society's (APS) DSOFT Travel Award **Feb 2022**
for presenting in APS March Meeting 2022 in Chicago, USA (Value of $500)

BioPhysical Society's (BPS) Travel Award for presenting in **Nov 2021**
66^{th} BPS Annual Meeting, Feb 2022 in San Franscico, USA (Value of $500)

SU Graduate Student Organization (GSO) Travel Award for presenting **Feb 2021**
in 65^{th} BPS Annual Meeting meeting, Feb 2021 (Virtual) (Value of $250)

American Physical Society (APS) DBIO Shirley Chan Student Travel Award **Dec 2020**
for presenting in APS March Meeting 2021 (Virtual) (Value of $100)

Equity Diversity and Inclusion (EID) Awards

Social Justice and Community Building Award **Apr 2022**
Department of Physics, Syracuse University, Syracuse, NY, USA

Press Coverages

T.V. Interview for Sars-CoV-2 work in PBS's WCNY [Link] **Dec 2021**
Cycle of Health's episode Fighting Future Pandemics

Confined cell motility work featured in College of Arts [Link] **Oct 2021**
and Sciences news, Syracuse University, Syracuse, NY, USA

Invited Talks

5. **S. Gupta**, A.E. Patteson, J.M. Schwarz **Sept 2022**
   From chromatin to covid: Interplay of mechanics and geometry in living materials
   Department of Physics, Rochester Institute of Technology

4. **S. Gupta**, A.E. Patteson, J.M. Schwarz **Aug 2022**
   From chromatin to covid: Interplay of mechanics and geometry in living materials
   Summer Seminar Series, Department of Biology, University of Rochester

3. **S. Gupta**, A.E. Patteson, J.M. Schwarz **Sept 2021**
   Modeling the effect of vimentin on confined cell motility
   Mechanics of Development and Disease Meet, BioInspired Institute, Syracuse University

2. **S. Gupta**, A.E. Patteson, J.M. Schwarz **Aug 2021**
   Role of vimentin in confined cell motility and SARS-CoV-2 uptake
   Summer Soft and Living Matter Seminar, Department of Physics, Syracuse University

1. **S. Gupta**, A.E. Patteson, J.M. Schwarz **Apr 2020**
   Modeling the effect of vimentin on confined cell motility
   Cytoskeleton in Tissue Morphogenesis Microsymposium, Syracuse University

Contributed Talks

4. **S. Gupta**, I.K. Oder, Y. Berrada, A. Stephens, A.E. Patteson, E.J. Banigan, J.M. Schwarz, Active Chromatin Dynamics Drives Nuclear Bulge Formation, **Mar 2023**
   American Physical Society March Meeting, Las Vegas, NV, USA

3. **S. Gupta**, E.D. Banigan, A.E. Patteson, J.M. Schwarz **Mar 2022**
Cell nuclei: From nonlinear mechanics to nontrivial shapes
American Physical Society March Meeting, Chicago, IL, USA

2. **S. Gupta**, A.E. Patteson, J.M. Schwarz **Mar 2021**
Vimentin mediates nuclear shape and position to affect cell speed and polarity in confinement, American Physical Society March Meeting (Virtual)

1. **S. Gupta**, A.E. Patteson, J.M. Schwarz **Mar 2020**
Modeling the effect of vimentin on confined cell motility
American Physical Society March Meeting (Virtual)

Poster Presentations

14. **S. Gupta** , I.K. Berg, M.L. Currey, M. Swoger, A. Stephens, **April 2023**
A.E. Patteson, J. M. Schwarz, E.J. Banigan, Active chromatin drives cell nuclear bulge formation, 5^{th} CEMB Annual Mechanobiology Symposium, UPenn, PA, USA

13. **S. Gupta** , I.K. Berg, M.L. Currey, M. Swoger, A. Stephens, **Jan 2023**
A.E. Patteson, J. M. Schwarz, E.J. Banigan, Active chromatin drives cell nuclear bulge formation, Active Matter in Complex Environments, Aspen, Colorado, USA

12. **S. Gupta**, E.D. Banigan, A.E. Patteson, J.M. Schwarz **Feb 2022**
Cell nuclei: From nonlinear mechanics to nontrivial shapes
66^{th} Biophysical Society Annual Meeting, San Francisco, CA, USA

11. **S. Gupta**, E.D. Banigan, A.E. Patteson, J.M. Schwarz **Sep 2021**
Compressing the cell nucleus: Nonlinear mechanics to nontrivial shapes
12^{th} Physics of Cancer Symposium, Leipzig, Germany (Virtual)

10. **S. Gupta**, A.E. Patteson, J.M. Schwarz **Jul 2021**
Vimentin-nuclear interplay in confined cell motility
Physics Meets Biology, Biological Physics Group, Institute Of Physics (Virtual)

9. **S. Gupta**, A.E. Patteson, J.M. Schwarz **Jun 2021**
Modeling the effect of vimentin on confined cell motility
Physics of Living Systems: From molecules to tissues, Austria (Virtual)

8. **S. Gupta**, A.E. Patteson, J.M. Schwarz **Jun 2021**
Role of vimentin in confined cell motility and SARS-CoV-2 uptake
School on Soft Solids and Complex Fluids, UMass Amherst, MA, USA (Virtual)

7. **S. Gupta**, M. Swoger, A.E. Patteson, J.M. Schwarz **Feb 2021**
Extracellular vimentin serves as co-receptor for SARS-CoV 2
65^{th} Biophysical Society Annual Meeting, USA (Virtual)

6. **S. Gupta**, A.E. Patteson, J.M. Schwarz **Jan 2021**
Vimentin mediates nuclear shape and position to affect cell speed and polarity in confinement, 3^{rd} CEMB Annual Mechanobiology Symposium, UPenn, PA, USA (Virtual)

5. **S. Gupta**, A.E. Patteson, J.M. Schwarz **Dec 2020**
   Effects of vimentin on confined cell motility
   4^{th} International Conference on Soft Materials, MNIT, RJ, India (Virtual)

4. **S. Gupta**, A.E. Patteson, J.M. Schwarz **Dec 2020**
   Effects of vimentin on confined cell motility
   Complex Fluids Symposium Conference, IIT Bombay, Mumbai, India (Virtual)

3. **S. Gupta**, M. Swogger, A.E. Patteson, J.M. Schwarz **Nov 2020**
   Extracellular vimentin serves as co-receptor for SARS-CoV 2
   122^{nd} Topical Symposium, New York State Section, APS (Virtual)

2. **S. Gupta**, A.E. Patteson, J.M. Schwarz **Jan 2020**
   Effects of vimentin on confined cell motility
   Physics of Collective Cell Migration, PCTS, Princeton University, NJ, USA

1. **S. Gupta**, A.E. Patteson, J.M. Schwarz **Dec 2019**
   Effects of vimentin on confined cell motility
   Complex Fluids Conference, IISER Bhopal, MP, India

School/ Workshop/ Conference/ Symposium Attended

6. Summer School on Soft Solids and Complex Fluids **Jun 2021**
   University of Massachusetts Amherst, MA, USA (Virtual)
5. Symposium - 11^{th} Annual Symposium Physics of Cancer **Sep 2020**
   Leipzig, Germany (Virtual)
4. Workshop - Fibrous Networks in Biology at LRSM **May 2019**
   University of Pennsylvania, PA, USA
3. Symposium - Central New York Cytoskeleton symposium **Apr 2019**
   BioTech Accelerator, Syracuse, NY, USA
2. Conference - American Physical Society March Meeting, Boston, MA USA **Mar 2019**
1. Winter School - Motile Active matter: Nanomachines, Microswimmers and Swarms Forschungszentrum Jülich, Germany **Feb 2019**

Mentoring and Outreach Experience

Mentoring Physics Department's Ph.D. student in developing simulation code base for liquid-liquid phase separation research. **Fall 2021-Present**

Wrote external grant, handled logistics, budget, and organized outreach visits.

- Organized and presented to 150 students in seven high school classes (Physics, Biology, Earth Sciences) outreach visits across three schools in Greater Syracuse City Area, NY **2021-2022**
- Organized and presented to 60 students in four middle school summer camps at Museum of Science and Technology (MOST) Syracuse, NY **Summer 2021**
- Designed two new Physics research outreach lessons with experimental demos, group activities, worksheets, and handouts **Summer 2021**

Teaching Experience

Teaching Assistant, Physics Department, Syracuse University **Aug 2017 - Apr 2019**
Designed rubrics, conducted labs & lessons, graded exams, essays, and presentations

- General Physics I Lab (Mechanics | Non-Major Sophomore) **Spring 2018, 2019**
- Our Corner in the Universe (Astronomy | Non-Major Freshman) **Fall 2018**
- General Physics II Lab (Electricity & Magnetism | Non-Major Sophomore) **Fall 2017**

Professional Development

Completed Syracuse University's Future Professoriate Program (FPP) **Apr 2022**

Bioinspired Institute Graduate and Postdoctoral Development Program, Syracuse University **Fall 2019- Present**

Professional Services

Proposed, selected and chaired for APS Invited Session MM23 "Brain Organoids: From morphogenesis to metamaterials" **Sep 2022**

Assisted in reviewing manuscript for Frontiers in Physics **May 2022**

Tabling for DSOFT and DBIO in APS March meeting **Mar 2022, 2023**

Organizer of Peer Writing Group **2021-2022**
Department of Physics, Syracuse University, Syracuse, NY, USA

Served in Physics Department Outreach Committee **2021-2022**
Syracuse University, Syracuse, NY, USA

Professional Societies

American Physical Society, Student Member **2019 - Present**

Biophysical Society, Student Member **2021 - Present**

References

Prof. Jennifer M. Schwarz
Professor, Department of Physics
Syracuse University, Syracuse
NY 13244, USA
Email: jmschw02@syr.edu

Prof. Christian D. Santangelo
Professor, Department of Physics
Syracuse University, Syracuse
NY 13244, USA
Email: cdsantan@syr.edu

Prof. Alison E. Patteson
Assistant Professor, Department of Physics
Syracuse University, Syracuse
NY 13244, USA
Email: aepattes@syr.edu

Prof. Moumita Das
Associate Professor, School of Physics and Astronomy
Rochester Institute of Technology, Rochester
NY 14623, USA
Email: modsps@rit.edu